Die approbierte Originalversion dieser Dissertation ist an der Hauptbibliothek der Technischen Universität Wien aufgestellt (http://www.ub.tuwien.ac.at).

The approved original version of this thesis is available at the main library of the Vienna University of Technology (http://www.ub.tuwien.ac.at/englweb/).

TECHNISCHE UNIVERSITÄT WIEN
Vienna University of Technology

DISSERTATION

Weakly Three-dimensional Transonic Laminar Flows in Slender Channels

ausgeführt zum Zwecke der Erlangung des akademischen Grade eines Doktors der technischen Wissenschaften unter der Leitung von

o.Univ.-Prof. Dipl.-Ing. Dr.techn. Alfred Kluwick
E322
Institut für Strömungsmechanik und Wärmeübertragung

eingereicht an der Technischen Universität Wien
Fakultät für Maschinenwesen und Betriebswissenschaften

von

Dipl.-Ing. Matthias Kornfeld
Matrikelnummer: 0325795
Parkstraße 4/21, A-2340 Mödling

Wien, im Jänner 2011

Kurzfassung

In der vorliegenden Arbeit werden laminare, schallnahe, schwach dreidimensionale Strömungen im hohen Reynoldszahlbereich in schmalen Kanälen, wie sie beispielsweise in Micro-Überschalldüsen und in Turbomaschinen mikro-elektro-mechanischer Systeme (MEMS) vorliegen, untersucht. Die Kanalhöhe sei dabei derart gering, dass die auftretende Grenzschicht mit der reibungsfreien Kernströmung zu wechselwirken beginnt und die klassische Grenzschichttheorie zusammenbricht. Das hieraus resultierende viskose - reibungsfreie Wechselwirkungsproblem wird für ideale Gase formuliert. Die reibungsfreie Kernregion und die viskose Grenzschicht im Interaktionsgebiet werden mit Hilfe von angepassten asymptotischen Entwicklungen und der Triple-Deck Theorie gelöst. Als Folge davon müssen die Grenzschicht und die Kernregion simultan berechnet werden.

Um einen ersten Einblick in die komplexe Struktur der schwach-dreidimensionalen, schallnahen Strömung zu erhalten, wurde zunächst die Strömung über einen flachen an der Kanalwand angebrachten Hügel betrachtet. Hierzu ist das linearisierte "Lower-Deck" Problem, welches analytisch gelöst wurde, betrachtet worden. Neben dem Strömungsverhalten selbst wurde weiters das asymptotische Verhalten weit strömabwärts nach dem Hügel untersucht.
Zur Untersuchung nichtlinearer Effekte, wie beispielsweise Grenzschichtablösung und dem Einfluss der Variation des schallnahen Ähnlichkeitsparameters auf die Strömung, wurden die vollen nichtlinearen "Lower-Deck-Gleichungen" mittels eines pseudo-spektralen Verfahrens numerisch gelöst. Von besonderem Interesse war hierbei die Ausbildung von Ablöseblasen an der Lee-Seite der Wanddeformation und deren Struktur.
Das Auftreten stromaufwärts wirkender Störungen sowohl unter Überschall- als auch unter Unterschallrandbedingungen wurde bezüglich ihrer Existenz und in Folge auch deren Abklingverhalten studiert. Zur Untersuchung von frei wechselwirkenden Grenzschichten, welche Eigenlösungen der Grundgleichungen darstellen, wurde die Strömung weit stromabwärts durch eine Oberflächendeformation gestört und so versucht eine freie, schwach dreidimensionale Wechselwirkung, ähnlich wie die der bekannten regularisierten Stoßprofile im zweidimensionalen Fall, auszulösen.

Abschließend wurde noch das Auftreten einer kritischen Grenzhöhe gefunden und es konnte gezeigt werden, dass keine stationären Lösungen der Strömung für Hügelhöhen über der Grenzhöhe existieren und es zu einer Lösungsverzweigung kommt. Durch die Untersuchung des lokalen Verzweigungsverhaltens konnte die Stabilität der Lösungsäste bestimmt werden. Weiters zeigte sich, dass es bei Änderung der Breite des Hügels zu Änderungen auch im Verzweigungsverhalten kommt und im zweidimensionalen Grenzfall die Verzweigungskurve vollständig degeneriert.

Abstract

In the present work laminar transonic weakly three-dimensional flows for high Reynolds numbers in slender channels, as they are found in micro supersonic nozzles and turbomachines of micro-electro-mechanical-systems (MEMS), are considered. The channel heights shall be so small that the viscous boundary layer starts to interact with the inviscid core flow and therefore the classical boundary layer approach fails. The resulting viscous-inviscid interaction problem is formulated for perfect gases. The inviscid core region and the viscous boundary layer are investigated by means of matched asymptotic expansions and triple deck theory. As a consequence, the properties of the core region and the boundary layer have to be calculated simultaneously in the interaction region.

To get a first insight into the complex structure of weakly three-dimensional transonic flows the flow over a shallow surface mounted hump was studied. Hence the linearized "Lower-Deck" problem, which was solved analytically, was investigated, Beside the flow behavior the asymptotic structure far downstream after the hump was considered.

To study nonlinear effects, as for instance boundary layer separation and changes of the flow field caused by variations of the transonic similarity parameter, the full nonlinear "Lower-Deck equations" has to be solved using a pseudo-spectral numerical method. Of special interest was the formation and topology of the separation bubbles at the lee side of the channel wall deformation.
The occurrence of upstream acting perturbations under supersonic as well as under subsonic flow conditions was studied with respect to their existence and consequently also the decay of the perturbations. To investigate freely interacting boundary layers, which are eigensolutions of the governing equations, the flow was perturbed by a surface deformation far downstream with the intention to trigger a weakly three-dimensional free interaction similar to the well known regularized shock profiles in the two-dimensional case.

Finally the appearance of a critical limiting height of the hump was found and it could be shown that there exists no steady solutions of the flow for hump heights larger than this limiting height and the solution starts to bifurcate. The local analysis of the bifurcation point yielded the stability of the solution branches. Furthermore, a change of the bifurcating behavior was found by changing the width of the hump and a fully degeneration of the bifurcation curve occurs in the limiting case of a two-dimensional wall deformation.

Acknowledgment

The present dissertation was carried out during my work as research assistant at the Institute of Fluid Mechanics and Heat Transfer, University of Technology Vienna, and financed by the Austrian Science Fund (FWF) in the framework of the "Wissenschaftskolleg - Differential Equations".

First of all I'd like to thank my advisor Prof. A. Kluwick for his continuous support and for giving me the opportunity to work with him. His remarks and suggestions were always stimulating and very constructive. During numerous talks and discussions I've learned to know him as an excellent teacher and to appreciate his rigorous enthusiasm for scientific work.
Furthermore, I'm very grateful to Prof. Ch. Schmeiser for the opportunity to take part in the WK Differential equations and to show me new, till then unknown, aspects of mathematics in particular during the summer camps at the Weissensee.
I'm also very indebted to Prof. Ph. Gittler who has kindly taken over the Co-Referat of my thesis.
Many thanks also to all of my colleagues at the Institute and the WK for the friendly, familiar atmosphere and the fruitful collaboration.
Finally, I'd like to thank my parents, family and friends, who gave me the necessary support and the chance to take my mind off the thesis from time to time.

Contents

1. Introduction **1**

2. Problem description **4**

2.1. Governing equations 5

2.2. Inspections Analysis - Orders of Magnitude 6

2.2.1. Lower Deck 6

2.2.2. Main Deck 8

2.2.3. Upper Deck 8

2.2.4. Calculation of the Orders of Magnitude of the Flow Quantities . . 9

2.3. Formal Asymptotic Expansions 11

2.3.1. Lower Deck 13

2.3.2. Main Deck 14

2.3.3. Upper Deck 16

2.4. Fundamental Lower Deck Problem 19

2.5. Fundamental Lower Deck Problem in Spectral Space 22

2.5.1. Governing Equations in Spectral Space 22

2.6. The Flow Structure 24

3. Solutions of the Linearized Problem **25**

3.1. Derivation of the Linearized Solutions in Spectral Space 25

3.2. Results of the Linearized Problem 28

3.2.1. Flow Structure under Subsonic Flow Conditions 28

3.2.2. Flow Structure under Supersonic Flow Conditions 31

3.3. Asymptotic Behavior far Downstream ($X \gg 1$) 34

3.3.1. Wall Shear Stress 34

3.3.2. Pressure Perturbation 35

4. Nonlinear Effects **37**

4.1. Boundary layer separation 37
4.2. Effects due to the transonic similarity parameter K 43

5. Upstream Influence, Free Interaction and Eigensolutions 46
5.1. Upstream Propagating Perturbations 47
5.1.1. Upstream Influence in the Two-Dimensional Case 47
5.1.2. Upstream Influence in the Weakly Three-Dimensional Case 48
5.2. Decay of the Upstream Perturbations 50
5.3. Asymptotic Structure of the Free Interaction 55
5.3.1. Free Interaction under Supersonic Flow Conditions 55
5.3.2. Free Interaction under Subsonic Flow Conditions 59
5.4. Eigensolutions and Internal Shock Structures 61
5.4.1. Slightly Deformed Two-Dimensional Hump 61
5.4.2. The Periodic Ridge 63
5.4.3. The Single Cosine-Squared Hump 65

6. Bifurcating Solutions and Local Analysis of the Bifurcation Point 67
6.1. Bifurcating Solutions 67
6.2. Local Analysis of the Bifurcation Point 69
6.3. Dependence on the hump width 74
6.4. Future work 76

7. Conclusions 77

A. List of Symbols 82

B. Pseudo Spectral Method 86
B.1. Preparation of the governing equations 86
B.2. Discretization of the Equations 88
B.3. Numerical Scheme 89
B.4. Grids and Collocation Points 90

List of Figures 92

List of Tables 95

Bibliography 96

1. Introduction

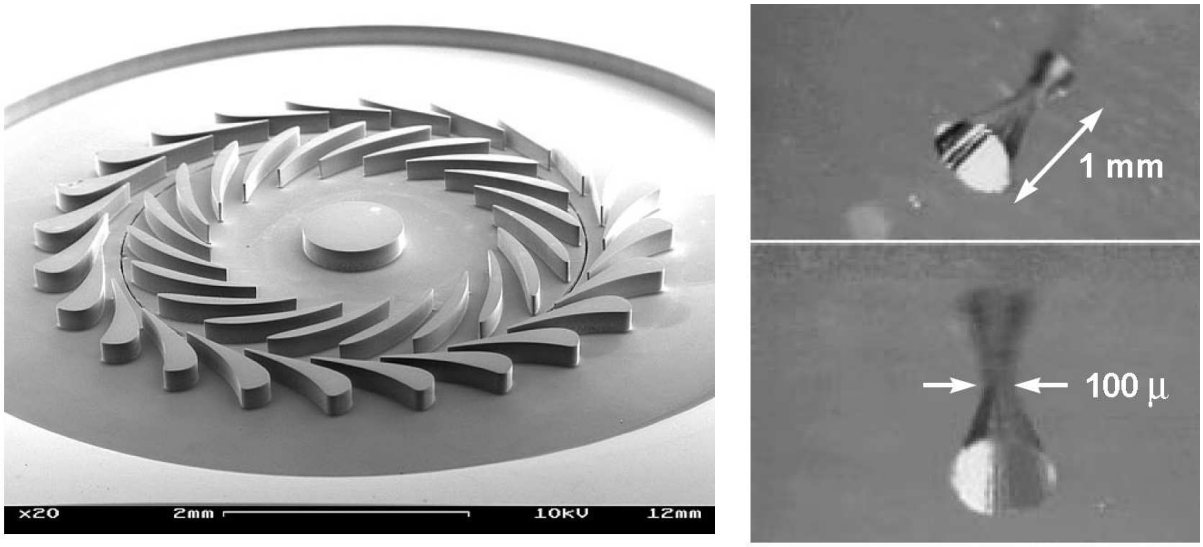

Figure 1.1.: MEMS turbine stage with 4mm diameter, A. H. Epstein, MIT Cambridge, [17] (left hand side) and supersonic micro nozzle, S.W. Janson, H. Helvajian and K. Breuer, The Aerospace Corporation, [24] (right hand side).

The rapidly expanding capability of micro machining technology has made feasible the development of gas turbines as well as micro supersonic nozzles in the millimeter size range, mainly based on semiconductor industry-derived processing of materials. Such devices are known as micro-electro-mechanical systems (MEMS), which are usually relevant to aerospace applications like the micro nozzles (thruster) for space propulsion of satellites. But due to the demand of greatly improved compact power sources for portable electronics also the development of MEMS gas turbine engines are of interest. Beside the manufacturing constraints a principle challenge is to obtain a design which also meets the requirements of fluid mechanics since the physics change also with scale. Viscous effects become more dominant at these small scales.
Typically turbomachinery tip Mach numbers in the high subsonic or low supersonic range are reached. Length scales of a few millimeters imply that a device with room

temperature inflow, such as a compressor, will operate at Reynolds numbers of the order $Re \sim 10^4$, while turbines with higher gas temperatures will operate at a Reynolds number of a few thousands and thus in a laminar regime. Therefore, viscous losses are much larger at these scales compared to large-scale turbomachinery. But viscous losses make up only about a third of the total fluid loss in a high speed turbomachine. Typically tip leakage and shock wave losses account for most of the rest. But also in large scale devices such flow conditions are found. For instance, in the channels between two leafs of a leaf seal in a large scale turbomachine, cf. [37], [23], similar conditions are found.
Another aspect on these small scales is the influence of surface roughness onto the flow, which is known to be capable to trigger weak compression shocks. Hence, a region of special interest is the transonic regime, where the Mach number is close to it's critical value $M = 1$ and the flow is very sensitive to perturbations.
Unless the channels in such devices are extremely small, the fluid behavior can still be represented as continuum flow so that molecular kinetics and Knudsen number considerations are not important.
Thus, steady viscous inviscid interactions taking place in transonic laminar continuum flows through narrow channels shall be considered. Rapid changes of the flow field in the streamwise direction, such as the formation of weak normal shocks or the presence of a local channel wall deformation due to surface roughness, eventually in connection with boundary layer separation, yield a breakdown of the classical boundary layer approach. As a consequence, the properties of the inviscid core region and the viscous boundary layer region has to be calculated simultaneously in the interaction region.
Previous work done in the context of viscous inviscid interaction in slender channels is given by Kluwick [26], Kluwick and Gittler [29], Kluwick, Braun and Gittler [28] and Kluwick and Meyer [30], who studied two-dimensional transonic laminar internal flows. The extension to their work covers, in particular, weakly three-dimensional effects which are to be included properly in the formulation of the interaction problem. In summary the current thesis is concerned with the following objectives.

- Formulation of the weakly three-dimensional interaction problem as presented in chapter 2.

- The investigation of the flow around sufficiently shallow wall deformations in the limit of the linearized problem as performed in chapter 3. Furthermore, the asymptotic properties of the flow quantities far downstream are to be treated by analyzing the linearized problem in spectral space for vanishing small values of the spectral

variables k and l.

- Investigation of the effect of boundary layer separation, specially on the formation and topography of separation bubbles using a pseudo spectral method for solving the full nonlinear problem as done in chapter 4. To validate the results significant values, like the separation angle, shall be compared to well known analytical approximations. Another aspect to be discussed is the effect of the transonic similarity parameter K on the flow behavior under supersonic as well as under subsonic flow conditions and associated effects.

- The analytical study of the occurrence of upstream acting perturbations and the calculation of their proper upstream decay as presented in section 5.1 to 5.2. Completed by a numerical investigation of the formation of weakly three-dimensional freely interacting boundary layers similar to the compressive shock profiles regularized by viscous inviscid interaction.

- The capability of three-dimensional transonic flows to bifurcate, the associated problem of flow stability taking place in such narrow channel flows perturbed by wall deformations and a local analysis of the bifurcation point shall be presented in chapter 6. These stability problems are features frequently encountered in technical applications and of major interest specially in the design of turbomachineries and nozzles.

Two-dimensional CFD-simulations of viscous effects in supersonic micro nozzles can be found in [2],[34],[21],[40], further related works on numerical simulations of shock waves in micro nozzles e.g. in [57] and experimental studies on flow visualization and pressure measurement in micro nozzles in [22], [42] among others.
Related analytical works on viscous inviscid interactions in internal purely supersonic flows can be found in [44],[4] and works on purely subsonic viscous inviscid interactions in [48] .

2. Problem description

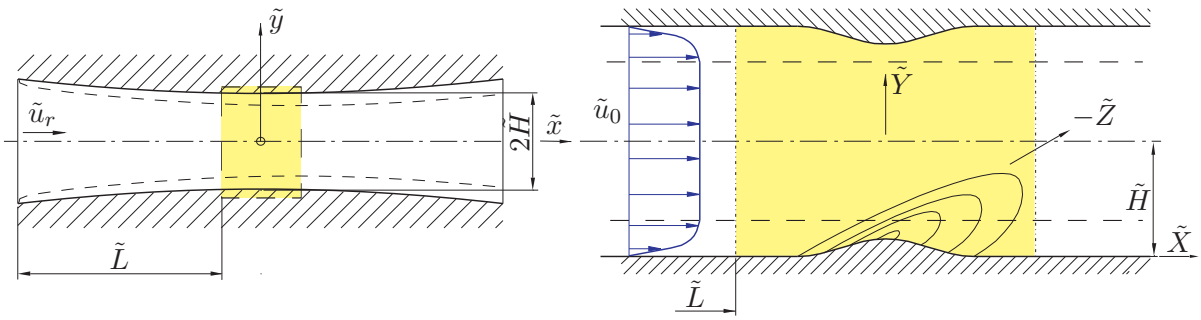

Figure 2.1.: Slender Laval nozzle with interaction region.

The transonic flow through a slender nozzle of height $2\tilde{H}$, see figure 2.1, is considered. Due to the symmetry in y-direction it is sufficient to study just one half of the channel. The Reynolds number shall be large thus generating a two-dimensional boundary layer at the channel walls, indicated by the dashed lines in figure 2.1, whose effect on the global flow behavior is not negligible anymore due to the slenderness of the channel. Specially we assume that this boundary layer starts to interact with the inviscid outer flow at a length $\tilde{L}$ and therefore classical boundary layer theory, see L. Prandtl [41], fails in this region. These rapid changes of the flow quantities in the viscous inviscid interaction region can be caused by a shallow weakly three-dimensional surface mounted obstacle or by the formation of a weak shock in the inviscid core region, respectively.
The breakdown of the hierarchical structure of the classical boundary layer theory can be overcome by introducing a triple deck structure, first formulated by Stewartson, Messiter and Neiland, cf. [50], [35], [38], and described by means of matched asymptotic expansions, cf. M. VanDyke [54]. First the governing equations in non-dimensional form are provided and then afterwards the order of magnitude of the various quantities will be discussed from a physical point of view.

2.1. Governing equations

The non-dimensional quantities are introduced in the following way

$$\begin{array}{llll} \mathbf{x} = \frac{\tilde{\mathbf{x}}}{\tilde{L}}, & H = \frac{\tilde{H}}{\tilde{L}}, & \boldsymbol{s_h} = \frac{\tilde{\boldsymbol{S}}}{\tilde{L}}, & \mathbf{u} = \frac{\tilde{\mathbf{u}}}{\tilde{u}_0}, \\ p = \frac{\tilde{p}}{\tilde{u}_0^2 \tilde{\rho}_0}, & \rho = \frac{\tilde{\rho}}{\tilde{\rho}_0}, & t = \frac{\tilde{t}\tilde{L}}{\tilde{u}_0}, & \theta = \frac{\tilde{\theta}}{\tilde{\theta}_0}, \\ h = \frac{\tilde{h}}{\tilde{u}_0^2}, & s = \frac{\tilde{s}}{\tilde{c}_{p0}}, & \mu = \frac{\tilde{\mu}}{\tilde{\mu}_0}, & k_\lambda = \frac{\tilde{k_\lambda}}{\tilde{k}_{\lambda,0}}, \\ c = \frac{\tilde{c}}{\tilde{c}_0}, & \boldsymbol{\tau} = \frac{\tilde{\boldsymbol{\tau}}\tilde{L}}{\tilde{\mu}_0 \tilde{u}_0}, & \boldsymbol{q} = \frac{\tilde{\mathbf{q}}\tilde{L}}{\tilde{k}_{\lambda,0}\tilde{\theta}_0}, & \end{array} \tag{2.1}$$

where tilde denotes dimensional quantities and the subscript 0 indicates a reference state. An adequate reference state for the problem is the state just upstream of the interaction region at the position $\tilde{L}$ in the undisturbed core region.

In the listing 2.1 of the relevant physical quantities just above $\tilde{\boldsymbol{x}}$ denotes the position vector with the horizontal, vertical and lateral components $(\tilde{x}, \tilde{y}, \tilde{z})$, $\tilde{H}$ the half height of the channel, $\tilde{\boldsymbol{S}}$ the vector describing the surface of the mounted obstacle, $\tilde{\mathbf{u}}$ the velocity vector with the horizontal, vertical and lateral components $(\tilde{u}, \tilde{v}, \tilde{w})$, $\tilde{p}$ the pressure, $\tilde{\rho}$ the density, $\tilde{t}$ the time, $\tilde{\theta}$ the temperature, $\tilde{h}$ the specific enthalpy, $\tilde{s}$ the specific entropy, $\tilde{c_{p0}}$ the specific heat at constant pressure, $\tilde{\mu}$ the dynamic viscosity, $\tilde{k_\lambda}$ the thermal conductivity and $\tilde{c}$ the speed of sound.

The fluid motion is described by the Navier-Stokes equations for compressible flows, cf. A. H. Shapiro [46], consisting of the continuity equation ensuring the conservation of mass, the momentum equations in three spatial directions as well as the energy equation ensuring the conservation of energy. This set of equations (neglecting the gravitational forces) can be written in the following non-dimensional form

$$\frac{\partial \rho}{\partial t} + \nabla \cdot (\rho \mathbf{u}) = 0, \tag{2.2a}$$

$$\rho \left(\frac{\partial \mathbf{u}}{\partial t} + (\mathbf{u} \cdot \nabla)\mathbf{u} \right) = -\nabla p + \frac{1}{Re} \nabla \cdot \boldsymbol{\tau}, \tag{2.2b}$$

$$\rho \frac{Dh}{Dt} - \frac{Dp}{Dt} = \frac{1}{Re} \left[\nabla \cdot (\boldsymbol{\tau u}) - \boldsymbol{u}(\nabla \cdot \boldsymbol{\tau}) \right] - \frac{1}{PrReEc} \nabla \cdot \mathbf{q}, \tag{2.2c}$$

where $\boldsymbol{\tau}$ is the viscous stress tensor and $\boldsymbol{q}$ the vector of the heat flux. The dimensionless parameters entering the governing equations are the Reynolds number $Re := \frac{\tilde{\rho}_0 \tilde{u}_0 \tilde{L}}{\tilde{\mu}_0}$, the Prandtl number $Pr := \frac{\tilde{\mu}_0 \tilde{c_{p0}}}{\tilde{k}_{\lambda,0}}$ and the Eckert number $Ec := \frac{\tilde{u}_0^2}{\tilde{c_{p0}} \tilde{\theta}_0}$. Another important dimensionless parameter appearing later is the Mach number $M_0 := \frac{\tilde{u}_0}{\tilde{c}_0}$. In the following it will be assumed that the Reynolds number is large $Re \gg 1$ and the Mach number is

close to its critical value $M_0 = 1$, while the Prandtl number Pr and the Eckert number Ec are taken to be of $\mathcal{O}(1)$.
Due to the symmetry with respect to the centerline of the nozzle ($Y = H$) the boundary conditions have to be specified for one half of the channel only. These are in general a no-slip condition at the wall and a matching condition with the oncoming undisturbed two-dimensional boundary layer. A detailed discussion of the boundary conditions is carried out in the subsequent sections.
To close the problem we assume a Newtonian fluid defined by, cf. [43],

$$\boldsymbol{\tau} = \mu \left(\nabla \mathbf{u}^T + (\nabla \mathbf{u}^T)^T - \frac{2}{3}(\nabla \cdot \mathbf{u})\mathbf{I} \right), \tag{2.3}$$

satisfying Fourier's law for the heat conduction

$$\mathbf{q} = -k_\lambda \nabla \theta, \tag{2.4}$$

as well as caloric and thermal equations of state

$$h = h(p, s), \quad p = p(\rho, \theta). \tag{2.5}$$

2.2. Inspections Analysis - Orders of Magnitude

Under the assumption that the interaction region exhibits a triple deck structure, consisting of a viscous lower deck, a passive main deck and an irrotational inviscid upper deck as sketched in figure 2.2, and taking into account the nature of these decks one can derive relations for the order of magnitudes of the flow quantities as well as the relevant length scales. Inspecting the governing equations and balancing the terms from a physical point of view in the individual decks reveals the subsequent relations.

2.2.1. Lower Deck

The variations of the dimensionless lower deck quantities are defined as

$$u_l = \frac{\tilde{u}_l}{\tilde{u}_0} = \Delta u_l, \;\; v_l = \frac{\tilde{v}_l}{\tilde{u}_0} = \Delta v_l, \;\; w_l = \frac{\tilde{w}_l}{\tilde{u}_0} = \Delta w_l, \tag{2.6a}$$

$$p_l - p_0 = \frac{\tilde{p}_l - \tilde{p}_0}{\tilde{u}_0^2 \tilde{\rho}_0} = \Delta p_l, \;\; \rho_l = \frac{\tilde{\rho}_l}{\tilde{\rho}_0} = R_w + \Delta \rho_l, \tag{2.6b}$$

where the subscript w denotes quantities evaluated at the channel wall. Taking the viscous character of the lower deck into account results in the following estimates:

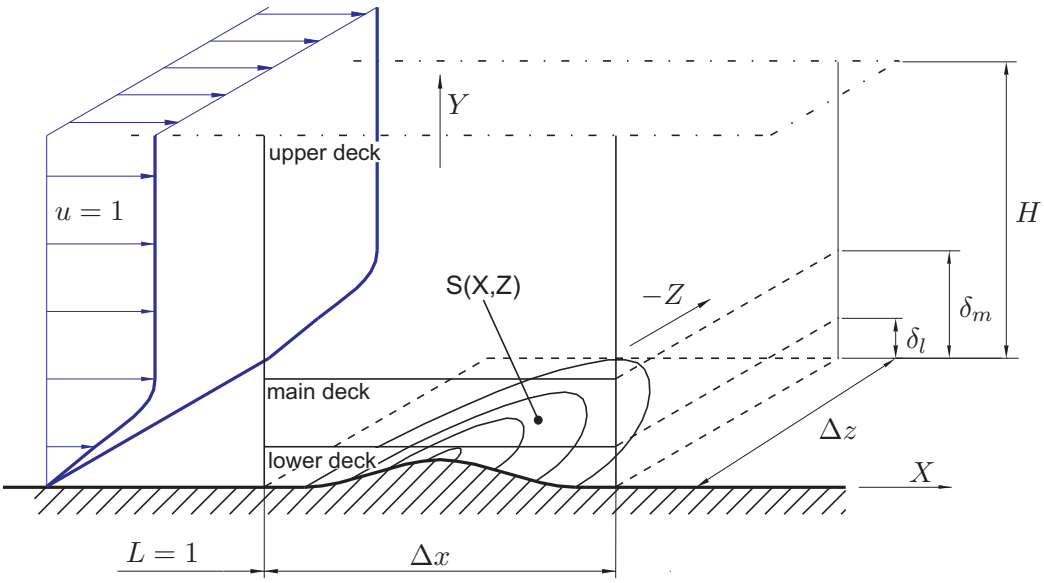

Figure 2.2.: Tripledeck structure of the viscous inviscid interaction region.

• Thin lower deck compared to the main deck

$$\Delta u_l \sim \delta_l \delta_m^{-1}. \tag{2.7}$$

• Balance of inertia and pressure term in x-momentum equation

$$\Delta u_l^2 \sim \Delta p_l. \tag{2.8}$$

• Balance of inertia and viscous term in x-momentum equation

$$\Delta u_l \frac{\Delta u_l}{\Delta x} \sim \frac{1}{Re} \frac{\Delta u_l}{\delta_l^2}. \tag{2.9}$$

• Balance of inertia and pressure term in z-momentum equation

$$\Delta u_l \frac{\Delta w_l}{\Delta x} \sim \frac{\Delta p_l}{\Delta z}. \tag{2.10}$$

• Non-degenerate continuity equation

$$\frac{\Delta u_l}{\Delta x} \sim \frac{\Delta v_l}{\delta_l}. \tag{2.11}$$

• Pressure disturbance in lower deck imposed by outer flow

$$\Delta p_l \sim \Delta p_u. \tag{2.12}$$

2.2.2. Main Deck

The dimensionless main deck quantities

$$u_m = \frac{\tilde{u}_m}{\tilde{u}_0} = U_0 + \Delta u_m, \;\; v_m = \frac{\tilde{v}_m}{\tilde{u}_0} = \Delta v_m, \;\; w_m = \frac{\tilde{w}_m}{\tilde{u}_0} = \Delta w_m, \tag{2.13a}$$

$$p_m - p_0 = \frac{\tilde{p}_m - \tilde{p_0}}{\tilde{u}_0^2 \tilde{\rho}_0} = \Delta p_m, \;\; \rho_m = \frac{\tilde{\rho}_m}{\tilde{\rho}_0} = R_0 + \Delta \rho_m \tag{2.13b}$$

are split into a small deviation from the oncoming two-dimensional boundary layer and the boundary layer flow itself, where U_0 and R_0 denote the velocity and the density profile of the oncoming boundary layer, respectively. Taking the passive nature of the main deck into account yields the following relations:

• Balance with the lower deck shift of the velocity profile

$$\Delta u_m \sim \Delta u_l. \tag{2.14}$$

• Displacement shifted to the upper deck

$$\Delta v_m \sim \Delta v_u. \tag{2.15}$$

• Balance of inertia and pressure term in z-momentum equation

$$\Delta u_m \frac{\Delta w_m}{\Delta x} \sim \frac{\Delta p_m}{\Delta z}. \tag{2.16}$$

• Non-degenerate continuity equation

$$\frac{\Delta u_m}{\Delta x} \sim \frac{\Delta v_m}{\delta_m}. \tag{2.17}$$

• Pressure disturbance in main deck imposed by outer flow

$$\Delta p_m \sim \Delta p_u. \tag{2.18}$$

2.2.3. Upper Deck

The dimensionless upper deck quantities

$$u_u = \frac{\tilde{u}_u}{\tilde{u}_0} = 1 + \Delta u_u, \;\; v_u = \frac{\tilde{v}_u}{\tilde{u}_0} = \Delta v_u, \;\; w_u = \frac{\tilde{w}_u}{\tilde{u}_0} = \Delta w_u, \tag{2.19a}$$

$$p_u - p_0 = \frac{\tilde{p}_u - \tilde{p_0}}{\tilde{u}_0^2 \tilde{\rho}_0} = \Delta p_u, \;\; \rho_u = \frac{\tilde{\rho}_u}{\tilde{\rho}_0} = 1 + \Delta \rho_u \tag{2.19b}$$

are again split into a small deviation from the oncoming one-dimensional flow in the core region and the flow in the core region itself. Taking the inviscid irrotational character of the upper deck into account gives the following relations:

• Planar weakly disturbed flow in the upper deck

$$\Delta\rho_u \sim \Delta p_u \sim \Delta u_u. \tag{2.20}$$

• Displacement effect shifted by main deck shall lead to a flow response at leading order

$$\frac{\Delta u_u^2}{\Delta x} \sim \frac{\Delta v_u}{H} \sim \frac{\Delta w_u}{\Delta z}. \tag{2.21}$$

• Transonic flow

$$\Delta u_u \sim \mid 1 - M_0^2 \mid \sim \Delta K. \tag{2.22}$$

• Irrotational flow

$$\frac{\Delta w_u}{\Delta x} \sim \frac{\Delta u_u}{\Delta z}, \tag{2.23a}$$

$$\frac{\Delta u_u}{\Delta z} \sim \frac{\Delta w_u}{\Delta x}, \tag{2.23b}$$

$$\frac{\Delta w_u}{H} \sim \frac{\Delta v_u}{\Delta z}, \tag{2.23c}$$

where the y-depending terms will be discussed in detail in the next section.

The time scaling preserving the slowest timescales and therefore governing the longterm behavior of the system can be estimated from a physical point of view by studying the speed of an upstream propagating wave, which gives in the limit $M_0 \to 1$

$$\frac{\Delta x}{\Delta t} \sim \Delta u_u. \tag{2.24}$$

Another approach is to require, that the time must enter the analysis at the level of the solvability condition, which will give exactly the same result as the earlier approach.

2.2.4. Calculation of the Orders of Magnitude of the Flow Quantities

Combining the estimates (2.7) - (2.12), (2.14) - (2.18), (2.20) - (2.23) and introducing a small expansion parameter $\varepsilon \ll 1$, measuring the perturbation of the streamwise velocity component Δu_u, gives the following ansatz for the orders of magnitude of the changes of the flow quantities in the three decks.

$$
\begin{aligned}
&\Delta u_l \sim \varepsilon, && \Delta v_l \sim \varepsilon^{l_v}, && \Delta w_l \sim \varepsilon^{l_w}, && \\
&\Delta u_m \sim \varepsilon^{m_u}, && \Delta v_m \sim \varepsilon^{m_v}, && \Delta w_m \sim \varepsilon^{m_w}, && \\
&\Delta u_u \sim \varepsilon^{n_u}, && \Delta v_u \sim \varepsilon^{n_v}, && \Delta w_u \sim \varepsilon^{n_w}, && \Delta \rho_u \sim \varepsilon^{n_\rho}, \\
&\Delta x \sim \varepsilon^{k_x}, && \Delta z \sim \varepsilon^{k_z}, && \delta \sim \varepsilon^{k_{\delta,l}}, && H \sim \varepsilon^{k_H}, \\
&\Delta p \sim \Delta p_l \sim \Delta p_m \sim \Delta p_u \sim \varepsilon^{n_p}, && && \Delta K \sim \varepsilon^{k_K}. &&
\end{aligned}
$$

Keeping in mind that the main deck contains the main part of the oncoming boundary layer yields

$$Re^{-\frac{1}{2}} \sim \varepsilon^{k_{\delta,m}}.$$

Inserting the above ansatz into equation (2.7) to (2.23a) gives the following 15 relations for the 16 unknowns

$$
\begin{aligned}
&\varepsilon \sim \varepsilon^{k_{\delta,l}-k_{\delta,m}}, && \varepsilon^2 \sim \varepsilon^{n_p}, && \varepsilon^{2-k_x} \sim \varepsilon^{1-2k_{\delta,l}+2k_{\delta,m}}, \\
&\varepsilon^{1+l_w-k_x} \sim \varepsilon^{n_p-k_z}, && \varepsilon^{1-k_x} \sim \varepsilon^{l_v-k_{\delta,l}}, && \varepsilon \sim \varepsilon^{m_u}, \\
&\varepsilon^{m_v} \sim \varepsilon^{n_v}, && \varepsilon^{m_u+m_w-k_x} \sim \varepsilon^{n_p-k_z}, && \varepsilon^{m_u-k_x} \sim \varepsilon^{m_v-k_{\delta,m}}, \\
&\varepsilon^{n_\rho} \sim \varepsilon^{n_u}, && \varepsilon^{n_u} \sim \varepsilon^{n_p}, && \varepsilon^{2n_u-k_x} \sim \varepsilon^{n_v-k_H}, \\
&\varepsilon^{2n_u-k_x} \sim \varepsilon^{n_w-k_z}, && \varepsilon^{n_u-k_z} \sim \varepsilon^{n_w-k_x}, && \varepsilon^{k_K} \sim \varepsilon^{n_u}.
\end{aligned}
$$

The flow in the upper deck shall be planar to the leading order and a y-dependency of the quantities shall enter at the next higher order. This condition is enforced by the shallowness of the channel, i.e. the requirement that the height of the channel is sufficiently small. A more precise condition for the channel height is given at the end of this section. Therefore the horizontal velocity component u_u can be expanded as follows

$$u_u = 1 + \varepsilon^{n_u} u_u^{(1)}(x, z) + \sum_i \varepsilon^{n_u \cdot i} u_u^{(i)}(x, y_u, z)$$

and consequently the derivative with respect to y is found to be

$$\left(\frac{\partial u}{\partial y}\right)_u \sim \sum_i \varepsilon^{n_u \cdot i} \frac{\partial}{\partial y_u} u_u^{(i)}(x, y_u, z) \frac{dy_u}{dy}.$$

Thus the expression for irrotational flow in the upper deck (2.23b) can be used to make the following estimate[1]

$$\varepsilon^{2n_u-k_H} \sim \varepsilon^{n_v-k_x}.$$

[1] Another estimate is given by G. Meyer [36], assuming no y-dependency of the flow in the upper deck also at higher orders.

Comparison of the exponents of ε in the stated expressions yields the following 16 linear equations for 16 unknowns

$$
\begin{array}{lll}
k_{\delta,l} - k_{\delta,m} = 1, & n_p = 2, & k_x - 2k_{\delta,l} + 2k_{\delta,m} = 1, \\
-l_w + n_p - k_x - k_z = 1, & l_v + k_x - k_{\delta,l} = 1, & m_u = 1, \\
m_v - n_v = 0, & m_u + m_w - n_p - k_x + k_z = 0, & m_u - m_v - k_x - k_{\delta,m} = 0, \\
-n_u + n_\rho = 0, & n_u - n_p = 0, & 2n_u - n_v - k_x + k_H = 0, \\
2n_u - n_w - k_x + k_z = 0, & n_u - n_w + k_x - k_z = 0, & -n_u + k_K = 0, \\
 & -2n_u + n_v - k_x + k_H = 0 &
\end{array}
$$

which have the solutions

$$
\begin{array}{llll}
l_v = 5, & l_w = 2, & m_u = 1, & m_v = 4, \\
m_w = 3, & n_u = 2, & n_v = 4, & n_w = 3, \\
n_\rho = 2, & n_p = 2, & k_x = 3, & k_z = 2, \\
k_{\delta,l} = 7, & k_{\delta,m} = 6, & k_H = 3, & k_K = 2.
\end{array}
$$

And finally from $\delta_m \sim Re^{-\frac{1}{2}}$ the small perturbation parameter ε is found to be

$$\varepsilon = Re^{-\frac{1}{12}}. \tag{2.25}$$

The number of reflections of the characteristics n in the upper deck can be estimated by

$$n \sim \frac{\Delta x}{H\sqrt{M_0^2 - 1}},$$

where for $n \to \infty$ the y-dependence of the flow quantities become negligible small and yields the following condition for the channel height

$$H = o\left(\frac{\Delta x}{\Delta K}\right) = o(\varepsilon^2) = o(Re^{-1/6}),$$

which is satisfied with the above stated length scales.

2.3. Formal Asymptotic Expansions

The inspection analysis carried out in the previous section suggests formal asymptotic expansions for the flow quantities in the different decks of the interaction region characterized by different length scales in horizontal, vertical and lateral direction. Substituting in the governing equations and evaluating in leading order yields the distinguished limits for each deck. Via matching of the different solutions of the neighboring asymptotic

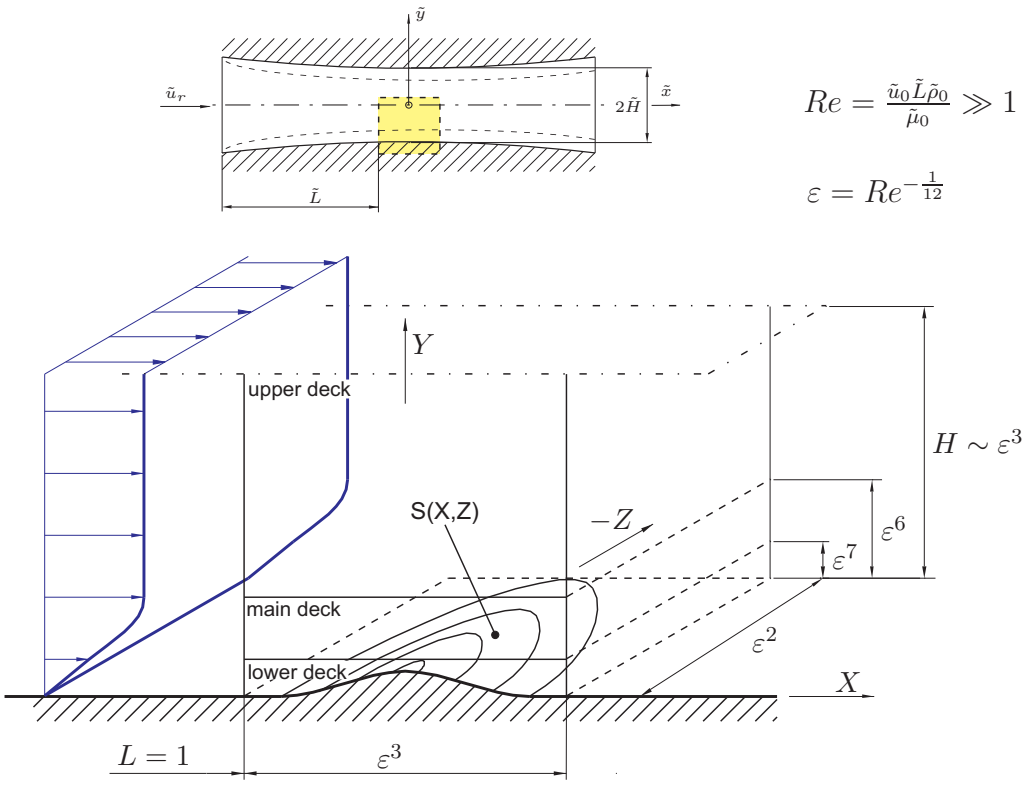

Figure 2.3.: Tripledeck structure and length scales of the interaction region.

regions an uniformly valid solution can be found, cf. [54]. Since the derivation of the fundamental problem for the weakly three-dimensional case does not differ a lot from the two-dimensional case studied by A. Kluwick and G. Meyer, cf. [30], as well as from the standard triple deck theory for the lower deck and the main deck, see i.e. [26], [50], these equations will be introduced without much further explanations.
The inspections analysis in section 2.2 suggests for the spatial scalings of the streamwise and lateral coordinate

$$x = 1 + \varepsilon^3 \bar{X}, \tag{2.26a}$$

$$z = \varepsilon^2 \bar{Z}, \tag{2.26b}$$

which are, of course, the same in all three decks. The time scaling is found to be

$$t = \varepsilon \bar{t}. \tag{2.27}$$

2.3.1. Lower Deck

Inspection analysis in section 2.2.1 suggests for the spatial scalings in y-direction

$$y_l = \varepsilon^7 \bar{Y}_l, \tag{2.28}$$

and the following asymptotic expansions for the relevant quantities

$$u_l = \varepsilon \bar{U}_{l,1}(\bar{X}, \bar{Y}_l, \bar{Z}, \bar{t}) + \mathcal{O}(\varepsilon^2), \tag{2.29a}$$
$$v_l = \varepsilon^5 \bar{V}_{l,1}(\bar{X}, \bar{Y}_l, \bar{Z}, \bar{t}) + \mathcal{O}(\varepsilon^6), \tag{2.29b}$$
$$w_l = \varepsilon^2 \bar{W}_{l,1}(\bar{X}, \bar{Y}_l, \bar{Z}, \bar{t}) + \mathcal{O}(\varepsilon^3), \tag{2.29c}$$
$$\rho_l = R_w + \varepsilon^2 \bar{\rho}_{l,1}(\bar{X}, \bar{Y}_l, \bar{Z}, \bar{t}) + \mathcal{O}(\varepsilon^3), \tag{2.29d}$$
$$p_l = \varepsilon^2 \bar{P}_{l,1}(\bar{X}, \bar{Z}, \bar{t}) + \mathcal{O}(\varepsilon^3), \tag{2.29e}$$

and

$$\mu_l = \mu_w + \mathcal{O}(\varepsilon^3). \tag{2.30}$$

The subscript w denotes quantities evaluated at the channel wall. The density evaluated at the wall R_w can be considered constant over the horizontal length scale of the interaction region of $\mathcal{O}(\varepsilon^3)$ in case of an adiabatic wall.
Substituting the asymptotic expansions (2.29) in the governing equations yields to leading order the following set of equations,
the continuity equation

$$\frac{\partial \bar{U}_{l,1}}{\partial \bar{X}} + \frac{\partial \bar{V}_{l,1}}{\partial \bar{Y}_l} = 0, \tag{2.31}$$

the x-momentum equation

$$R_w \left(\bar{U}_{l,1} \frac{\partial \bar{U}_{l,1}}{\partial \bar{X}} + \bar{V}_{l,1} \frac{\partial \bar{U}_{l,1}}{\partial \bar{Y}_l} \right) = -\frac{\partial \bar{P}_{l,1}}{\partial \bar{X}} + \mu_w \frac{\partial^2 \bar{U}_{l,1}}{\partial \bar{Y}_l{}^2}, \tag{2.32}$$

the y-momentum equation

$$\frac{\partial \bar{P}_{l,1}}{\partial \bar{Y}_l} = 0 \tag{2.33}$$

and the z-momentum equation

$$R_w \left(\bar{U}_{l,1} \frac{\partial \bar{W}_{l,1}}{\partial \bar{X}} + \bar{V}_{l,1} \frac{\partial \bar{W}_{l,1}}{\partial \bar{Y}_l} \right) = -\frac{\partial \bar{P}_{l,1}}{\partial \bar{Z}} + \mu_w \frac{\partial^2 \bar{W}_{l,1}}{\partial \bar{Y}_l{}^2}. \tag{2.34}$$

The no-slip condition at the wall yields the following boundary conditions

$$\bar{U}_{l,1} = \bar{V}_{l,1} = \bar{W}_{l,1} = 0 \qquad \text{at } \bar{Y}_l = S(\bar{X}, \bar{Z}, \bar{t}) \tag{2.35}$$

with the scaled height $s_h = \varepsilon^7 S(\bar{X}, \bar{Z})$ of a surface mounted obstacle, see figure 2.3. Equations (2.31) to (2.34) are so far identical to Prandtl's boundary layer equations in incompressible form for weakly three-dimensional flows. However, new conditions arise out of the matching of the asymptotic expressions for the flow quantities in the lower deck with those in the undisturbed boundary layer upstream of the interaction region and with those of the main deck, respectively. The matching procedure with the undisturbed boundary layer gives

$$\lim_{\bar{X}\to-\infty} \bar{P}_{l,1}(\bar{X}, \bar{Z}, \bar{t}) = 0, \tag{2.36a}$$

$$\lim_{\bar{X}\to-\infty} \bar{U}_{l,1}(\bar{X}, \bar{Y}_l, \bar{Z}, \bar{t}) = U_0'(0)\bar{Y}_l, \tag{2.36b}$$

$$\lim_{\bar{X}\to-\infty} \bar{V}_{l,1}(\bar{X}, \bar{Y}_l, \bar{Z}, \bar{t}) = 0, \tag{2.36c}$$

$$\lim_{\bar{X}\to-\infty} \bar{W}_{l,1}(\bar{X}, \bar{Y}_l, \bar{Z}, \bar{t}) = 0. \tag{2.36d}$$

The matching procedure with the main deck, using the results for the governing equations in the main deck obtained in the following section, results in

$$\lim_{\bar{Y}_l\to\infty} \left[\bar{U}_{l,1}(\bar{X}, \bar{Y}_l, Z, \bar{t}) - U_0'(0)\left(\bar{Y}_l + \bar{A}_1(\bar{X}, \bar{Z}, \bar{t})\right)\right] = 0, \tag{2.37a}$$

$$\lim_{\bar{Y}_l\to\infty} \left[\bar{W}_{l,1}(\bar{X}, \bar{Y}_l, Z, \bar{t}) + \frac{1}{U_0(0)R_0(0)} \int_{-\infty}^{\bar{X}} \frac{\partial \bar{P}_{l,1}(\zeta, \bar{Z}, \bar{t})}{\partial \bar{Z}, \bar{t}} d\zeta\right] = 0, \tag{2.37b}$$

$$\bar{P}_{l,1}(\bar{X}, \bar{Z}, \bar{t}) = \bar{P}_{m,1}(\bar{X}, \bar{Z}, \bar{t}). \tag{2.37c}$$

$\bar{A}_1$ can be interpreted as the negative disturbance of the displacement thickness and is part of the solution of the main deck equations.

2.3.2. Main Deck

The inspection analysis in section 2.2 suggests for the spatial scalings in y-direction

$$y_m = \varepsilon^6 \bar{Y_m} = Re^{-\frac{1}{2}} \bar{Y_m}. \tag{2.38}$$

The scaling of the vertical coordinate in the main deck is the same as for the "classical" oncoming boundary layer indicating, as mentioned already earlier, that the main deck comprises the main part of the oncoming boundary layer. The following formal asymptotic expansions for the flow quantities are determined by superimposing the undisturbed boundary layer profile evaluated at the beginning of the interaction region $L = 1$ with

the perturbations of these quantities. Consequently the asymptotic expansions can be written as

$$u_m = U_0(\bar{Y_m}) + \varepsilon \bar{U}_{m,1}(\bar{X}, \bar{Y_m}, \bar{Z}, \bar{t}) + \mathcal{O}(\varepsilon^2), \tag{2.39a}$$

$$v_m = \varepsilon^4 \bar{V}_{m,1}(\bar{X}, \bar{Y_m}, \bar{Z}, \bar{t}) + \mathcal{O}(\varepsilon^5), \tag{2.39b}$$

$$w_m = \varepsilon^3 \bar{W}_{m,1}(\bar{X}, \bar{Y_m}, \bar{Z}, \bar{t}) + \mathcal{O}(\varepsilon^4), \tag{2.39c}$$

$$\rho_m = R_0(\bar{Y_m}) + \varepsilon \bar{\rho}_{m,1}(\bar{X}, \bar{Y_m}, \bar{Z}, \bar{t}) + \mathcal{O}(\varepsilon^2), \tag{2.39d}$$

$$p_m = \varepsilon^2 \bar{P}_{m,1}(\bar{X}, \bar{Z}, \bar{t}) + \mathcal{O}(\varepsilon^3), \tag{2.39e}$$

$$\theta_m = \Theta_0(\bar{Y_m}) + \varepsilon \bar{\Theta}_{m,1}(\bar{X}, \bar{Y_m}, \bar{Z}, \bar{t}) + \mathcal{O}(\varepsilon^2), \tag{2.39f}$$

and

$$\mu_l = \mu_w + \mathcal{O}(\varepsilon^3). \tag{2.40}$$

The leading order approximation of the governing equations can be obtained straightforwardly just by inserting the asymptotic expansions into the main deck equations. Hence the main deck equations are found to be

$$\frac{\partial}{\partial \bar{X}}(R_0 \bar{U}_{m,1} + U_0 \rho_{m,1}) + \frac{\partial}{\partial \bar{Y_m}}(R_0 \bar{V}_{m,1}) = 0, \tag{2.41a}$$

$$U_0 \frac{\partial \bar{U}_{m,1}}{\partial \bar{X}} + \bar{V}_{m,1} \frac{\partial U_0}{\partial \bar{Y_m}} = 0, \tag{2.41b}$$

$$\frac{\partial \bar{P}_{m,1}}{\partial \bar{Y_m}} = 0, \tag{2.41c}$$

$$\bar{W}_{m,1} = -\frac{1}{R_0 U_0} \int_{-\infty}^{\bar{X}} \frac{\partial \bar{P}_{m,1}(\zeta, \bar{Z})}{\partial \bar{Z}} d\zeta, \tag{2.41d}$$

$$U_0 \frac{\partial \bar{\rho}_{m,1}}{\partial \bar{X}} + \bar{V}_{m,1} \frac{dR_0}{d\bar{Y_m}} = 0, \tag{2.41e}$$

the leading order representation of the continuity equation, the x-momentum equation, the y-momentum equation, the z-momentum equation and the energy equation, respectively. The passive nature of the main deck is highlighted by the fact, that no dissipative terms enter the equations, which also can be observed from the general solution

$$\bar{U}_{m,1} = \bar{A}_1(\bar{X}, \bar{Z}, \bar{t}) U_0'(\bar{Y_m}), \tag{2.42a}$$

$$\bar{V}_{m,1} = -\frac{\partial \bar{A}_1(\bar{X}, \bar{Z}, \bar{t})}{\partial \bar{X}} U_0(\bar{Y_m}), \tag{2.42b}$$

$$\bar{W}_{m,1} = -\frac{1}{R_0 U_0} \int_{-\infty}^{\bar{X}} \frac{\partial \bar{P}_{m,1}(\zeta, \bar{Z}, \bar{t})}{\partial \bar{Z}} d\zeta, \tag{2.42c}$$

$$\bar{\rho}_{m,1} = \bar{A}_1(\bar{X}, \bar{Z}, \bar{t}) R_0'(\bar{Y_m}), \tag{2.42d}$$

$$\bar{P}_{m,1} = \bar{P}_{m,1}(\bar{X}, \bar{Z}, \bar{t}), \tag{2.42e}$$

where the function $\bar{A}_1$ can be interpreted as the negative disturbance of the displacement thickness of the undisturbed boundary layer as pointed out before. The matching with the lower deck solutions has been performed in the previous subsection, cf. (2.37). And the matching of the main deck solutions with the upper deck solutions yields

$$\lim_{\bar{Y_m}\to\infty} \bar{U}_{m,1}(\bar{X},\bar{Y_m},\bar{Z},\bar{t}) = \lim_{\bar{Y_m}\to\infty} \bar{\rho}_{m,1}(\bar{X},\bar{Y_m},\bar{Z},\bar{t}) = 0, \tag{2.43a}$$

$$\lim_{\bar{Y_m}\to\infty} \bar{V}_{m,1}(\bar{X},\bar{Y_m},\bar{Z},\bar{t}) = -\frac{\partial \bar{A}_1}{\partial \bar{X}}, \tag{2.43b}$$

$$\lim_{\bar{Y_m}\to\infty} \bar{W}_{m,1}(\bar{X},\bar{Y_m},\bar{Z},\bar{t}) = -\int_{-\infty}^{\bar{X}} \frac{\partial \bar{P}_{u,1}(\zeta,\bar{Z},\bar{t})}{\partial \bar{Z}} d\zeta, \tag{2.43c}$$

$$\bar{P}_{m,1}(\bar{X},\bar{Z},\bar{t}) = \bar{P}_{u,1}(\bar{X},\bar{Z},\bar{t}), \tag{2.43d}$$

using $\lim_{\bar{Y_m}\to\infty} U_0(\bar{Y_m}) = 1$, $\lim_{\bar{Y_m}\to\infty} U_0'(\bar{Y_m}) = 0$ and $\lim_{\bar{Y_m}\to\infty} R_0(\bar{Y_m}) = 1$. Matching with the undisturbed oncoming boundary layer results in

$$\lim_{\bar{X}\to-\infty} \bar{P}_{m,1} = 0, \lim_{\bar{X}\to-\infty} \bar{U}_{m,1} = 0, \lim_{\bar{X}\to-\infty} \bar{V}_{m,1} = 0, \lim_{\bar{X}\to-\infty} \bar{W}_{m,1} = 0. \tag{2.44}$$

2.3.3. Upper Deck

Inspection analysis performed in section 2.2.3 suggests for the spatial scalings in y-direction and the scaled height of the channel H

$$y_u = \varepsilon^3 \bar{Y}_u, \quad H = \varepsilon^3 \bar{H}, \tag{2.45}$$

and the subsequent formal asymptotic expansions for the flow quantities

$$u_u = 1 + \varepsilon^2 \bar{U}_{u,1}(\bar{X},\bar{Z},\bar{t}) + \mathcal{O}(\varepsilon^3), \tag{2.46a}$$

$$v_u = \varepsilon^4 \bar{V}_{u,1}(\bar{X},\bar{Y}_u,\bar{Z},\bar{t}) + \mathcal{O}(\varepsilon^5), \tag{2.46b}$$

$$w_u = \varepsilon^3 \bar{W}_{u,1}(\bar{X},\bar{Z},\bar{t}) + \mathcal{O}(\varepsilon^4), \tag{2.46c}$$

$$\rho_u = 1 + \varepsilon^2 \bar{\rho}_{u,1}(\bar{X},\bar{Z},\bar{t}) + \mathcal{O}(\varepsilon^3), \tag{2.46d}$$

$$p_u = \varepsilon^2 \bar{P}_{u,1}(\bar{X},\bar{Z},\bar{t}) + \mathcal{O}(\varepsilon^3), \tag{2.46e}$$

$$\theta_u = 1 + \varepsilon^2 \bar{\Theta}_{u,1}(\bar{X},\bar{Z},\bar{t}) + \mathcal{O}(\varepsilon^3), \tag{2.46f}$$

for the condition of transonic flow, introducing the transonic similarity parameter K,

$$(1 - M_0^2) = \varepsilon^2 K. \tag{2.47}$$

Moreover,

$$\mu_u = \mathcal{O}(1). \tag{2.48}$$

Continuity equation. The starting point for the formulation of the upper deck problem is the continuity equation

$$\frac{\partial \rho}{\partial t} + \nabla \cdot (\rho \mathbf{u}) = 0.$$

Insertion of the asymptotic expansions for the upper deck scaling and the appropriate time scaling yields,

$$\mathcal{O}(\varepsilon^2): \quad \frac{\partial \bar{\rho}_{u,1}}{\partial \bar{X}} + \frac{\partial \bar{U}_{u,1}}{\partial \bar{X}} = 0, \tag{2.49a}$$

$$\mathcal{O}(\varepsilon^4): \quad \frac{\partial \bar{\rho}_{u,1}}{\partial \bar{t}} + \frac{\partial}{\partial \bar{X}}\left(\bar{\rho}_{u,2} + \bar{U}_{u,2}\right) + \frac{\partial}{\partial \bar{X}}\left(\bar{\rho}_{u,1}\bar{U}_{u,1}\right) + \frac{\partial \bar{V}_{u,1}}{\partial \bar{Y}_u} + \frac{\partial \bar{W}_{u,1}}{\partial \bar{Z}} = 0. \tag{2.49b}$$

Integration of (2.49a) with respect to $\bar{X}$ then leads to

$$\bar{\rho}_{u,1} + \bar{U}_{u,1} = 0. \tag{2.50}$$

The integration constant entering (2.50) is found to be zero by matching with the undisturbed flow upstream,

$$\lim_{\bar{X}\to-\infty} \bar{U}_{u,1} = 0, \lim_{\bar{X}\to-\infty} \bar{\rho}_{u,1} = 0. \tag{2.51}$$

Momentum equations. The leading order representation of the x-momentum equation is

$$\mathcal{O}(\varepsilon^2): \quad \frac{\partial \bar{U}_{u,1}}{\partial \bar{X}} = -\frac{\partial \bar{P}_{u,1}}{\partial \bar{X}}, \tag{2.52a}$$

$$\mathcal{O}(\varepsilon^4): \quad \frac{\partial \bar{U}_{u,1}}{\partial \bar{t}} + \frac{\partial \bar{U}_{u,2}}{\partial \bar{X}} + \bar{\rho}_{u,1}\frac{\partial \bar{U}_{u,1}}{\partial \bar{X}} + \bar{U}_{u,1}\frac{\partial \bar{U}_{u,1}}{\partial \bar{X}} = -\frac{\partial \bar{P}_{u,2}}{\partial \bar{X}}, \tag{2.52b}$$

which again can be integrated with respect to $\bar{X}$ and yields

$$\bar{U}_{u,1} = -\bar{P}_{u,1}. \tag{2.53}$$

As before the integration constant is found to be zero using the upstream matching conditions (2.51)

$$\lim_{\bar{X}\to-\infty} \bar{P}_{u,1} = 0. \tag{2.54}$$

For the leading order term of the momentum equation in y-direction one again obtains

$$\frac{\partial \bar{P}_{u,1}}{\partial \bar{Y}_u} = 0. \tag{2.55}$$

To leading order the z-momentum equation reduces to

$$\frac{\partial \bar{W}_{u,1}}{\partial \bar{X}} = -\frac{\partial \bar{P}_{u,1}}{\partial \bar{Z}}. \tag{2.56}$$

Energy equation. In the limit $Re \to \infty$ the energy equation

$$\rho \frac{Dh}{Dt} - \frac{Dp}{Dt} = \frac{1}{Re}\tau : \nabla \mathbf{u} - \frac{1}{PrReEc}\nabla \cdot \mathbf{q} \tag{2.57}$$

assumes the inviscid adiabatic form

$$\rho \frac{Dh}{Dt} - \frac{Dp}{Dt} = 0. \tag{2.58}$$

Exploiting the expansion of the enthalpy, cf. A. Kluwick [25],

$$h = (\rho - 1) + \frac{2\Gamma - 3}{2}(\rho - 1)^2 + ... \tag{2.59}$$

yields

$$\mathcal{O}(\varepsilon^2): \quad \frac{\partial \bar{\rho}_{u,1}}{\partial \bar{X}} - \frac{\partial \bar{P}_{u,1}}{\partial \bar{X}} = 0, \tag{2.60a}$$

$$\mathcal{O}(\varepsilon^4): \quad \frac{\partial}{\partial \bar{t}}(\bar{\rho}_{u,1} - \bar{P}_{u,1}) + \bar{U}_{u,1}\frac{\partial \bar{\rho}_{u,1}}{\partial \bar{X}} + \frac{\partial \bar{U}\rho_{u,2}}{\partial \bar{X}} + \frac{\partial}{\partial \bar{X}}\left(\frac{2\Gamma - 3}{2}\bar{\rho}_{u,1}^2\right) = \frac{\partial \bar{P}_{u,2}}{\partial \bar{X}} - K\frac{\partial \bar{P}_{u,1}}{\partial \bar{X}}, \tag{2.60b}$$

where $\Gamma := \frac{1}{\tilde{c}}\frac{\partial(\tilde{\rho}\tilde{c})}{\partial \tilde{\rho}}|_{\tilde{s}}$ is the fundamental derivative of gas dynamics.
Using (2.49), (2.52) and (2.60) the leading order approximation of the solvability condition

$$2\frac{\partial \bar{P}_{u,1}}{\partial \bar{t}} + \frac{\partial}{\partial \bar{X}}J(\bar{P}_{u,1}; K, \Gamma) + \frac{\partial \bar{V}_{u,1}}{\partial \bar{Y}_u} + \frac{\partial \bar{W}_{u,1}}{\partial \bar{Z}} = 0 \tag{2.61}$$

is found, where

$$J(\bar{P}_{u,1}; K, \Gamma) = -K\bar{P}_{u,1} - \Gamma\bar{P}_{u,1}^2 \tag{2.62}$$

is the density of the perturbation mass flux in case of a one-dimensional, isentropic, inviscid and transonic flow of a perfect gas through a nozzle as in A. Kluwick [25].

Integrating equation (2.61) with respect to $\bar{Y}_u$ results in an expression for $\bar{V}_{u,1}$ which has to be matched to the main deck solution. Applying the matching conditions (2.43) finally yields

$$2\frac{\partial \bar{P}_{u,1}}{\partial \bar{t}} + \frac{\partial}{\partial \bar{X}}J(\bar{P}_{u,1}; K, \Gamma) + \frac{1}{\bar{H}}\frac{\partial \bar{A}_1}{\partial \bar{X}} + \frac{\partial \bar{W}_{u,1}}{\partial \bar{Z}} = 0, \tag{2.63}$$

which closes the triple deck problem, since it relates the displacement effect caused by the lower deck to a response of the pressure in the upper deck at leading order. The role of the main deck is just a passive one. The pressure imposed by the outer flow causes a de- or acceleration of the lower deck flow, which results in a displacement of the streamlines in the boundary layer. This displacement effect causes immediately a response of the pressure in the upper deck. Thus equation (2.63) is referred to as interaction law, governing the viscous inviscid interaction of the lower and upper deck flow, respectively.

2.4. Fundamental Lower Deck Problem

Since the role of the main deck is just a passive one, the problem of the viscous inviscid interaction can be fully described by the equations of the lower deck and the interaction law.

Gathering the results of the previous section, the fundamental lower deck problem in non-canonical form is seen to be

$$\frac{\partial \bar{U}_{l,1}}{\partial \bar{X}} + \frac{\partial \bar{V}_{l,1}}{\partial \bar{Y}_l} = 0, \tag{2.64a}$$

$$R_w \left(\bar{U}_{l,1} \frac{\partial \bar{U}_{l,1}}{\partial \bar{X}} + \bar{V}_{l,1} \frac{\partial \bar{U}_{l,1}}{\partial \bar{Y}_l} \right) = - \frac{\partial \bar{P}_{l,1}}{\partial \bar{X}} + \mu_w \frac{\partial^2 \bar{U}_{l,1}}{\partial \bar{Y_l}^2}, \tag{2.64b}$$

$$R_w \left(\bar{U}_{l,1} \frac{\partial \bar{W}_{l,1}}{\partial \bar{X}} + \bar{V}_{l,1} \frac{\partial \bar{W}_{l,1}}{\partial \bar{Y}_l} \right) = - \frac{\partial \bar{P}_{l,1}}{\partial \bar{Z}} + \mu_w \frac{\partial^2 \bar{W}_{l,1}}{\partial \bar{Y_l}^2}, \tag{2.64c}$$

supplemented by the no slip condition at the channel wall

$$\bar{U}_{l,1} = \bar{V}_{l,1} = \bar{W}_{l,1} = 0 \qquad \text{at } \bar{Y}_l = S(\bar{X}, \bar{Z}, \bar{t}), \tag{2.65}$$

the matching condition with the oncoming undisturbed boundary layer flow

$$\lim_{\bar{X} \to -\infty} \bar{P}_{l,1}(\bar{X}, \bar{Z}, \bar{t}) = 0, \tag{2.66a}$$

$$\lim_{\bar{X} \to -\infty} \bar{U}_{l,1}(\bar{X}, \bar{Y}_l, \bar{Z}, \bar{t}) = U_0'(0) \bar{Y}_l, \tag{2.66b}$$

$$\lim_{\bar{X} \to -\infty} \bar{V}_{l,1}(\bar{X}, \bar{Y}_l, \bar{Z}, \bar{t}) = 0, \tag{2.66c}$$

$$\lim_{\bar{X} \to -\infty} \bar{W}_{l,1}(\bar{X}, \bar{Y}_l, \bar{Z}, \bar{t}) = 0 \tag{2.66d}$$

and the matching conditions with the main deck

$$\lim_{\bar{Y}_l\to\infty}\left[\bar{U}_{l,1}(\bar{X},\bar{Y}_l,Z,\bar{t})-U_0'(0)\left(\bar{Y}_l+\bar{A}_1(\bar{X},\bar{Z},\bar{t})\right)\right]=0, \tag{2.67a}$$

$$\lim_{\bar{Y}_l\to\infty}\left[\bar{W}_{l,1}(\bar{X},\bar{Y}_l,Z,\bar{t})+\frac{1}{U_0(0)R_0(0)}\int_{-\infty}^{\bar{X}}\frac{\partial\bar{P}_{l,1}(\zeta,\bar{Z},\bar{t})}{\partial\bar{Z}}d\zeta\right]=0, \tag{2.67b}$$

taking into account, that $\lim_{\bar{Y}_l\to\infty}U_0(0)=U_0'(0)\bar{Y}_l$. The lower deck problem is closed by the interaction law in unsteady form

$$2\frac{\partial\bar{P}_{u,1}}{\partial\bar{t}}+\frac{\partial}{\partial\bar{X}}J(\bar{P}_{u,1};K,\Gamma)+\frac{1}{\bar{H}}\frac{\partial\bar{A}_1}{\partial\bar{X}}+\frac{\partial\bar{W}_{u,1}}{\partial\bar{Z}}=0. \tag{2.68}$$

The interaction law governs the mutual reaction of the lower and upper deck flow. The leading order perturbation of the pressure is generated by the outer flow and the same in all three decks as in the classical boundary layer theory.

The fundamental lower deck problem depends on several parameters, e.g. fluid and geometry properties like μ_w or H, which can be eliminated in all relationships except the interaction law by introducing the affine transformations

$$\bar{X}=|K|^{\frac{3}{2}}(2\Gamma)^{-\frac{3}{2}}R_W^{-\frac{1}{2}}\mu_W^{-1}U_0'(0)^{-2}\cdot X^*, \tag{2.69a}$$

$$\bar{Y}=|K|^{\frac{1}{2}}(2\Gamma)^{-\frac{1}{2}}R_W^{-\frac{1}{2}}U_0'(0)^{-1}\cdot Y^*, \tag{2.69b}$$

$$\bar{Z}=|K|^{\frac{3}{2}}(2\Gamma)^{-\frac{3}{2}}R_W^{-\frac{1}{2}}\mu_W^{-1}U_0'(0)^{-2}\cdot Z^*, \tag{2.69c}$$

$$\bar{t}=|K|^{\frac{1}{2}}2^{-\frac{1}{2}}(\Gamma)^{-\frac{3}{2}}R_W^{-\frac{1}{2}}\mu_W^{-1}U_0'(0)^{-2}\cdot t^*, \tag{2.69d}$$

$$\bar{U}_{l,1}=|K|^{\frac{1}{2}}(2\Gamma)^{-\frac{1}{2}}R_W^{-\frac{1}{2}}\cdot U^*, \tag{2.69e}$$

$$\bar{V}_{l,1}=|K|^{-\frac{1}{2}}(2\Gamma)^{\frac{1}{2}}R_W^{-\frac{1}{2}}\mu_W U_0'(0)\cdot V^*, \tag{2.69f}$$

$$\bar{W}_{l,1}=|K|^{\frac{1}{2}}(2\Gamma)^{-\frac{1}{2}}R_W^{-\frac{1}{2}}\cdot W^*, \tag{2.69g}$$

$$\bar{P}_1=|K|(2\Gamma)^{-1}\cdot P^*, \tag{2.69h}$$

$$\bar{A}_1=|K|^{\frac{1}{2}}(2\Gamma)^{-\frac{1}{2}}R_W^{-\frac{1}{2}}U_0'(0)^{-1}\cdot A^*, \tag{2.69i}$$

$$\bar{S}=|K|^{\frac{1}{2}}(2\Gamma)^{-\frac{1}{2}}R_W^{-\frac{1}{2}}U_0'(0)^{-1}\cdot S^*. \tag{2.69j}$$

Here the subscripts l and u in the pressure terms have been omitted since the pressure perturbation in leading order is constant with respect to y in all three decks. The resulting fundamental lower deck problem except the interaction law is free of any parameters. The remaining parameters in the interaction law can be merged to

$$\Lambda\equiv|K|^{-\frac{3}{2}}(2\Gamma)^{\frac{1}{2}}R_W^{-\frac{1}{2}}U_0'(0)^{-1}\bar{H}^{-1}>0, \tag{2.70a}$$

$$\lambda\equiv2^{-\frac{1}{2}}|K|^{\frac{1}{2}}(\Gamma)^{-\frac{1}{2}}R_W^{-\frac{1}{2}}U_0'(0)^{-1}\bar{H}^{-1}>0, \tag{2.70b}$$

where Λ and λ measure the intensity of the coupling between the lower and the upper deck, respectively. A complete elimination of all parameters, even in the interaction law, is not possible, which is somehow clear since the problem governing parameters must somewhere enter the problem description.

Further, it is convenient to make use of Prandtl's transposition theorem, cf. [41],

$$t = t^*, X = X^*, Y = Y^* - S(X, Z, t), S(X, Z, t) = S^*(X^*, Z^*, t^*), \tag{2.71a}$$

$$U(X, Y, Z, t) = U^*(X^*, Y^*, t^*), \tag{2.71b}$$

$$V(X, Y, Z, t) = V^*(X^*, Y^*, t^*) - U\frac{\partial}{\partial X}S - W\frac{\partial}{\partial Z}S, \tag{2.71c}$$

$$P(X, Z, t) = P^*(X^*, Z^*, t^*), A(X, Z, t) = A^*(X^*, Z^*, t^*) + S(X, Z, t), \tag{2.71d}$$

so that finally the fundamental lower deck problem for the two-dimensional oncoming boundary layer flow in canonical form is given by

$$\frac{\partial U}{\partial X} + \frac{\partial V}{\partial Y} = 0, \tag{2.72a}$$

$$U\frac{\partial U}{\partial X} + V\frac{\partial U}{\partial Y} = -\frac{\partial P}{\partial X} + \frac{\partial^2 U}{\partial Y^2}, \tag{2.72b}$$

$$U\frac{\partial W}{\partial X} + V\frac{\partial W}{\partial Y} = -\frac{\partial P}{\partial Z} + \frac{\partial^2 W}{\partial Y^2} \tag{2.72c}$$

with the no slip condition at the wall

$$U = V = W = 0 \qquad \text{at } Y = 0, \tag{2.73}$$

the matching conditions with the oncoming undisturbed boundary layer

$$\lim_{X\to-\infty} P(X, Z, t) = 0, \tag{2.74a}$$

$$\lim_{X\to-\infty} U(X, Y, Z, t) = Y, \tag{2.74b}$$

$$\lim_{X\to-\infty} V(X, Y, Z, t) = 0, \tag{2.74c}$$

$$\lim_{X\to-\infty} W(X, Y, Z, t) = 0 \tag{2.74d}$$

and the matching condition with the main deck

$$\lim_{Y\to\infty} [U(X, Y, Z, t) - Y] = A(X, Z, t), \tag{2.75a}$$

$$\lim_{Y\to\infty} [W(X, Y, Z, t)] = -\frac{1}{Y}\int_{-\infty}^{X} \frac{\partial P(\zeta, Z, t)}{\partial Z} d\zeta. \tag{2.75b}$$

The lower deck problem is closed by the unsteady form of the interaction law

$$-\frac{\partial P}{\partial t}+\frac{\partial}{\partial X}G(P;K,\Gamma)-\Lambda\frac{\partial}{\partial X}\left(A-S+\frac{1}{\lambda}\int_{-\infty}^{X}\frac{\partial\bar{W}_{u,1}(\zeta,Z,t)}{\partial Z}d\zeta\right)=0, \tag{2.76}$$

with

$$\frac{\partial\bar{W}_{u,1}}{\partial X}=-\frac{|K|}{2\Gamma}\frac{\partial P}{\partial Z}. \tag{2.77}$$

Rewritten just in terms of the pressure, i.e by eliminating the velocity term, yields

$$-\frac{\partial P}{\partial t}+\frac{\partial}{\partial X}G(P;K,\Gamma)=\Lambda\frac{\partial}{\partial X}\left(A-S-\frac{1}{\Lambda\,|K|}\int_{-\infty}^{X}\int_{-\infty}^{\zeta}\frac{\partial^2P(\xi,Z,t)}{\partial Z^2}d\xi d\zeta\right). \tag{2.78}$$

The intensity of the coupling between lower and upper deck is measured by the parameter Λ as defined in equation (2.70). The leading order approximation G, characterizing the negative disturbance of the mass flux density[2] associated with the upper deck flow, is given by

$$G(P;K,\Gamma)=sign(K)P+\frac{1}{2}sign(\Gamma)P^2. \tag{2.79}$$

2.5. Fundamental Lower Deck Problem in Spectral Space

For analytical as well as numerical considerations it is useful to consider an alternative representation of the governing equations, which sometimes allows a more convenient treatment of the problem.

To this end the problem is linearized about the undisturbed oncoming boundary layer flow and mapped into spectral space. This results in a set of algebraic equations instead of the original set of nonlinear partial differential equations, which is advantageous for an analytical treatment.

2.5.1. Governing Equations in Spectral Space

In a first step the X-component of the velocity is split into its perturbed and unperturbed parts

$$U=Y+\hat{U}. \tag{2.80}$$

[2]The fundamental derivative of gas dynamics Γ is strictly positive for a perfect fluid, thus the term $sign(\Gamma)$ in the function G will be omitted in the subsequent sections.

To map the fundamental lower deck problem into spectral space use is made of the double Fourier transform, denoted by a double asterisk

$$\mathcal{F}^2(Q) = Q^{**} = \int_{-\infty}^{\infty}\int_{-\infty}^{\infty} Q(X,Y,Z)e^{-ikX-ilZ}dXdZ, \tag{2.81}$$

where Q denotes an arbitrary field quantity and k, l are the spectral variables corresponding to the physical variables X and Z, respectively. Hence the governing equations in spectral space read as follows

$$ik\hat{U}^{**} + \frac{\partial V^{**}}{\partial Y} = 0, \tag{2.82a}$$

$$ikY\hat{U}^{**} + V^{**} + ikP^{**} - \frac{\partial^2 \hat{U}^{**}}{\partial Y^2} = \mathcal{F}^2\left\{-\hat{U}\frac{\partial \hat{U}}{\partial X} - V\frac{\partial \hat{U}}{\partial Y}\right\}, \tag{2.82b}$$

$$ikYW^{**} + \frac{\partial P^{**}}{\partial Z} - \frac{\partial^2 W^{**}}{\partial Y^2} = \mathcal{F}^2\left\{-\hat{U}\frac{\partial W}{\partial X} - V\frac{\partial W}{\partial Y}\right\}, \tag{2.82c}$$

$$-\frac{\partial P^{**}}{\partial t} + sign(K)\cdot ikP^{**} - ik\Lambda\left(A^{**} - S^{**} - \frac{l^2}{k^2}\frac{1}{\Lambda\,|K|}P^{**}\right) = \mathcal{F}^2\left\{\frac{1}{2}P^2\right\}, \tag{2.82d}$$

where the linearized problem is recovered by neglecting the right-hand-side of (2.82). The boundary conditions become

$$\hat{U}^{**} = V^{**} = W^{**} = 0 \qquad \text{at } Y = 0, \tag{2.83a}$$

$$\lim_{X\to-\infty}(\hat{U}^{**}, V^{**}, W^{**}, P^{**}) = 0, \tag{2.83b}$$

$$\lim_{Y\to\infty}\hat{U}^{**} = A^{**}, \tag{2.83c}$$

$$\lim_{Y\to\infty}W^{**} = -\frac{1}{Y}\mathcal{F}^2\left\{\int_{-\infty}^{X}\frac{\partial P(\zeta,Z,t)}{\partial Z}d\zeta\right\}. \tag{2.83d}$$

2.6. The Flow Structure

Studying the formal asymptotic expansions of the flow quantities and the governing equations of the fundamental lower deck problem the following general statements are derived:

- The most striking feature of the viscous flow in the lower deck is the large size of the crossflow velocity component W in (2.29). This means that the secondary flow (V,W) is basically one dimensional ($W \gg V$) in the lower deck.
- The cross flow velocity profile in the Y-direction must be jetlike, being zero at the wall and an order of magnitude smaller at the edge to the main deck than in the lower deck.
- The crossflow velocity component W neither enters the continuity nor the X-momentum equation, which reflects the weakly three-dimensional behavior. Thus the three-dimensionality enters the problem just in one additional term in the interaction law.
- The crossflow is driven by the pressure gradient in Z-direction induced by the upper deck flow, but there is no response of the upper deck flow due to the crossflow in the lower deck in contrast to the interaction of the upper deck flow with the streamwise flow in the lower deck.
- In the limit $K \to 0$ the weakly three-dimensional problem passes into a pseudo two-dimensional one since the term governing the three-dimensionality becomes negligible small. Hence the horizontal and vertical flow quantities can be determined for each slice in the X-Y plane separately.

3. Solutions of the Linearized Problem

If the height of the surface mounted obstacle is small and therefore the oncoming boundary layer profile only slightly perturbed, the solutions can be described by the linearized fundamental lower deck problem, which is obtained by neglecting the nonlinear terms on the right hand side of equations (2.82). In the steady case this problem can be solved analytically.

3.1. Derivation of the Linearized Solutions in Spectral Space

For an analytical treatment of the fundamental lower deck problem it is valuable to use the spectral representation of the governing equations, as described in section 2.5.1. Thus the linearized steady fundamental lower deck problem in spectral space as stated below is appropriate.

$$ik\hat{U}^{**} + \frac{\partial V^{**}}{\partial Y} = 0, \tag{3.1a}$$

$$ikY\hat{U}^{**} + V^{**} = -ikP^{**} + \frac{\partial^2 \hat{U}^{**}}{\partial Y^2}, \tag{3.1b}$$

$$ikYW^{**} = -\frac{P^{**}}{\partial Z} + \frac{\partial^2 W^{**}}{\partial Y^2}, \tag{3.1c}$$

$$sign(K)P^{**} + \frac{l^2}{k^2}\frac{1}{|K|}P^{**} = \Lambda\left(A^{**} - S^{**}\right), \tag{3.1d}$$

with the subsequent boundary conditions

$$\hat{U}^{**} = V^{**} = W^{**} = 0 \qquad \text{at } Y = 0, \tag{3.2a}$$

$$\lim_{X\to-\infty}(\hat{U}^{**}, V^{**}, W^{**}, P^{**}) = 0, \tag{3.2b}$$

$$\lim_{Y\to\infty}\hat{U}^{**} = A^{**}, \tag{3.2c}$$

$$\lim_{Y\to\infty}W^{**} = -\frac{1}{Y}\mathcal{F}^2\left\{\int_{-\infty}^{X}\frac{\partial P(\zeta, Z, t)}{\partial Z}d\zeta\right\}. \tag{3.2d}$$

The solution for the crossflow velocity component W^{**} is obtained by evaluating the Z-momentum equation (3.1c), which can be rewritten with $r = (ik)^{1/3}Z$ as follows

$$\frac{\partial^2 W^{**}}{\partial r^2} - rW^{**} = \frac{il}{(ik)^{2/3}}P^{**}. \tag{3.3}$$

Using the ansatz $W^{**}(k,l,r) = \varphi(k,l,r) \cdot Ai(r)$ one obtains

$$\varphi'' Ai(r) + 2\varphi' Ai'(r) = \frac{il}{ik^{2/3}}P^{**}, \tag{3.4}$$

where Ai(r) is the Airy function, cf. [1], $()''$ and $()'$ denote the first and second partial derivative with respect to r, respectively. After introducing the ansatz $\psi = \varphi' Ai(r)$ the problem finally reads

$$(\psi Ai(r))' = Ai(r)\frac{il}{(ik)^{2/3}}P^{**}, \tag{3.5}$$

which gives after integrating and considering the boundary conditions (3.2) the final result

$$W^{**}(k,l,r) = Ai(r)\frac{il}{(ik)^{2/3}}P^{**}(k,l)\underbrace{\int_0^r \left\{ Ai^2(\varrho)\int_0^\varrho Ai(s) - \frac{1}{3}ds \right\} d\varrho}_{\mathcal{J}(r)}, \tag{3.6}$$

where $\mathcal{J}(r)$ can also be written in the form $\mathcal{J}(r) = -\frac{2}{\sqrt{3}}\int_0^\infty sin(\frac{1}{3}\zeta^3 + \zeta r - \frac{1}{6}\pi)d\zeta$ as in F.T. Smith [48], [47]. Differentiating the X-momentum equation with respect to Y yields

$$\frac{\partial^2 \hat{\tau}^{**}}{\partial Y^2} - Y\frac{\partial \hat{\tau}^{**}}{\partial Y} = 0, \tag{3.7}$$

which suggests the ansatz $\hat{\tau}^{**}(r) = \frac{\partial \hat{U}^{**}}{\partial r} = B(k,l) \cdot Ai(r)$. Evaluating the X-momentum equation at the wall and introducing this ansatz one obtains

$$B(k,l) \cdot Ai'(0) = (ik)^{1/3}P^{**}. \tag{3.8}$$

Integrating the streamwise shear stress perturbation $\hat{\tau}^{**}$ with respect to Y from 0 to ∞, considering the matching condition (3.2c) gives $\frac{1}{3}B(k,l) = A^{**}$ and hence one obtains

$$(ik)^{1/3}P^{**} = 3Ai'(0)A^{**}. \tag{3.9}$$

Eliminating the displacement function A^{**} by inserting the interaction law (3.1d) yields the final solution for the pressure perturbation

$$(ik)^{1/3}P^{**} = 3Ai'(0)\left[\frac{k^2 + sign(K)\,|K|^{-1}\,l^2}{sign(K)\Lambda k^2}P^{**} + S^{**}\right] \tag{3.10}$$

or rewritten in a more convenient form

$$P^{**} = \frac{sign(K)\Lambda k^2}{-k^2 - sign(K)\left|K\right|^{-1} l^2 + \gamma^{-4/3} sign(K)\Lambda k^2 (ik)^{1/3}} S^{**}, \tag{3.11}$$

where $\gamma = (-3Ai'(0))^{3/4}$. Consequently the streamwise wall shear stress perturbation is found to be

$$\begin{aligned}\hat{\tau}^{**}(k,l,0) = \frac{\partial \hat{U}^{**}}{\partial Y}\mid_{Y=0} &= \frac{\partial \hat{U}^{**}}{\partial r}(ik)^{1/3}\mid_{r=0} = \\ &= \frac{3Ai(0) sign(K)\Lambda (ik)^{2/3}\left(-\frac{l^2}{9Ai^2(0)} + \gamma^{-4/3}(k^2+l^2)\right)}{k^2 + sign(K)\left|K\right|^{-1} l^2 + \gamma^{-4/3} sign(K)\Lambda (k^2+l^2)(ik)^{1/3}} S^{**},\end{aligned} \tag{3.12}$$

and the crossflow wall shear stress perturbation

$$\begin{aligned}\sigma^{**}(k,l,0) = \frac{\partial W^{**}}{\partial Y}\mid_{Y=0} &= \frac{\partial W^{**}}{\partial r}(ik)^{1/3}\mid_{r=0} = \\ &= \frac{sign(K)\Lambda k^2 (ik)^{-1/3} il\mathcal{J}'(0)}{-k^2 - sign(K)\left|K\right|^{-1} l^2 - \gamma^{-4/3} sign(K)\Lambda (k^2+l^2)(ik)^{1/3}} S^{**},\end{aligned} \tag{3.13}$$

where $\mathcal{J}'(0) = -(3Ai(0))^{-1}$. Furthermore, the velocity perturbation in streamwise direction $\hat{U}^{**}$ and the displacement function A^{**} are

$$\hat{U}^{**}(k,l,r) = 3 \cdot A^{**} \int_0^r Ai(s)ds \tag{3.14}$$

and

$$A^{**}(k,l) = P^{**}\left(\frac{sign(K)k^2 + l^2}{\left|K\right|\Lambda k^2}\right) + S^{**}. \tag{3.15}$$

Remark: Equation (3.6) and the shape function $\mathcal{J}(r)$ again reflects the wall jet shaped profile of the crossflow velocity as suggested by the asymptotic expansions in section 2.3.

3.2. Results of the Linearized Problem

Rather than to express the double inversion of the linearized solutions in a real closed form, it is proved more flexible to use a Fast-Fourier-Transform numerical approach, cf. [12]. Thus one is not restricted to particular hump geometries or other simplifications. A quite common smooth surface deformation investigated also in related studies is the cosine-squared hump geometry

$$S(X,Z) = \begin{cases} h_{hump} \cdot cos^2(\frac{\pi}{2}\sqrt{X^2+Z^2}), & \text{for } \sqrt{X^2+Z^2} \leq 1, \\ 0, & \text{otherwise,} \end{cases}$$

which will be used for the following studies and where h_{hump} denotes the height of the surface mounted obstacle.
The problem characterizing parameters Λ and K, the coupling parameter and the transonic similarity parameter, were chosen to be $\Lambda = 1.25$ and $K = \pm 1$ under sub- and supersonic flow conditions, respectively, while the hump height $h_{hump} = 0.1$.

3.2.1. Flow Structure under Subsonic Flow Conditions

The crossflow near the surface can be described by the crossflow wall shear stress σ_w, where constant σ_w-curves in figure 3.1 are denoted by solid lines. First the whole lower deck crossflow upstream the hump moves outwards from the peak line, as shown in figure 3.1. Once the hump is encountered, the crossflow wall shear stress reverses sign, reaching a minimum just beyond the hump's peak, and then becomes positive again immediately downstream the hump. Hence, near the surface the fluid is drawn towards the region just leewards the obstacle, before drifting outwards further downstream. The negative pressure gradient in the Z-direction, where constant $-\frac{\partial P}{\partial Z}$ curves in figure 3.1 are indicated by dashed lines, gives effectively the crossflow velocity at the edge to the main deck. Consequently the crossflow velocity for $Z > 0$ is positive upstream and changes sign near the peak of the hump and thereafter is negative. Thus, at the edge to the main deck, fluid is driven away from the peak line upstream, to enable the fluid to negotiate the obstacle, while downstream the effect is roughly the opposite.
Therefore we can distinguish four regions with a substantial different flow behavior, as indicated on the right side of figure 3.1, which are also existent in the crossflow velocity profiles in figure 3.2.

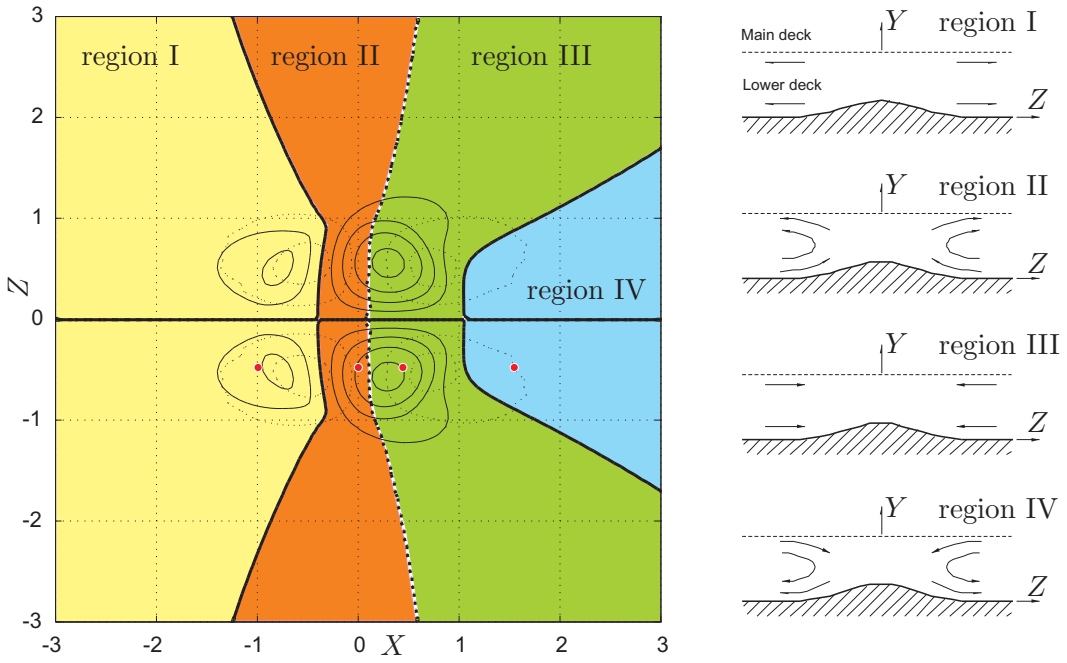

Figure 3.1.: Flow structure under subsonic flow conditions ($\Lambda = 1.25, K = 1$).

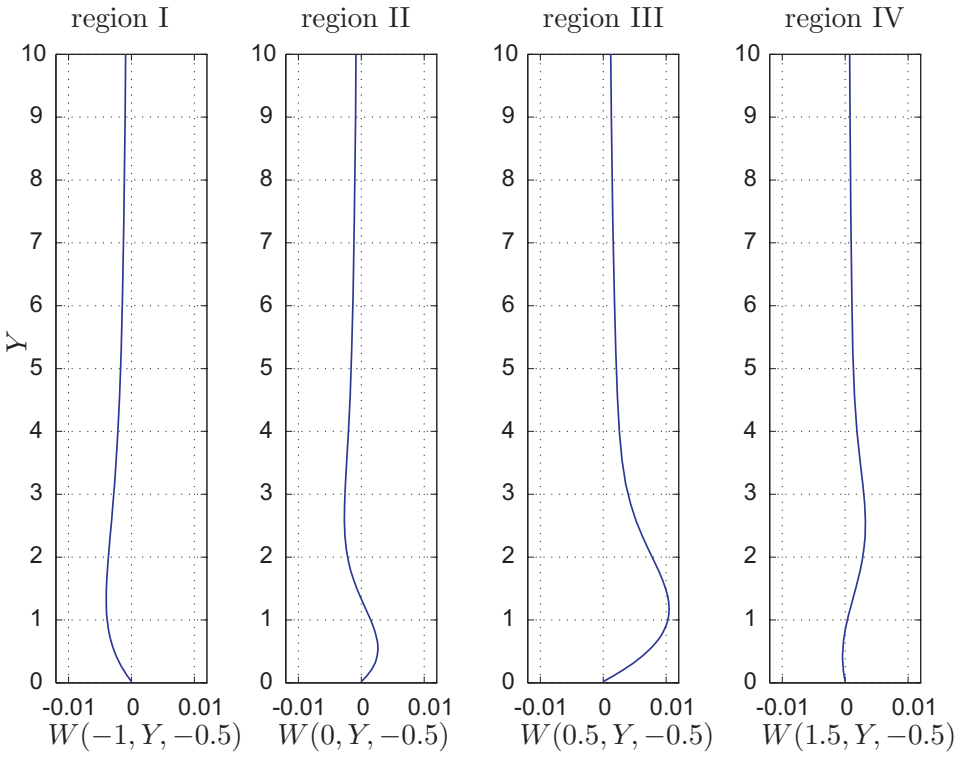

Figure 3.2.: Crossflow velocity profiles W in region I-IV,($\Lambda = 1.25, K = 1, h_{hump} = 0.1$).

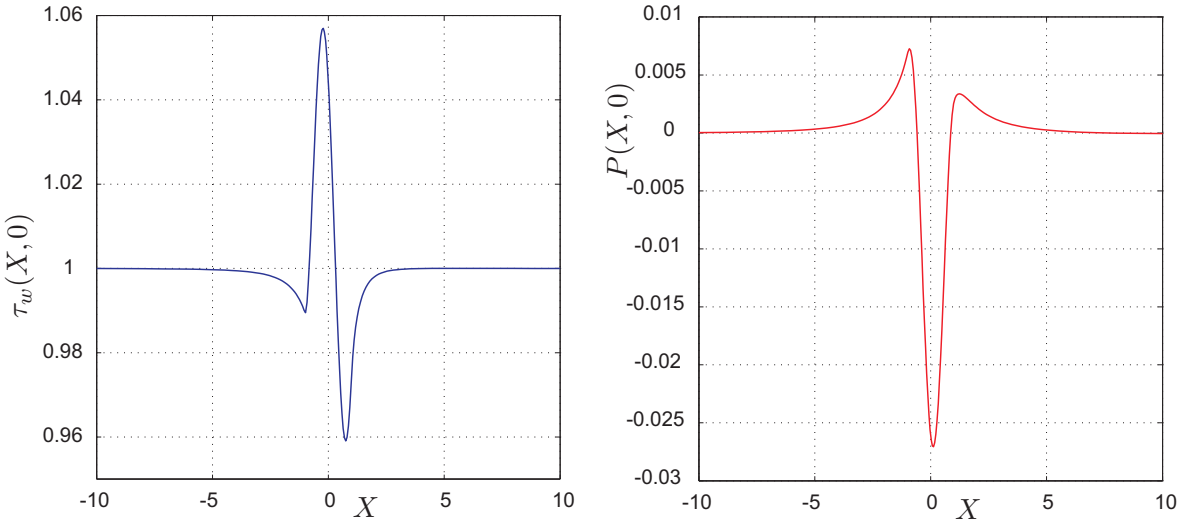

Figure 3.3.: Wall shear stress τ_w and pressure perturbation P along the centerline of the hump (Z=0) for $\Lambda = 1.25$, $K = 1$ and and $h_{hump} = 0.1$.

The simple source-like trend upstream in region I is followed by some major adjustment of the crossflow velocity close to the surface near the hump in region II. First, fluid near the surface starts to be drawn inwards near the peak of the hump, so that a vortex motion appears. Then, over the back of the hump, the entire lower deck flow acquires a sink-like form, in order that the fluid may encircle the obstacle. Finally, beyond the hump, the displacement forces the surface fluid eventually to be expelled, while the fluid above the lower deck is drawn in, and so another vortex motion is set up. This vortex rotates in the opposite sense to the vortex near the rear of the hump. The vortex lines of this vortex in region II must be stretched as they pass over and around the obstacle. The vorticity is concentrated near the front of the hump, and a streamwise component of the vorticity is induced as for the horseshoe shaped vortex, cf. R. Sedney [45], due to the vortex transport equation

$$\frac{D\boldsymbol{\omega}}{Dt} = (\boldsymbol{\omega} \cdot \nabla)\mathbf{u} + \nu\nabla^2\boldsymbol{\omega},$$

where $\boldsymbol{\omega} = \mathrm{rot}(\mathbf{u})$ is the vorticity.

In streamwise direction the flow is first slightly decelerated upstream the hump, accelerates with encountering the hump, reaching a maximum a the peak and is again highly decelerated at the leeward side of the hump. Finally to attain an undisturbed state downstream again the flow is slightly accelerated, as evident in the pressure perturbation along the center line of the hump as shown in figure 3.3.

Consequently the wall shear stress τ_w first rises with the acceleration of the flow and

drops with the deceleration at the lee-side of the hump. If the surface deformation is large enough a local supersonic region in the upper deck flow due to the acceleration of the flow followed by a region of separated flow caused by the following deceleration is expected.

3.2.2. Flow Structure under Supersonic Flow Conditions

Under supersonic flow conditions similar results as under subsonic flow conditions are obtained.

The fluid near the surface upstream the obstacle is moved outwards from the peak line again, once the hump is encountered, the crossflow wall shear stress σ_w reverses sign and then becomes positive for $Z > 0$ immediately downstream the hump. Therefore, near the surface at the lee-side of the obstacle the fluid is drawn towards the peak line, before drifting outwards further downstream. Near the peak of the hump the cross flow velocity at the edge of the main deck changes sign as under subsonic flow conditions and becomes negative for $Z > 0$ on the leeward side of the hump. Thus, at the edge to the main deck, fluid is again driven away from the peak line upstream, while downstream this motion is reversed.

Therefore we can distinguish again the four regions with a substantial different crossflow behavior as under subsonic flow conditions, see figure 3.4, which are also existent in the crossflow profiles shown in figure 3.5.

In streamwise direction the flow is again slightly decelerated upstream the hump and accelerates with encountering the hump followed by a deceleration at the leeward side of the hump. To attain an undisturbed state downstream again the flow is slightly accelerated finally, as evident in the pressure perturbation along the center line of the hump in figure 3.6.

Consequently the wall shear stress τ_w de- and increases with the de- and acceleration of the flow, respectively. Again one might expect a subsonic region in the upper deck flow in front of the hump caused by the deceleration if the deformation of the surface is large enough. Also separation might be caused at the lee-side of the hump for sufficiently large hump heights by the deceleration of the flow.

Moreover, the perturbation of the undisturbed flow quantities under supersonic flow conditions is much larger than under subsonic flow conditions, obvious by comparing figure 3.3 and figure 3.6.

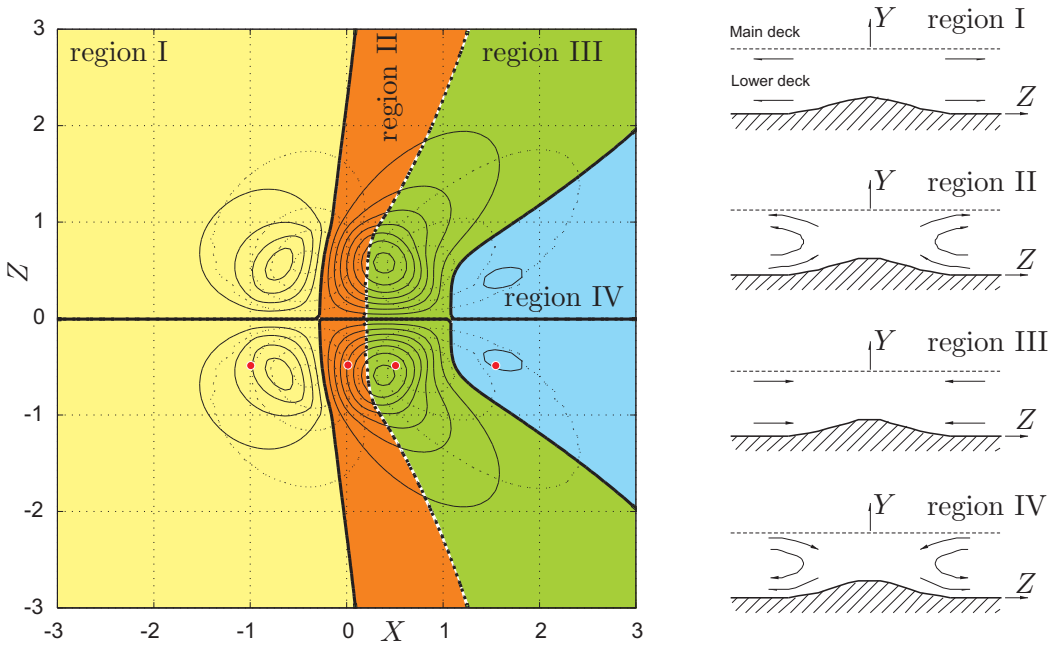

Figure 3.4.: Flow structure under supersonic flow conditions ($\Lambda = 1.25, K = -1$).

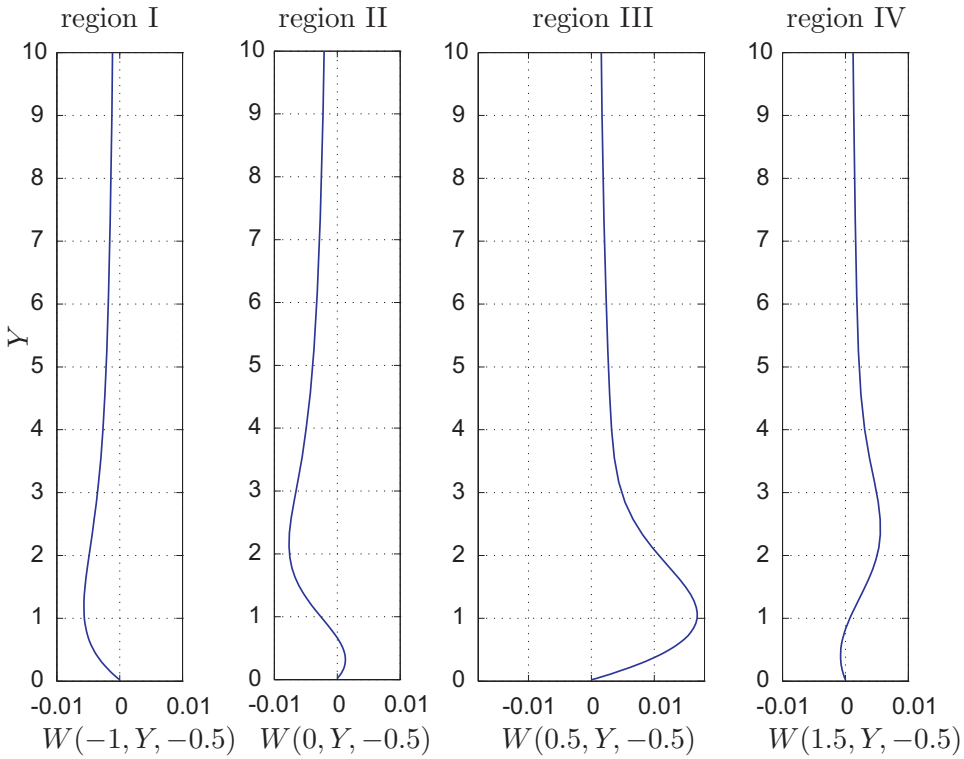

Figure 3.5.: Crossflow velocity profiles W in region I-IV,($\Lambda = 1.25, K = -1, h_{hump} = 0.1$).

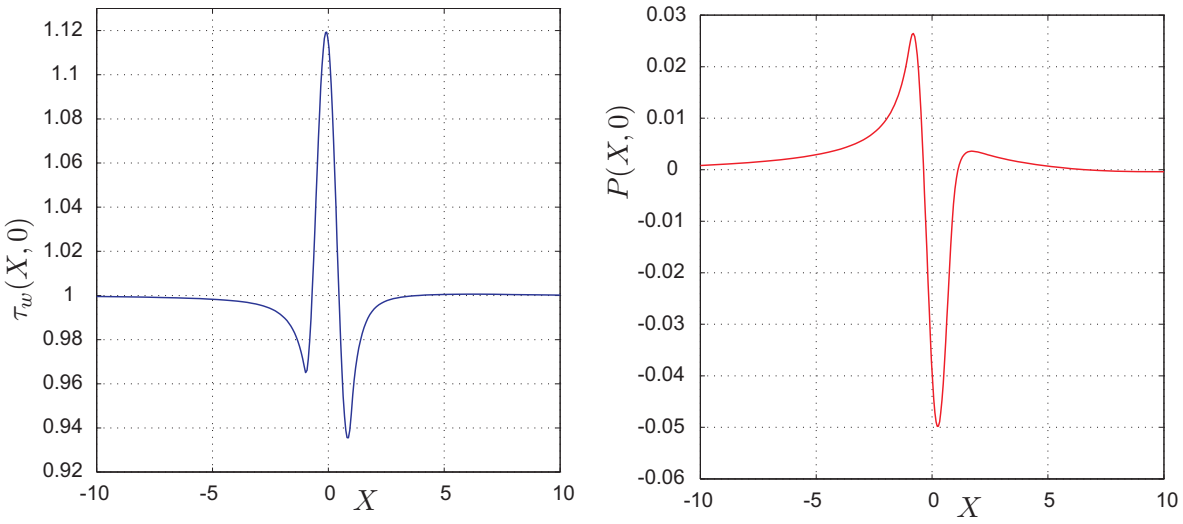

Figure 3.6.: Wall shear stress τ_w and pressure perturbation P along the centerline of the hump (Z=0) for $\Lambda = 1.25$, $K = -1$ and $h_{hump} = 0.1$.

3.3. Asymptotic Behavior far Downstream ($X \gg 1$)

An approximation of the solution of the flow quantities far downstream can be attained by truncating the spectral representation and considering just the main contributions. Thus asymptotic solutions of the fundamental lower deck problem are obtainable in a closed analytical form. Due to the decaying character of the flow quantities far downstream these asymptotic solutions are expected to be also a quite good approximation of the solutions of the nonlinear problem far downstream.
The main contributions to the solutions far downstream ($X \gg 1$) are found for the spectral variable $k \ll 1$, or more precisely for $k = \mathcal{O}(\frac{1}{X})$. By neglecting terms of $o(k)$ in the spectral representation of the solutions and evaluating this truncated representation via Inverse Fourier Transform the asymptotic behavior of the flow quantities is obtained.

3.3.1. Wall Shear Stress

The dominant contribution to the wall shear stress perturbation $\hat{\tau}_w$ near the X-axis, in fact when $Z = \mathcal{O}(1)$, comes from small values of k, with l finite or more precisely $k = o\left(\frac{l}{\sqrt{|K|}}\right)$, when

$$\hat{\tau}_w^{**}(k \ll 1, l) \sim 3Ai(0)\,|K|\,\Lambda(ik)^{2/3}\left[\gamma^{-4/3} - \frac{1}{9Ai^2(0)}\right] S^{**}(0,l). \tag{3.16}$$

This gives

$$\hat{\tau}_w(X \to \infty, Z) \sim \frac{3\sqrt{3}Ai(0)\Gamma(\frac{5}{3})\,|K|\,\Lambda}{4\pi^2}\left[\gamma^{-4/3} - \frac{1}{9Ai^2(0)}\right] X^{-5/3}\int_{-\infty}^{\infty} S(X,Z)dX, \tag{3.17}$$

which is valid in a region $X \gg 1$ and $Z \ll \frac{X}{\sqrt{|K|}}$. Due to the Integral in (3.17) the streamwise wall shear stress perturbation far downstream is confined to a region with a lateral extension of the width of the hump and is zero outside this region matching the condition of undisturbed flow quantities for $Z \to \infty$, which is also confirmed by numerical results. But a 'corridor' phenomenon in the boundary layer displacement and the streamwise wall shear stress as observed for three-dimensional subsonic flows by F.T. Smith, R.I. Sykes and P.W.M. Brighton, c.f. [49], is not existent.
Similarly the main contribution for the crossflow wall shear stress σ_w again comes from small values of k and l finite, when

$$\sigma_w^{**}(k \ll 1, l) \sim \mathcal{J}'(0)\,|K|\,\Lambda k^2(ik)^{-1/3}\frac{1}{il}S^{**}(0,l), \tag{3.18}$$

yielding

$$\sigma_w(X \to \infty, Z) \sim \frac{5\mathcal{J}'(0)\Gamma(\frac{5}{3})\,|K|\,\Lambda}{4\pi^2\sqrt{3}} \cdot X^{-8/3} \cdot \Xi(Z) \tag{3.19}$$

with

$$\Xi(Z) = \int_{-\infty}^{Z}\int_{-\infty}^{\infty} S(X,\zeta)dXd\zeta - \int_{-\infty}^{0}\int_{-\infty}^{\infty} S(X,\zeta)dXd\zeta, \tag{3.20}$$

which is again valid in a region $X \gg 1$ and $Z \ll \frac{X}{\sqrt{|K|}}$ and referred as 'inner' asymptotic solution. For values of $Z \gg \frac{X}{\sqrt{|K|}}$ one can find an 'outer' asymptotic solution satisfying vanishing perturbations for $Z \to \infty$, which can be matched with the 'inner' solution to an uniformly valid solution in Z-direction. But since for $X \gg 1$ also the region of the 'inner' solution is valid for $Z \gg 1$, the determination of the 'outer' solution is omitted. The shape function $\Xi(Z)$ is obviously independent of X, but in contrast to the streamwise wall shear stress the crossflow wall shear stress distribution spreads with increasing values of X due to the matching of the 'inner' and 'outer' solution. This is also indicated by the wedge shape of region IV as sketched in figure 3.1 and figure 3.4
Moreover, both results, the streamwise and crossflow wall shear stress perturbation, are independent of $sign(K)$ and therefore stay the same under subsonic as well as under supersonic flow conditions.

3.3.2. Pressure Perturbation

For the asymptotic representation of the pressure perturbation we have now to distinguish between sub- and supersonic flow conditions, respectively. In contrast to the case of subsonic flow conditions there is a singularity at $k = l$ caused by neglecting terms of $o(k)$ in the case of supersonic flow conditions, which is regularized by the full spectral representation and therefore a closed analytical representation is not obtainable. But numerical results gives the hint that the pressure perturbation under supersonic flow conditions is more less similar to the solution under subsonic flow conditions just with a reversed sign corresponding to the factor $sign(K)$ in equation (3.11).

Thus, the dominant contribution to the pressure perturbation under subsonic flow conditions far downstream comes again from small values of the spectral variables k and l, or more precisely $k = \mathcal{O}\left(\frac{l}{\sqrt{|K|}}\right)$, when

$$P^{**}(k \ll 1, l \ll 1) \sim -\frac{\Lambda k^2}{k^2 + |K|^{-1} l^2} S^{**}(0,0). \tag{3.21}$$

This gives

$$P(X \to \infty, Z) \sim \frac{\Lambda\sqrt{|K|}}{4\pi^2} \int_{-\infty}^{\infty}\int_{-\infty}^{\infty} S(X,Z)dXdZ \cdot X^{-2}\frac{1-\xi^2}{(1+\xi^2)^2} \tag{3.22}$$

with $\xi = \sqrt{|K|}\frac{Z}{X}$, which is valid in a region $X^2 + |K|Z^2 \gg 1$.

The pressure distribution also spreads with increasing values of X, like the crossflow wall shear stress, which somehow meets our expectations since the crossflow is just driven by the pressure gradient in Z-direction and thus a spreading crossflow requires a spreading pressure distribution.

4. Nonlinear Effects

In the present chapter the effect of boundary layer separation at the lee side of a surface mounted hump and the influence of variation of the transonic similarity parameter K on the flow field will be discussed.

So far only the linearized solutions were obtained, valid for vanishingly small humps. If the hump height becomes an $\mathcal{O}(1)$ quantity the full nonlinear problem has to be solved and requires a numerical treatment of the fundamental lower deck equations.
To this end a pseudo spectral method, cf. [10], [15], [19], [3], is used, which requires much less memory resources than standard numerical techniques (i.e. finite-difference schemes) in particular for three-dimensional problems, for which finite-difference methods have not proven successful. A major advantage of spectral methods is to capture regions of reversed flow (i.e. boundary layer separation) without any additional approximations (e.g. FLARE-approximation for finite-difference methods). The physical problem can be solved very effectively and allows the usage of standard numerical algorithms (e.g. FFT-algorithm) by mapping the unbounded physical domain $X \times Z \in [-\infty, \infty] \times [-\infty, \infty]$ onto a bounded domain $x_n \times z_n \in [0, \pi] \times [0, \pi]$, cf. [5], [9]. A detailed discussion of the used pseudo spectral method is given in appendix B.

4.1. Boundary layer separation

As already shown by the linearized results the fluid at the leeward side of the hump is decelerated and thus the wall shear stress τ_w decreases, cf. figure 4.1. If the height of the surface mounted hump is large enough the wall shear stress becomes negative locally. Thus a region where the streamwise velocity component reverses sign, i.e. a region of reversed flow, occurs. The velocity profiles of the streamwise velocity component U in the region of reversed flow are shown in figure 4.3.

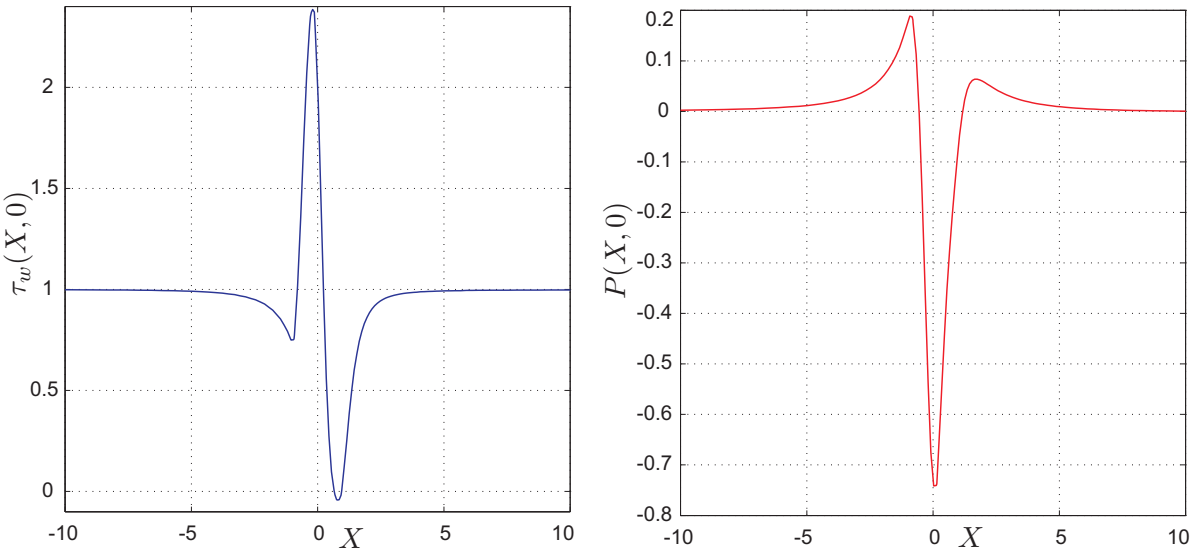

Figure 4.1.: Wall shear stress τ_w and pressure perturbation P along the centerline of the hump (Z=0) for $\Lambda = 1.25$, $K = 1$ and $h_{hump} = 2.25$.

Therefore the boundary layer starts to separate from the wall exactly where τ_w becomes negative and reattaches further downstream where the wall shear stress changes again to positive values, as shown in figure 4.2.
The fluid inside the region of reversed flow forms a separation bubble. Since the cross flow velocity component W is two orders of magnitude smaller than the streamwise velocity component U the wall streamlines are almost parallel to the X-axis and a closed separation bubble without fluid exchange with the outer flow might be expected.

Even though the crossflow velocity component is much smaller than the streamwise velocity component it is not negligible since it plays a dominant role in regions of vanishing shear stress τ and velocity V. Along these lines the fluid is drawn inwards to the centerline $Z = 0$. Following Oswatitsch, [39], such a separation point at the centerline is called point of weak convergence or separation node, when $\frac{\sigma_{w,X}}{\tau_{w,X}} < 1$. The structure of the streamlines in the vicinity of this point is sketched in figure 4.4.

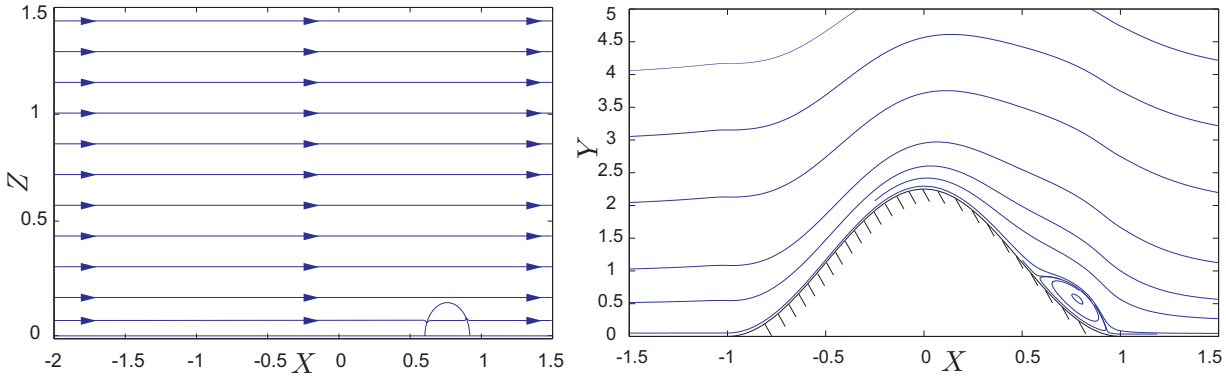

Figure 4.2.: Wall streamlines in the vicinity of the hump (left hand side) and streamlines in a cross section $Z = 0$ with a separation bubble at the lee side of the hump (right hand side), ($h_{hump} = 2.25, \Lambda = 1.25, K = 1$).

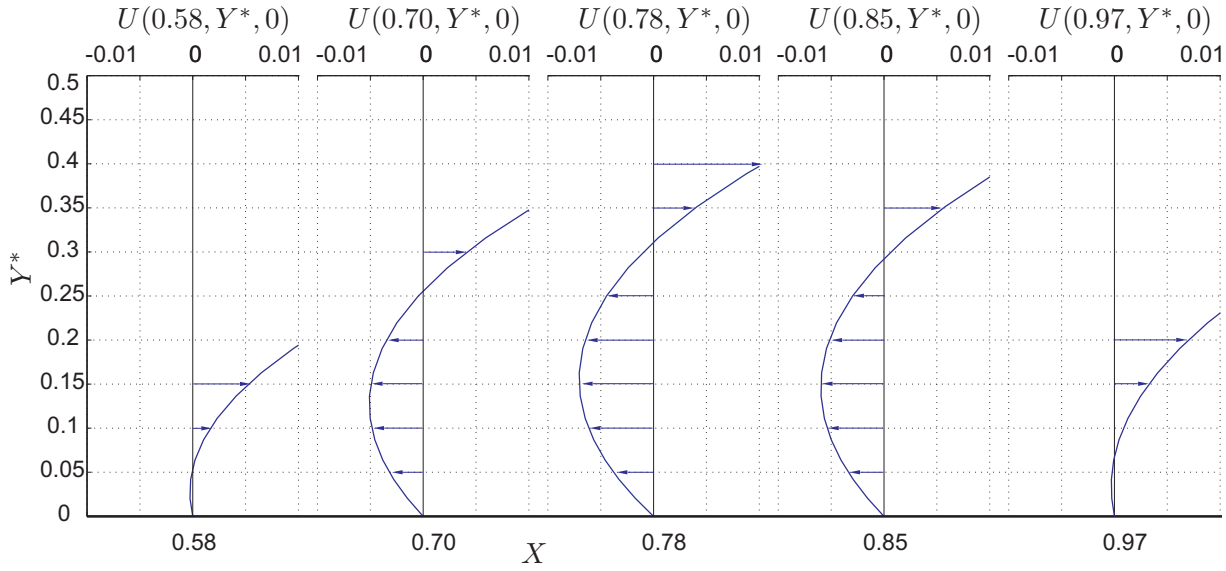

Figure 4.3.: Streamwise velocity profiles $U(X, Y, 0)$ in the separation bubble at the centerline $Z = 0$.

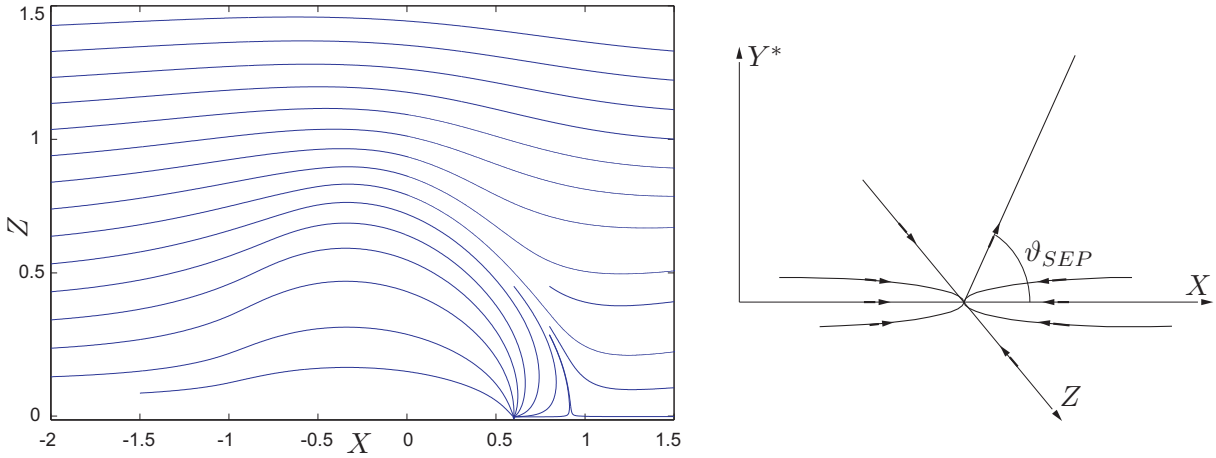

Figure 4.4.: Wall streamlines with an appropriate scaled crossflow velocity component in the vicinity of the hump and the point of weak convergence at $X = 0.57, Z = 0$ (left hand side) and the flow structure close to the point of weak convergence with the angle of the separation streamline ϑ_{SEP} (right hand side).

Further insight into the flow structure close to the separation node and the point of reattachment is gained by studying the wall streamlines with an appropriate scaled crossflow velocity component, such that this field quantity becomes of $\mathcal{O}(U)$. The singular points at separation and reattachment are of special interest. These occur at the intersection of the zero contours of the streamwise and cross flow wall shear stresses. For the cosine-squared hump geometry there are only two such singularities both on the centerline $Z = 0$.

These streamlines, as shown in figure 4.4, are not to scale, but illustrate nicely the type of the singularity. Accordingly a separation node at $X = 0.567$ and a attachment saddle point at $X = 0.975$ is found. The number of nodal points must exceed the number of saddle points exactly by two for a finite closed surface geometry as shown by Lighthill et al. [18]. Since the basic flow can be interpreted as a result of a source and a sink like nodal point at $X \to \mp\infty$, respectively, the number of singularities above is seen to satisfy this condition.
Thus each fluid particle in the separation bubble is seen to be transported slowly to the sink like separation node. There the fluid starts to separate from the wall and moves further on the surface of the bubble to the point of reattachment and back again to the separation node on a closed streamline as shown on the right hand side in figure 4.2.

Due to this mechanism fluid is continuously brought into the bubble and concentrated at the center. The crossflow velocity component enters the continuity equation in the higher order approximations, which effectively yields weakly diverging helical streamlines for $\frac{\partial W}{\partial Z} < 0$. Since the crossflow velocity and thus the mass flux into the bubble is small these weakly opened streamlines are sufficient to generate a small outflow and satisfy the continuity. Thus one finds a small open separation bubble with a mass flux into the bubble from both sides and an outflow at the center.

This separation bubble topology is similar to the results found by Kluwick and Hackmüller, [27], studying the wall streamline pattern on a swept wing. In contrast to these results, where an open separation bubble with a mass flux into the bubble from the left and an outflow at the right side occurs, the outflow mass flux in our case takes place on the centerline.
Similar open separation bubbles are also observed in geophysical flows over sandy three-dimensional elevations, see [20]. There the fluid is also concentrated at the centerline, but the streamlines near the center are of a focusing type, and the release of fluid is achieved through a helical flow out toward the Z-direction.

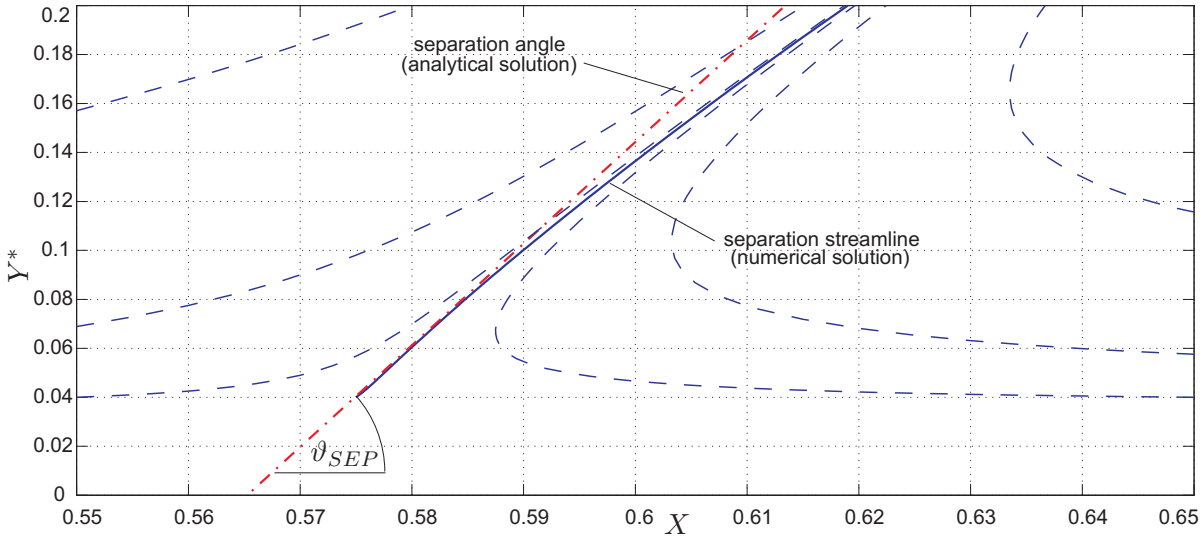

Figure 4.5.: Streamlines in a cross section through the centerline Z=0 in the vicinity of the separation point (dashed lines) with the separation streamline (solid line) and separation angle ϑ_{SEP}.

To validate the numerical results in vicinity of the separation bubble the separation streamline close to the wall, cf. [39],

$$y_{SEP} = X \cdot tan(\vartheta_{SEP}) \tag{4.1}$$

with the separation angle

$$tan(\vartheta_{SEP}) = -\frac{3\tau_{w,X}}{P_X} \tag{4.2}$$

is determined, where the subscript X denotes the derivative with respect to X. Equation (4.2) was originally obtained for planar flows but is also valid in the weakly three-dimensional case since the crossflow quantities are small. The streamlines in vicinity of the separation point are indicated by dashed lines and the separation streamline by a solid line, respectively. Due to the discretization and the no-slip condition at the wall reliable results of the streamline integration algorithm are obtained for $Y^* \geq 0.04$. Therefore the numerically found separation streamline obviously "starts" at $Y^* = 0.04$ and not as physically exact at the wall. Evaluating equation (4.1) and (4.2) yields the separation angle as well as a linear approximation of the separation streamline (dashed dotted line) close to the wall. As shown in figure 4.5 the tangent of the numerically found separation streamline at the wall coincides very well with the analytically obtained approximation of the separation streamline and the corresponding separation angle.

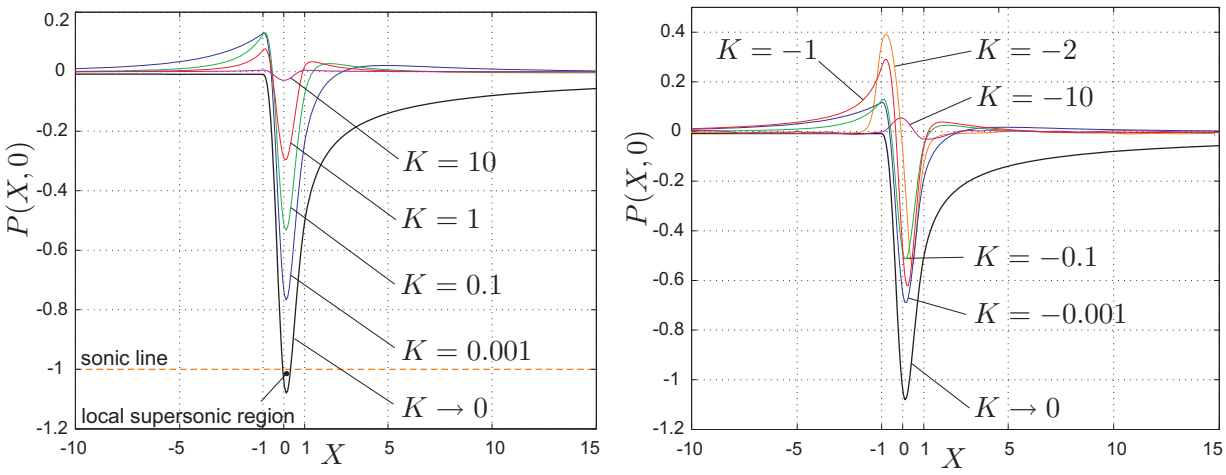

Figure 4.6.: Pressure perturbation P for various values of K under subsonic flow conditions (left hand side) and under supersonic flow conditions (right hand side), $(h_{hump} = 1.0, \Lambda = 1.25|K|^{-3/2})$.

4.2. Effects due to the transonic similarity parameter K

To study the influence of the transonic similarity parameter K on the flow behavior the flow is perturbed by a surface mounted cosine-squared hump of constant height, while the parameter K is varied. To avoid other nonlinear effects, such as boundary layer separation, the hump height is taken to be $h_{hump} = 1$. Since K is proportional to the difference between the Mach number of the undisturbed flow M_0 and its critical value $M = 1$ small values of K describe a regime close to sonic conditions, whereas in the limit $K \to \pm\infty$ purely sub- and supersonic conditions are obtained.

A first insight is gained by analyzing the limiting cases $K \to 0$ and $|K| \gg 1$, respectively. For $K \to 0$ the weakly three-dimensional problem reduces to a pseudo two-dimensional one since the term governing the three-dimensionality becomes negligible. Thus the horizontal and vertical flow quantities can be determined for each slice in the X-Y plane separately and the formulation of the linearized problem yields the solution

$$P_{K\to 0} = \frac{\gamma^{4/3}}{4\pi^2} \frac{\partial^{2/3}}{\partial X^{2/3}} \int_{-\infty}^{X} S(\zeta, Z) d\zeta.$$

As suggested by the above results the solution becomes independent of the coupling parameter Λ and obviously also of $sign(K)$. Moreover, the pressure perturbation $P(X, Z)$ vanishes for $S(X < -1, Z) = 0$ and exhibits a minimum close to the maximum of $S(X, Z)$.

In the other limiting case, $|K| \gg 1$, the interaction between the lower and the upper deck disappears since the coupling parameter $\Lambda \sim |K|^{-3/2} \to 0$. Thus the upper deck does not respond to changes in the lower deck and hence just the surface mounted hump is "seen" in the upper deck. This is seen also by inspection of the linearized solution of the pressure perturbation, which yields

$$P_{|K|\to\infty} = -sign(K)\Lambda S(X, Z).$$

Thus the pressure perturbation reflects just the hump geometry scaled with the coupling parameter Λ, while the sign of the perturbation only depends on the flow conditions; i.e. whether sub- or supersonic flow conditions are present.

The numerical results for various values of $|K|$, as shown in figure 4.6 for the pressure perturbation, confirm the analytical results of the linearized problem for the limiting cases, even for $K \to 0$ where $|P| \sim 1$ and thus the linearization is formally not valid anymore. In general, an increasing pressure perturbation is found for decreasing absolute values of K. But one has to be careful by interpreting these results since all lower deck quantities as well as the length scales and the hump geometry are suitable scaled and the scaling depends on $|K|$ also. Thus for different values of the transonic similarity parameter the physical hump height differs even if the height is constant in the lower deck representation.
Under subsonic flow conditions, if $|K|$ is small enough, i.e. if the flow is close enough to the point of transition $P = 1$, the flow exhibits a local supersonic region in the upper deck. This local supersonic flow is shocked back to subsonic flow conditions via a pseudo shock representing the regularization of the shock discontinuity predicted by the theory of inviscid flows. As to be expected, therefore, the shock thickness tends to zero in the limit $\Lambda \to 0$ where the effect of boundary layer displacement becomes arbitrarily small. There is no corresponding local subsonic region in the inviscid core region, i.e. a pressure perturbation greater than P=1, under supersonic flow conditions for $h_{hump} = 1.0$. By increasing the hump height such a local subsonic region could be found. In the two-dimensional case a regularized shock profile, where the flow is continuously decelerated from super- to subsonic flow conditions, occurs for sufficiently large humps. Weakly three-dimensional shock profiles are the topic of later discussions.

Another remarkable effect of the type of flows considered here is the phenomenon of upstream influence, i.e. perturbations of the flow field arise upstream the surface mounted hump. This effect is common in the two-dimensional case under supersonic flow conditions as well, but in contrast to the three-dimensional results there is strictly no such effect under subsonic flow conditions, which was shown by Kluwick and Meyer [31].
A detailed discussion of the phenomenon of upstream influence under subsonic flow conditions is given in the next chapter.

5. Upstream Influence, Free Interaction and Eigensolutions

One interesting property of laminar boundary layers is their capability, specially under supersonic flow conditions, of spontaneously undergoing a radical change without any locally operating external agent. This phenomenon is among others responsible for the flow having a bifurcated, or lambda, shock structure and cause separation upstream of the point of incidence of the main shock as shown in detail by Chapman et al. [11]. This effect contradicts the previously accepted mathematical account that both supersonic inviscid flow and conventional forward-moving compressible boundary layer flow do not allow upstream propagation of disturbances. A first mathematical explanation for supersonic flows without separation was given by Lighthill [33], while the resolution to this apparent paradox was delevoped by Stewartson and Williams [51], [52] to give the first rational account of upstream influence. The structure of three-dimensional free-interactions in external flows was studied by Smith et al. [16] and freely interacting transonic boundary layers by Bodonyi and Kluwick [4].
For channel flows similar effects are observed. If the height of the channel becomes sufficiently small, such that there is no variation of the pressure across the channel $P = P(X, Z)$, no upstream influence occurs under subsonic flow conditions for a two-dimensional channel indentation as shown by Kluwick and Meyer [31]. Only under supersonic flow conditions an upstream propagation of disturbances in narrow two-dimensional channels is observed. Furthermore, beside the trivial solution

$$P \equiv 0, \quad A \equiv 0, \quad U \equiv Y,$$

two eigensolutions are found, where the compressive eigensolution corresponds to the internal structure of a weak normal shock in a channel. In contrast to these results upstream propagating disturbances are found under subsonic as well as under supersonic flow conditions in the weakly three-dimensional case.

This effect is investigated in the subsequent sections by studying the linearized problem in the two-dimensional case and afterwards by extending the formulation to the weakly three-dimensional one.

5.1. Upstream Propagating Perturbations

5.1.1. Upstream Influence in the Two-Dimensional Case

To show the occurrence of the effect of upstream influence the linearized pressure perturbation in spectral space

$$P^{**} = \underbrace{\frac{sign(K)\Lambda k^2}{-k^2 - sign(K)\,|K|^{-1}\,l^2 + \gamma^{-4/3} sign(K)\Lambda k^2 (ik)^{1/3}}}_{\Omega(k,l)} S^{**},$$

as stated in equation (3.11) is studied.
Inversion of the Fourier transform and Cauchy's residual theorem yields an upstream effect if there are poles placed in the lower complex plane $(-i)$. By shifting the hump geometry such that $S(X,Z) \equiv 0$ for $X < 0$ we ensure that there are no negative complex poles due to the geometry and it is sufficient just to study the poles of the transfer function Ω.
Thus the poles of $\Omega(k,0)$ in the two-dimensional case are found by evaluating the denominator function $f(s)$

$$f(s) = s^6 + sign(K)\Lambda\gamma^{-4/3}s^7 = 0, \tag{5.1}$$

where $s^3 = ik$.
Hence the position of the poles are given by

$$s_{1\ldots6} = 0, \qquad s_7 = -sign(K)\gamma^{4/3}\Lambda^{-1} \tag{5.2}$$

and respectively for the original problem

$$k_{1\ldots6} = 0, \qquad k_7 = -sign(K)\gamma^4\Lambda^{-3}i, \tag{5.3}$$

where the term γ is associated with the two-dimensional eigenvalue found by Lighthill [33] and Stewartson and Williams [51].

Since $\gamma^4\Lambda^{-3} > 0$ the location of the poles only depend on $sign(K)$. Therefore we recover the well known observations for a two-dimensional channel wall deformation. An

upstream influence occurs under supersonic flow conditions ($K < 0$) while perturbations cannot make themselves felt upstream of the wall deformation under subsonic flow conditions ($K > 0$).

5.1.2. Upstream Influence in the Weakly Three-Dimensional Case

In the weakly three-dimensional case a generalized denominator function is given by

$$f(s,l) = s^6 + sign(K)\Lambda\gamma^{-4/3}(s)^7 - sign(K)\frac{1}{|K|}l^2 = 0, \tag{5.4}$$

which differs from equation (5.1) just by $-sign(K)\frac{1}{|K|}l^2$. This term can be interpreted as a shift of $f(s, l = 0)$ with respect to the spectral variable l. Since we are not interested in the exact location and numbers of poles but in the existence of at least one pole in the lower complex plane it is sufficient to perform a qualitative analysis. Thus the denominator function is studied graphically as shown in figure 5.1.

There the poles in the lower complex plane of the transfer function correspond to zeros in the region $s > 0$ (yellow shaded region) and indicated by red circles. The denominator function $f(s, l = 0)$ is denoted by blue and red solid lines under supersonic and subsonic flow conditions, respectively, while the generalized denominator function $f(s, l)$ is found by shifting the former one by an amount of $l^2|K|^{-1}$ upwards for $K < 0$ (supersonic conditions, red dashed line) and downwards for $K > 0$ (subsonic conditions, blue dashed line).

As shown in figure 5.1 the shift of the denominator functions results in a slight displacement of the position of the poles $p_n(l = 0)$ with respect to l under supersonic flow conditions. Thus the weakly three-dimensional upstream behavior for $K < 0$ is expected to closely resemble the two-dimensional behavior.
Under subsonic flow conditions, however, this shift cause a new pole to appear in the lower complex plane. Therefore an upstream influence also for $K > 0$ is observed even if the channel is sufficiently slender, such that the pressure perturbation is constant across the channel.

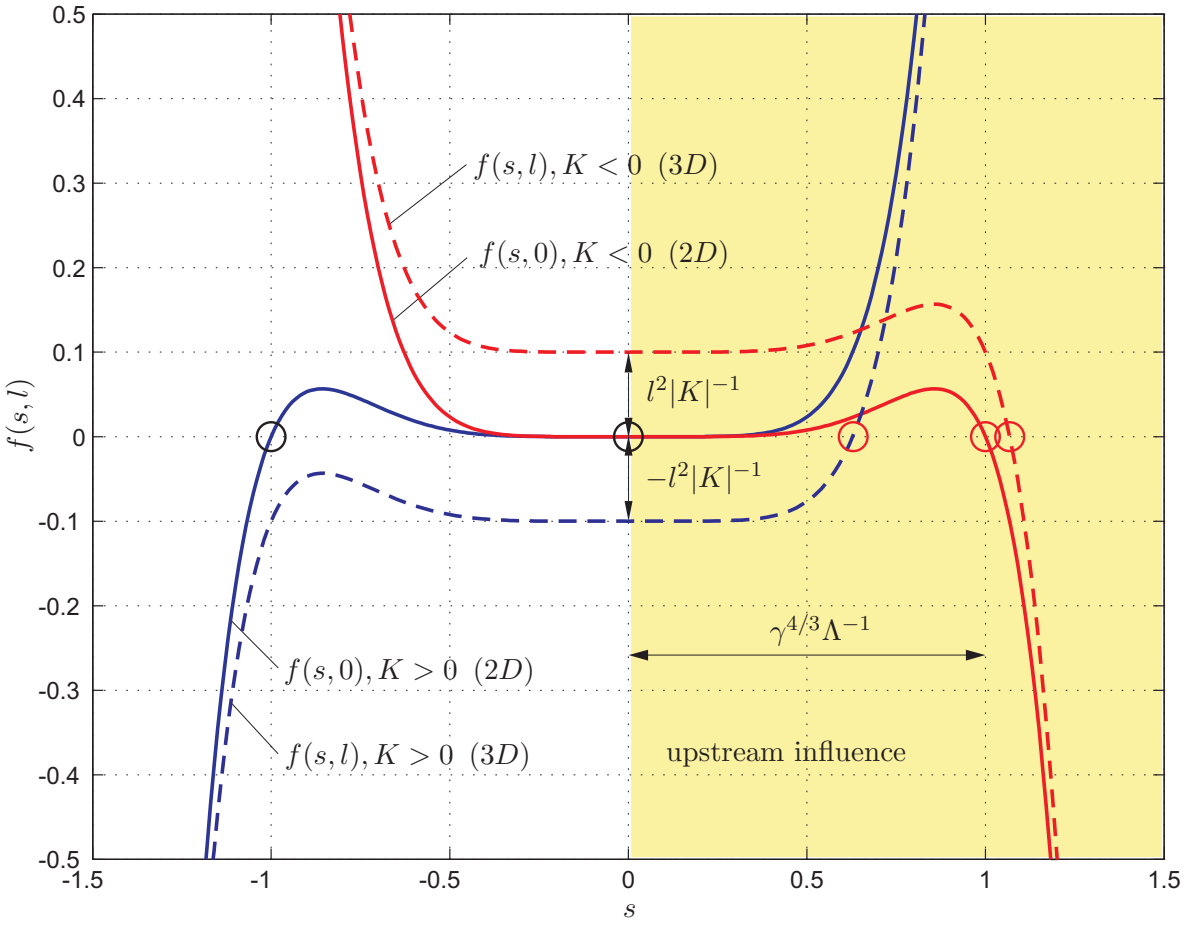

Figure 5.1.: Zeros (circles) of the denominator function $f(s,l)$ under supersonic flow conditions (red lines) and subsonic flow conditions (blue lines).

5.2. Decay of the Upstream Perturbations

Since we have shown, that there is an upstream effect under supersonic as well as under subsonic flow conditions indeed, the obvious consequence is to ask for the decay rate of the upstream perturbation. This study is much more sophisticated than simply to show the existence of this effect since one has to perform the whole inverse Fourier transform and therefore consider more or less all poles and their exact position in the lower complex plane.

This investigation can be simplified by evaluating the field quantities at the centerline of the surface mounted hump $Z = 0$ and assuming symmetry with respect to Z. Thus one obtains by applying the inverse Fourier transform, Cauchy's residual theorem and after exchange of the order of integration and summation the following relationship for the upstream pressure perturbation

$$P(X,0) = 2\sum_n \int_0^\infty a_n(l) e^{ip_n(l)X}) dl, \tag{5.5}$$

where $a_n(l)$ denotes the residuals, $p_n(l)$ the corresponding poles and the subscript n the numbering of the poles.
Up to now the problem formulation is simplified but still exact. Unfortunately, the solution of this problem is still not feasible but the behavior far upstream, where $-X \gg 1$, can be approximated. With the same arguments as in chapter 3 the main contribution to the flow quantities far upstream are associated with values $k \ll 1$ and consequently for a non-degeneration of the governing equations the spectral variable l must be rather small also. Thus p_n and a_n are expanded into a Taylor series about the two-dimensional state $l = 0$.

$$a_n(l) = a_n(0) + a_n'(0) \cdot l + \frac{1}{2} a_n''(0) \cdot l^2 + ... \tag{5.6a}$$

$$p_n(l) = p_n(0) + p_n'(0) \cdot l + \frac{1}{2} p_n''(0) \cdot l^2 + ... \tag{5.6b}$$

Here the prime and double prime denotes the first and second derivative with respect to l, respectively.
Substituting expansion (5.6) into equation (5.5) and evaluating the integral gives

$$P(-X \gg 1, 0) \sim 2\sum_n \left[e^{ip_n(0)X} \left(\frac{a_n(0)}{ip_n'(0)X} - \frac{a_n'(0)}{p_n'(0)^2 X^2} \right) \right]. \tag{5.7}$$

Hence one has to sum up the contributions of the poles $p_n(0)$ in the lower complex

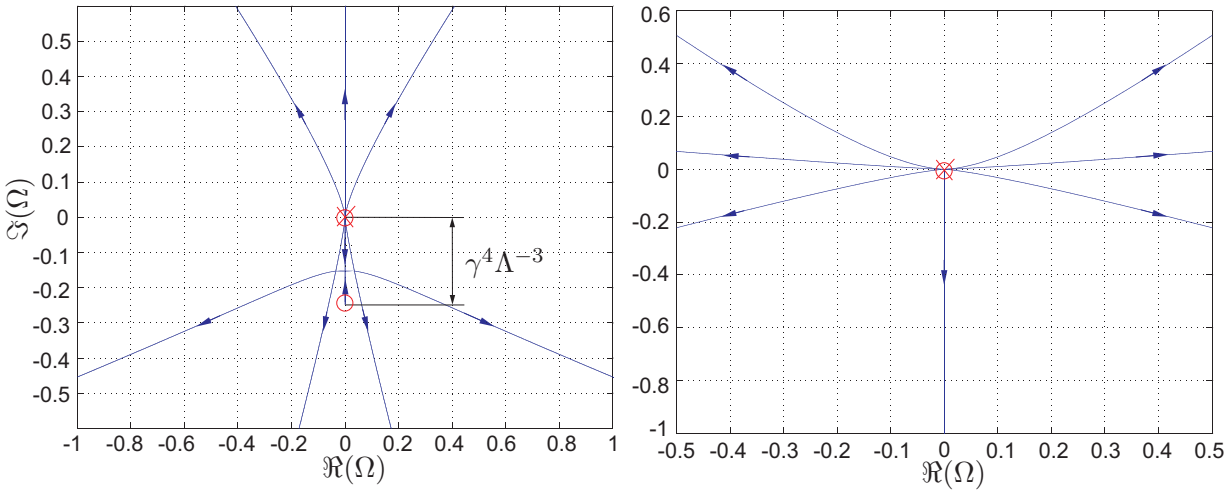

Figure 5.2.: Poles, pole traces and zeros of the transfer function Ω under supersonic (left hand side) and subsonic (right hand side) flow conditions.

plane. Figure 5.2 shows the poles $p_n(0)$ (red circles) and zeros (red crosses) of the transfer function Ω under supersonic (left hand side) and subsonic flow conditions (right hand side). The shift of the poles with respect to the spectral variable l is indicated by blue lines and referred to as traces of the poles $p_n(0)$.

Under supersonic flow conditions the contribution of the pole traces leaving the origin is negligible due to the presence of the zeros in the origin. The main contribution results from the single pole trace leaving the pole $p_1(0) = -i\gamma^4\Lambda^{-3}$. Under subsonic flow conditions the only pole traces in the lower complex plane are those three leaving the poles in the origin. The main contribution again results from a single pole trace leaving the pole $p_1(0)$ along the negative imaginary axis. The other two pole traces are negligible due to symmetry reasons ($\Re(p_2'(0)) = -\Re(p_3'(0))$) and the fact that $\Im(p_2'(0)) = \Im(p_3'(0)) = 0$. Since we are considering just the pole trace along the imaginary axis $p_1'(0) = i \cdot C$ under supersonic as well as under subsonic flow conditions, where C is a real constant, this finally yields

$$P(-X \gg 1, 0) \sim -e^{ip_1(0)X}\left(\frac{c_1}{X} - \frac{c_2}{X^2}\right), \tag{5.8}$$

where c_1, c_2 are real constants depending only on the residual $a_1(0)$ and the derivatives $a_1'(0)$ and $p_1'(0)$.

Thus the decay of the pressure perturbation far upstream a surface mounted hump under supersonic flow conditions is given by

$$P(-X \gg 1, 0) \sim -\frac{1}{X} e^{\gamma^4 \Lambda^{-3} X}, \tag{5.9}$$

where the exponent is the same as in the two-dimensional case. In the weakly three-dimensional case an additional term occurs, which yields an algebraic-exponential decay of the upstream perturbations. This is not surprising since we are studying a weakly three-dimensional problem and the solution is expected to be close to the two-dimensional one.

Comparison of this analytical result with numerical results show very good agreement as represented in figure 5.3. The numerical evaluation of the pressure perturbation upstream a surface mounted hump is shown in a logarithmic plot, cf. figure 5.3, where the results for a hump geometry with constant height in Z-direction (2D problem) are denoted by blue circles and the results for the standard cosine-squared hump by blue squares. The corresponding analytical results are indicated by solid lines. In the two-dimensional case the exponential decay appears as a straight line in the logarithmic plot, where the numerical result (blue circles) exactly coincides with the analytical found result (solid line) in the whole upstream region. The slope is determined by the eigenvalue $\phi = \gamma^4 \Lambda^{-3}$ which gives the exact exponential decay of the upstream perturbation.
In the weakly three-dimensional case the analytical result (solid line) matches the numerical one (blue boxes) quite well sufficiently far upstream. Obviously the dominant contribution for large $-X$ values is the exponential one associated with the exponential decay of the two-dimensional problem. This suggests a more or less purely two-dimensional behavior far upstream even in the weakly three-dimensional case, which will be discussed in detail in the next section.

Under subsonic flow conditions the only poles, which are considered in the inverse Fourier transform, are located at the origin $p_1(0) = 0$. The residual $a_1(0)$ and therefore the constant c_1 is found to be zero due to fact that the zeros of the transfer function Ω are located at the origin. Consequently, the decay of the upstream perturbations under subsonic flow conditions is given by

$$P(-X \gg 1, 0) \sim \frac{1}{X^2}. \tag{5.10}$$

The algebraic X^{-2} decay is significant for the subsonic behavior of three-dimensional perturbations. Figure 5.4 shows the numerical evaluation of the pressure perturbation under subsonic flow conditions, which is denoted by blue crosses, and the analytically predicted algebraic decay indicated by a solid line. The algebraic decay of the perturbation appears as a straight line with a slope of two in the double logarithmic plot. As shown in figure 5.4 the numerical results matches the analytical ones again very well even quite close to surface mounted obstacle.

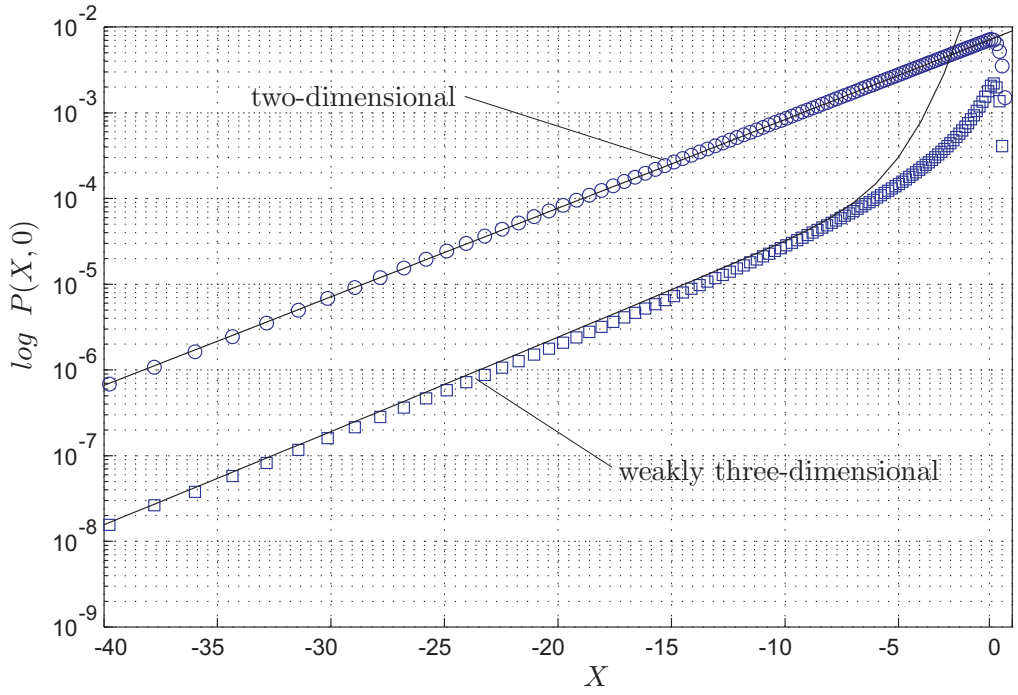

Figure 5.3.: Algebraic-exponential decay of the upstream pressure perturbation under supersonic flow conditions.

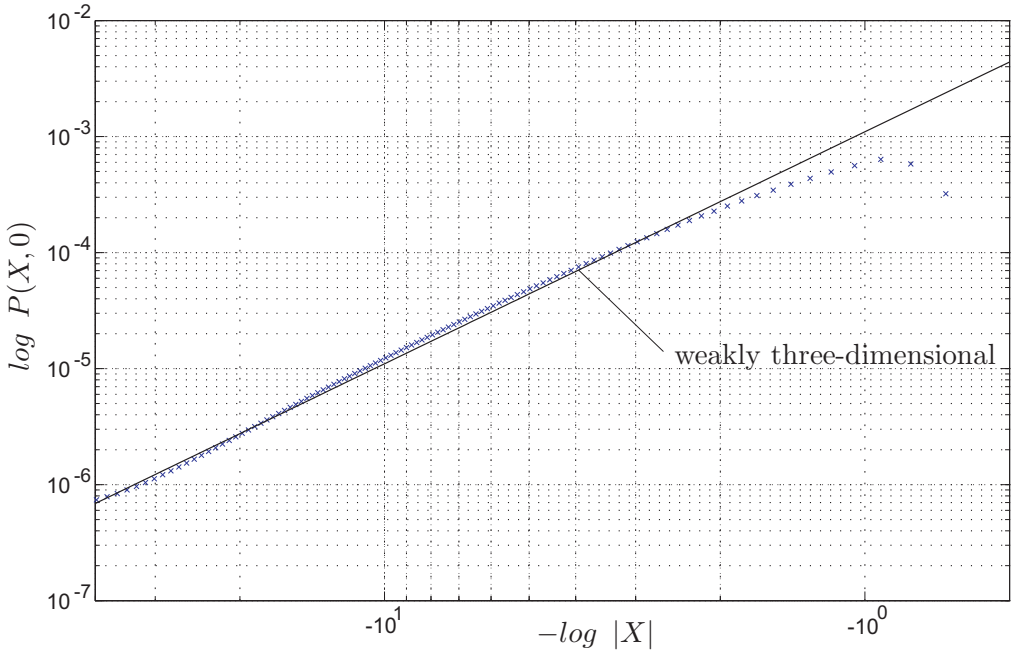

Figure 5.4.: Algebraic decay of the upstream pressure perturbation under subsonic flow conditions.

5.3. Asymptotic Structure of the Free Interaction

The motivation of studying the free interaction of the boundary layer is due to well known two-dimensional eigensolutions and their extension to the weakly three-dimensional case as well as to experimental observations.
Under supersonic flow conditions in two dimensions there exists beside the trivial undisturbed Blasius solution two further eigensolutions referred to as compressive and expansive free interaction, cf. [51]. Such a compressive eigensolution for transonic flows in nozzles corresponds to the internal shock structure of weak shocks. These regularized shock profiles resulting from shock boundary layer interaction has to connect the undisturbed flow states before and after the shock.
For subsonic external flows past a high aspect ratio wing at a supercritical angle of attack a number of authors have observed the existence of three-dimensional regions of separated flow, so called stall-cells, cf. [56], [55].
Thus the focus of the present investigation is on weakly three-dimensional eigensolutions under supersonic flow conditions, e.g. a regularized shock profile with a curved or wavy shock front, and on the possible expected formation of stall-cell patterns under subsonic flow conditions.

5.3.1. Free Interaction under Supersonic Flow Conditions

Based on the structure of the upstream influence, discussed in the previous section, solutions, which depart from the undisturbed flow algebraic-exponentially are sought. That is, we look for solutions of the form

$$U \sim Y + \frac{1}{(X-X_0)} e^{\phi(X-X_0)} cos(\beta(X)(Z-Z_0))\tilde{U}(Y), \tag{5.11a}$$

$$V \sim -\frac{1}{(X-X_0)} e^{\phi(X-X_0)} cos(\beta(X)(Z-Z_0))\tilde{V}(Y), \tag{5.11b}$$

$$W \sim \frac{1}{(X-X_0)} e^{\phi(X-X_0)} sin(\beta(X)(Z-Z_0))\tilde{W}(Y), \tag{5.11c}$$

$$P \sim -\frac{1}{(X-X_0)} e^{\phi(X-X_0)} cos(\beta(X)(Z-Z_0)), \tag{5.11d}$$

$$A \sim \frac{1}{(X-X_0)} e^{\phi(X-X_0)} cos(\beta(X)(Z-Z_0))\tilde{U}(\infty), \tag{5.11e}$$

where ϕ is again the eigenvalue of the two-dimensional problem and (X_0, Z_0) are arbitrary shifts of the solution due to their invariance with respect to X and Z. For simplicity the coordinate shift is chosen $X_0 = Z_0 = 0$ without loss of generality. Further

we assume $\beta(X) \ll 1$ and $\beta(X)' \ll 1$ for $-X \gg 1$. These assumptions seems to be arbitrarily, but it will be shown later that this conditions are satisfied indeed.

Introducing the ansatz (5.11) in the x-momentum equation (2.72b) and neglecting higher order terms yields

$$Y\tilde{U}\left(-\frac{1}{X}\phi+\frac{1}{X^2}\right)+\frac{1}{X}\tilde{V}=\left(\frac{1}{X^2}-\frac{1}{X}\phi\right)-\frac{1}{X}\tilde{U}'', \tag{5.12}$$

which gives after differentiation with respect to Y and considering the continuity equation (2.72a)

$$\tilde{U}'''-Y\tilde{U}'\left(\phi-\frac{1}{X}\right)=0, \tag{5.13}$$

where the prime denotes the derivative with respect to Y. Applying the transformation $\eta = Y\left(\phi-\frac{1}{X}\right)^{1/3}$ and introducing the shear stress perturbation $\tilde{\tau} = \frac{\partial}{\partial Y}\tilde{U}$ the Airy differential equation

$$\ddot{\tilde{\tau}}(\eta)-\eta\tilde{\tau}(\eta)=0 \tag{5.14}$$

is obtained with the solution

$$\tilde{\tau}(\eta)=C\cdot Ai(\eta)=\dot{\tilde{U}}(\eta), \tag{5.15}$$

considering no exponential growth of $\tilde{\tau}(\eta)$ for $Y\to\infty$. Rewritten in terms of $\tilde{U}$ equation (5.15) gives

$$\ddot{\tilde{U}}(\eta)=C\cdot\dot{Ai}(\eta), \tag{5.16}$$

where the dot denotes the derivative with respect to η. The integration constant C is determined by considering $\tilde{U}''(0) = -\left(\phi - X^{-1}\right) = 0$, which results from evaluating equation (5.12) at the wall.
Thus the streamwise velocity perturbation is given by

$$\tilde{U}(Y)=\frac{-\left(\phi-\frac{1}{X}\right)^{2/3}}{Ai'(0)}\int_0^Y Ai\left(\left[\phi-\frac{1}{X}\right]^{1/3}y\right)dy \tag{5.17}$$

and in the limit $Y\to\infty$ one obtaines

$$\tilde{U}(Y\to\infty)=\frac{-\left(\phi-\frac{1}{X}\right)^{1/3}}{Ai'(0)}\underbrace{\int_0^\infty Ai(\eta)d\eta}_{1/3}=-\frac{\left(\phi-\frac{1}{X}\right)^{1/3}}{3Ai'(0)}. \tag{5.18}$$

A similar evaluation of the z-momentum equations yields the Airy differential equation $\ddot{\tilde{W}}(\eta)-\eta\tilde{W}(\eta) = -\beta$ for the crossflow velocity component with $\tilde{W}(0) = \tilde{W}(Y \to \infty) = 0$. As a result we obtain

$$\tilde{W}(\eta) = \beta Ai(\eta)\mathcal{J}(\eta), \tag{5.19}$$

where $\mathcal{J}(\eta)$ is defined in equation (3.6).

Finally, by introducing ansatz (5.11) into the linearized interaction law for $K < 0$

$$-\frac{\partial^2 P}{\partial X^2} + |K|^{-1}\frac{\partial^2 P}{\partial Z^2} = \Lambda\frac{\partial^2 A}{\partial X^2} \tag{5.20}$$

and considering the above derived relations, β is given by

$$\begin{aligned}\beta(X) &= \sqrt{|K|}\sqrt{\left(\phi^2 - \frac{2}{X}\phi\right)\left(-\Lambda\frac{\left(\phi - \frac{1}{X}\right)^{1/3}}{3Ai'(0)} - 1\right)} = \\ &= \sqrt{|K|}\sqrt{\left(\phi^2 - \frac{2}{X}\phi\right)\left(\frac{\left(\phi - \frac{1}{X}\right)^{1/3}}{\phi^{1/3}} - 1\right)},\end{aligned} \tag{5.21}$$

where we used $\phi = -3Ai'(0)\Lambda^{-1}$.

Expanding this solution for $-X \gg 1$ yields

$$\beta \sim \frac{1}{\sqrt{3}}\sqrt{\frac{\phi|K|}{|X|}}. \tag{5.22}$$

Thus one can see, that β as well as β' is rather small far upstream and therefore the upstream perturbation becomes almost two-dimensional. This fact is also present in the decay of the perturbations upstream of a surface mounted obstacle, as shown in figure 5.3, where for sufficiently large negative values of X the algebraic-exponential decay tends to an exponential one as in the two-dimensional case.
We also note, that the found asymptotic structure of the upstream region (solid line), cf. figure 5.5, matches the numerical results very well even for $\beta Z \sim \mathcal{O}(1)$.

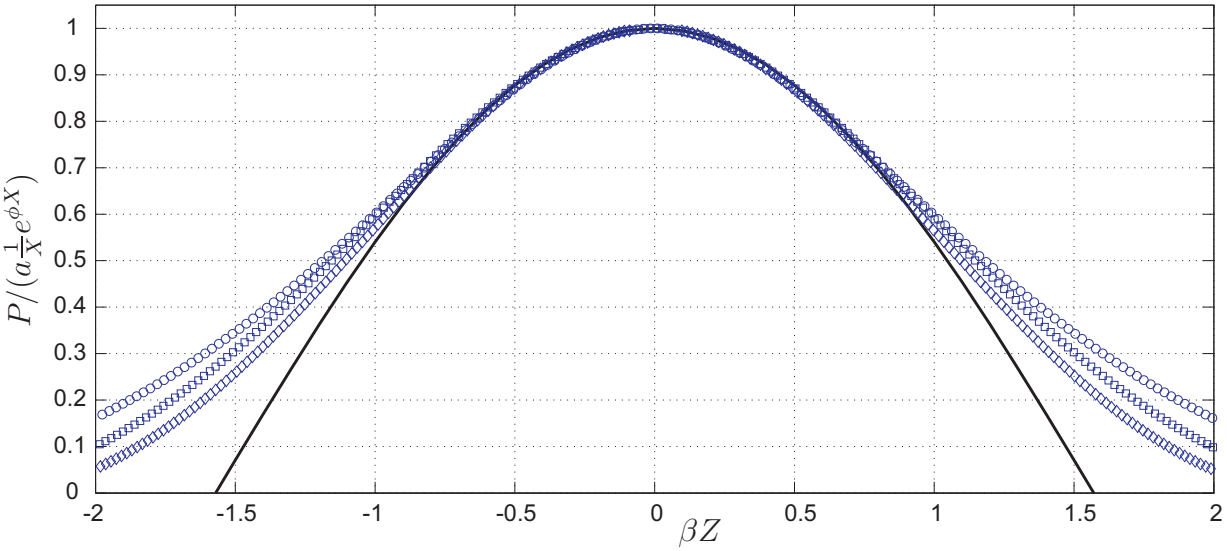

Figure 5.5.: Asymptotic structure of the upstream perturbation of the pressure under supersonic flow conditions (solid line) and numerical results for $K = -1$, $\Lambda = 1.25$ ($\bigcirc$...$X = -11.5$, $\square$...$X = -16$ and $\diamond$...$X = -20$).

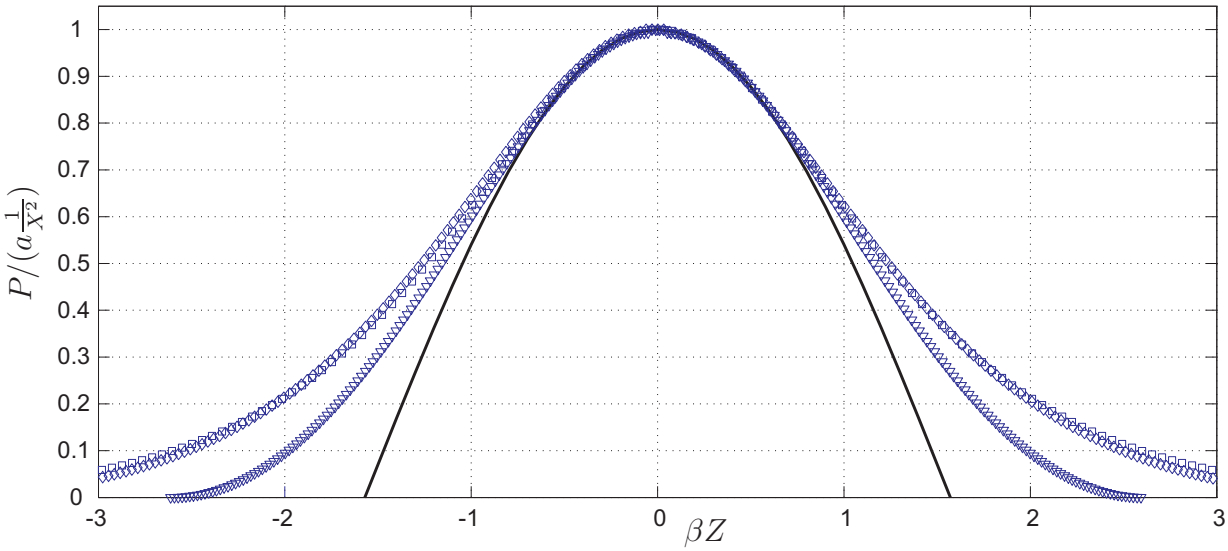

Figure 5.6.: Asymptotic structure of the upstream perturbation of the pressure under subsonic flow conditions (solid line) and numerical results for $K = 1$, $\Lambda = 1.25$ ($\square$...$X = -16$, $\diamond$...$X = -20$ and $\bigtriangledown$...$X = -35$).

5.3.2. Free Interaction under Subsonic Flow Conditions

Similar to the case of supersonic flow conditions solutions describing the structure of the upstream influence, which departure from the undisturbed flow algebraicly, are sought. Thus we look for solutions of the form

$$U \sim Y + \frac{1}{(X-X_0)^2} cos(\beta(X)(Z-Z_0))\tilde{U}(Y), \tag{5.23a}$$

$$V \sim -\frac{1}{(X-X_0)^2} cos(\beta(X)(Z-Z_0))\tilde{V}(Y), \tag{5.23b}$$

$$W \sim -\frac{1}{(X-X_0)^2} sin(\beta(X)(Z-Z_0))\tilde{W}(Y), \tag{5.23c}$$

$$P \sim -\frac{1}{(X-X_0)^2} cos(\beta(X)(Z-Z_0)), \tag{5.23d}$$

$$A \sim \frac{1}{(X-X_0)^2} cos(\beta(X)(Z-Z_0))\tilde{U}(\infty), \tag{5.23e}$$

where (X_0, Z_0) is again an arbitrary shift of the solution due to the invariance with respect to X and Z, which will be omitted in the subsequent calculations for simplicity. As before $\beta(X)$ and its derivative are assumed to be rather small for $-X \gg 1$.

Applying the same arguments and procedure as for supersonic flow conditions the streamwise velocity perturbation

$$\tilde{U}(Y) = -\frac{\left(\frac{2}{X}\right)^{2/3}}{Ai'(0)} \int_0^Y Ai\left(\left[\frac{2}{X}\right]^{1/3} y\right) dy \tag{5.24}$$

and in the limit $Y \to \infty$

$$\tilde{U}(Y \to \infty) = -\frac{\left(\frac{2}{X}\right)^{1/3}}{Ai'(0)} \underbrace{\int_0^\infty Ai(\eta) d\eta}_{1/3} = -\frac{\left(\frac{2}{X}\right)^{1/3}}{3Ai'(0)} \tag{5.25}$$

is obtained. Similarly as for supersonic flows the crossflow velocity component is given by

$$\tilde{W}(\eta) = \beta Ai(\eta)\mathcal{J}(\eta), \tag{5.26}$$

where $\mathcal{J}(\eta)$ is defined in equation (3.6) and $\eta = \left(\frac{2}{X}\right)^{1/3} Y$.

By introducing ansatz (5.11) into the linearized interaction law for $K > 0$

$$\frac{\partial^2 P}{\partial X^2} + |K|^{-1}\frac{\partial^2 P}{\partial Z^2} = \Lambda\frac{\partial^2 A}{\partial X^2}, \tag{5.27}$$

finally yields the relation

$$\beta(X) = \frac{\sqrt{6|K|}}{X}\sqrt{\left(\frac{\Lambda \cdot 2^{2/3} \cdot 44}{9^2}X^{-1/3} + 1\right)} \tag{5.28}$$

for subsonic conditions. Far upstream, where $-X \gg 1$, β is given by

$$\beta \sim \frac{1}{X}\sqrt{6|K|}. \tag{5.29}$$

Similar as for supersonic flow conditions β as well as β' is rather small far upstream and therefore the upstream perturbation becomes almost two-dimensional. The asymptotic structure of the upstream region (solid line), cf. figure 5.6, matches the numerical results very well even for $\beta Z \sim \mathcal{O}(1)$.

5.4. Eigensolutions and Internal Shock Structures

The asymptotic structure of the free interaction region, studied in the previous section, suggests the occurrence of non-trivial eigensolutions similar to the well known two-dimensional eigensolutions.
The compressive eigensolution of the two-dimensional problem corresponds to the situation of a weak normal shock in the channel. The flow field in the boundary layer is subjected to an almost discontinuous pressure distribution, i.e. a rapid change of the flow field, and a region of shock boundary layer interaction emerges around the position of the shock. This transonic viscous inviscid interaction mechanism is different from the thoroughly discussed effect of thermo-viscous regularization, cf. [13], [14] or [25], caused by small effects of viscosity and heat conduction. The shock-boundary layer interaction leads to a smooth transition from super- to subsonic flow in the core region connecting the undisturbed supersonic state upstream $P(X \to -\infty) = 0$ and the subsonic state far downstream $P(X \to \infty) = 2$, where sonic conditions in the core region are obtained for $P = 1$.

Such an eigensolution can be triggered for instance by a surface mounted hump far downstream. Thus weakly three-dimensional shock profiles, e.g. shock profiles with a curved shock front, similar to the two-dimensional profiles might be expected and maybe also the formation of stall cells under subsonic flow conditions.
In the subsequent studies only the formation of weakly three-dimensional internal shock profiles are investigated. First, solutions triggered by hump geometries deviating slightly from constant geometries with respect to Z (2D geometry) are discussed followed by obstacles with higher developed three-dimensionality.

5.4.1. Slightly Deformed Two-Dimensional Hump

In the two-dimensional case a compressive eigensolution can be triggered by perturbing the flow with a surface mounted hump far downstream. By increasing the hump height until a critical value is reached such an eigensolution emerges in front of the hump, which is shifted upstream for increasing values of h_{hump} and becomes invariant with respect to the streamwise coordinate for $h_{hump} \to h_{crit}$.

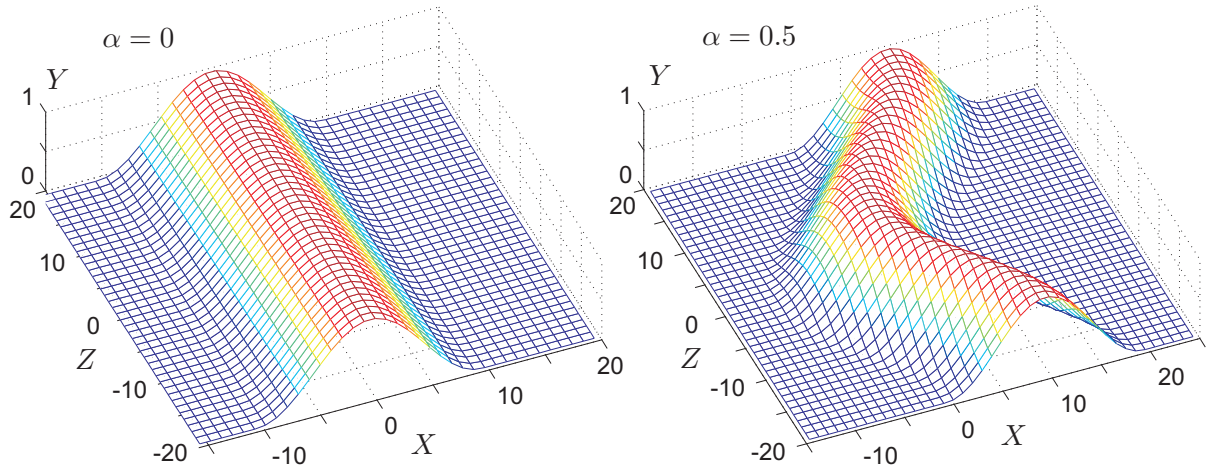

Figure 5.7.: Constant hump geometry with respect to Z ($\alpha = 0$) (left hand side) and deformed hump geometry ($\alpha = 0.5$) (right hand side).

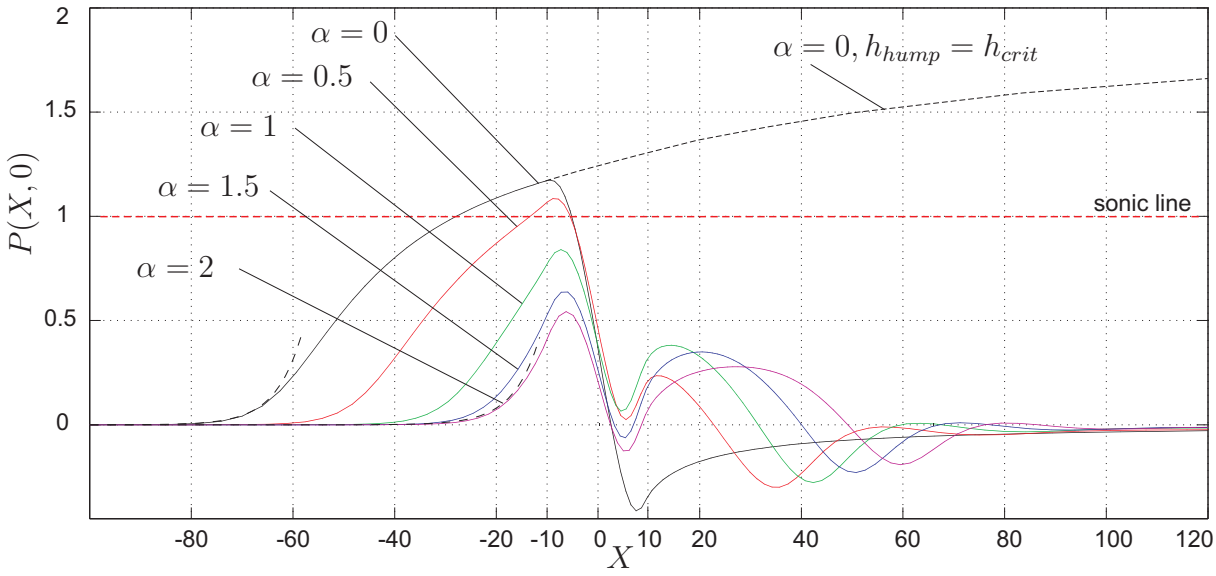

Figure 5.8.: Pressure perturbation along the centerline $Z = 0$ for various deforming parameters α, $h_{hump} = 1.25, \Lambda = 1.25, K = -1$.

To study the effect of a hump geometry deviating slightly from a two-dimensional one on the three-dimensionality of the shock profile the geometry

$$S(X,Z) = \begin{cases} h_{hump} \cdot cos^2\left(\frac{\pi}{2}\sqrt{(0.1X)^2 + (0.1\hat{Z})^2}\right), & \text{for } \sqrt{(0.1X)^2 + (0.1\hat{Z})^2} \leq 1, \\ 0, & \text{otherwise,} \end{cases}$$

is introduced, where $\hat{Z} = \alpha \cdot cos(\frac{2\pi}{Z_{max}}Z) - 1$. Here α is a deformation parameter, Z_{max} denotes the width of the periodic domain and $h_{hump} < h_{crit}$.
By mounting a hump with $h_{hump} = h_{crit}$ and $\alpha = 0$ far downstream a two-dimensional shock profile as shown in figure 5.8 is triggered. For $h_{hump} < h_{crit}$ the shock profile is shifted downstream towards the wall deformation, but the emerging shock profile in front of the hump is still recovered. To study the effect of increasing values of the deformation parameter α on the shape of the regularized shock profile the hump height is taken as $h_{hump} = 1.25 < h_{crit}$.

For $\alpha = 0$ the flow in front of the hump is decelerated such that subsonic flow conditions in the upper deck ($P > 1$) are reached at $X - 28$. The pressure distribution, cf. figure 5.8, in front of the hump shows the characteristic shape of a regularized shock profile. The exponential decay of this eigensolution is indicated by a dashed line.
By increasing the deformation parameter the pressure perturbation becomes weaker and the front of the shock profile is shifted downstream towards the hump. Already for $\alpha = 1$ the pressure perturbation becomes that weak, that a subsonic region in the upper deck is not formed anymore. For $\alpha = 2$ the front of the shock profile is shifted about two hump length towards the hump.
Furthermore, it is observed that the flow becomes almost two-dimensional a few hump lengths upstream independently of the size of the deformation parameter.

5.4.2. The Periodic Ridge

Since the flow field becomes two-dimensional a few hump lengths upstream the wavy shaped surface deformation discussed in the previous section a higher three-dimensionality of the hump may allow to trigger a weakly three-dimensional eigensolution. Thus the periodic ridge as defined by

$$S(X,Z) = \begin{cases} h_{hump} \cdot cos^2\left(\frac{\pi}{2}\sqrt{(0.1X)^2 + (0.1Z)^2}\right), & \text{for } |0.1X| \leq 1, \\ 0, & \text{otherwise} \end{cases}$$

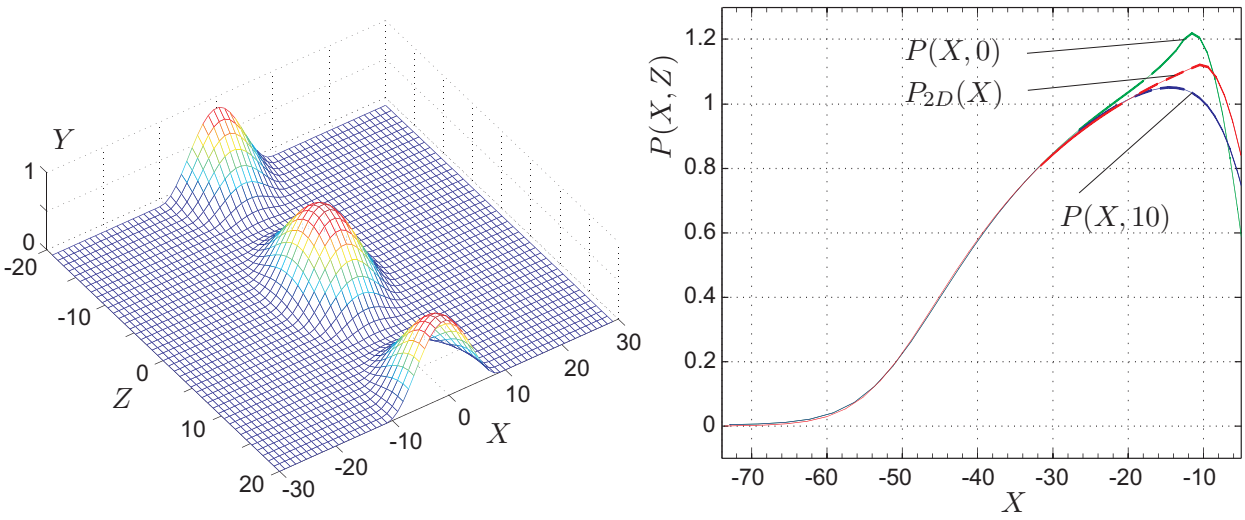

Figure 5.9.: Periodic ridge with respect to Z (left hand side) and corresponding pressure perturbation P (right hand side) for $\Lambda = 1.25$, $K = 1$ and $h_{hump} = 2.25$.

is introduced. Before starting the discussion of the numerical results further insight is gained by studying the linearized lower deck equations far upstream.

By assuming a non-degeneration of the linearized solutions with respect to the spectral variable l this yields the condition $l \sim \mathcal{O}(k^{7/6})$. Since the main contribution far upstream results from values of $k \ll 1$ the dominating values of l are rather small. Therefore the flow far upstream just 'sees' a two-dimensional surface deformation

$$S_{2D}(X) = \frac{1}{2\pi} \int_{-\infty}^{\infty} S(X, Z) dZ,$$

which results from averaging the original three-dimensional obstacle in lateral direction. Hence the flow field upstream a three-dimensional surface deformation becomes two-dimensional independent of the shape of the deformation and identically with the flow field upstream of a two-dimensional obstacle resulting from averaging the original obstacle in crossflow direction.

These analytical considerations are perfectly supported by the numerics. For the periodic ridge as shown in figure 5.9 the pressure perturbation upstream the ridge along the peak line $P(X, 0)$ and exactly between two humps $P(X, 10)$ is plotted. As suggested by previous considerations the flow field becomes two-dimensional just a few hump lengths upstream the surface deformation. Furthermore these analytical considerations, gained from the linearized formulation, seem to be valid even for quite large perturbations of the field quantities.

Moreover, the flow field far upstream of the periodic ridge coincides perfectly with the results found upstream a two-dimensional hump $P_{2D}(X)$ with a surface geometry obtained by properly averaging the periodic ridge in lateral direction.

This finding also explains the results for various deformation parameters in the previous section. Since the oncoming flow upstream just 'sees' a two-dimensional surface deformation and the height of the averaged geometry decreases with increasing values of the deformation parameter the perturbation of the flow field upstream becomes weaker and thus the emerging shock profile is shifted towards the hump.

The flow field far upstream of the obstacle becomes two-dimensional independently of the shape of the wall deformation. Hence, it seems not possible to trigger a weakly three-dimensional eigensolution by perturbing the flow with a three-dimensional surface mounted obstacle far downstream.

5.4.3. The Single Cosine-Squared Hump

Since the analytical results of the previous section are gained by studying the linearized problem a further attempt to trigger a weakly three-dimensional eigensolution is to increase the height of the hump as well as to further increase the three-dimensionality of the surface deformation. Therefore we study the flow field in front of a single cosine-squared hump as defined in chapter 3.

By increasing the hump height one might expect a dominant role of the nonlinear terms with respect to the linear ones and thus to trigger an eigensolution upstream the wall deformation in contrast to the predictions of the linearized theory.
Indeed, for increasing values of h_{hump} a three-dimensional upstream flow structure is found, but just for rather small values of the hump height. Furthermore no steady solutions for values of h_{hump} larger than a critical value h_c are found.
This effect is not only apparent under supersonic flow conditions but also under subsonic conditions. These results are noteworthy since there is no obvious reason for such a critical value. In the two-dimensional case a similar critical value of the height of the wall deformation is found, which is associated with a blocking of the nozzle and chocked flow. In contrast to the blocking in the two-dimensional case there must be another physical reason for this critical hump height in the weakly three-dimensional case since due to the additional degree of freedom the flow can always pass the obstacle.

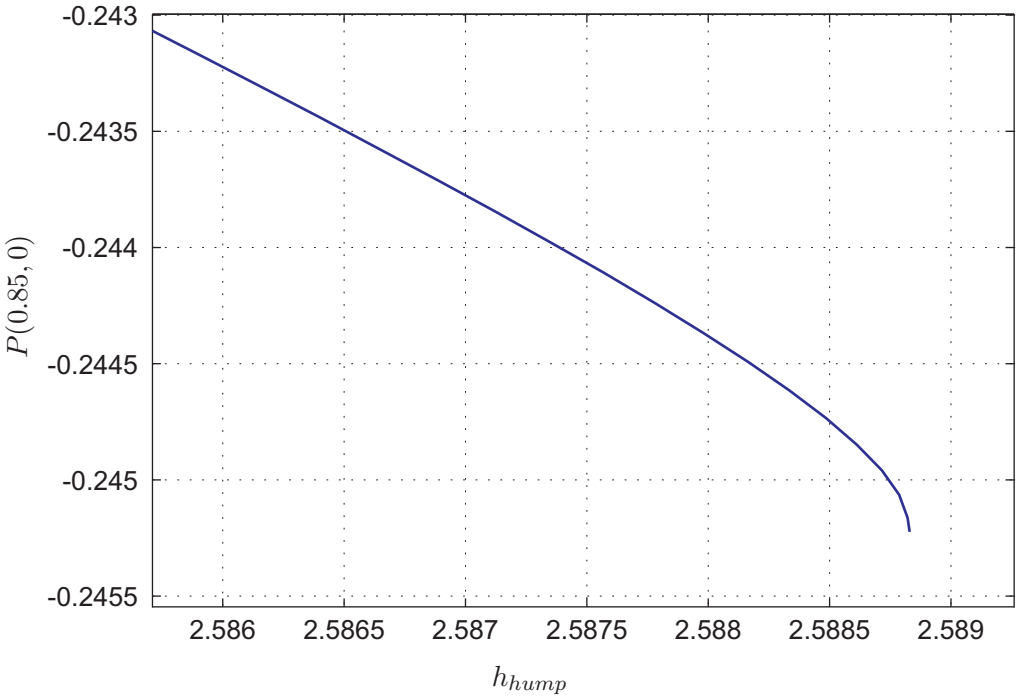

Figure 5.10.: Pressure perturbation for various hump height at $X = 0.85$, $Z = 0$ under subsonic flow conditions for $\Lambda = 1.25$ and $K = 1$.

Studying the flow field for various hump heights, as shown in figure 5.10 for the pressure perturbation, indicates a singular behavior for $h_{hump} \rightarrow h_c$. The local structure of the flow field in vicinity of h_c suggests a second, a lower branch and a non-uniqueness of the solutions.

To gain further insight into this effect numerical solutions on the lower branch are sought and a local analysis of the bifurcation (turning point) is performed, which is the topic of the next chapter.

6. Bifurcating Solutions and Local Analysis of the Bifurcation Point

6.1. Bifurcating Solutions

Numerical results for the cosine-squared hump show, that the height of this hump cannot be increased unlimited in the steady case for both supersonic as well as subsonic flow conditions. There exists a critical height h_c, where for $h_{hump} > h_c$ no steady solutions are found anymore. A singular behavior is indicated for $h_{hump} \to h_c$, which suggests the existence of a lower solution branch leading to non-unique solutions of the flow field.

For the subsequent studies only the behavior of the flow under subsonic conditions ($K > 0$) is considered. To find further solutions also on the expected lower branch the numerical algorithm is slightly modified. Instead of prescribing the hump height and solving for the resulting flow field, one flow quantity is prescribed in a single point of the calculation domain, e.g. the wall shear stress $\tau_w(0.85, 0)$ at the lee side of the hump, and the corresponding height of the hump is part of the solution. For details see appendix B. Furthermore a path-following strategy is applied to obtain reliable results also on the unstable lower branch.

As shown in figure 6.1 there exists a lower solution branch and a turning point appears at $h_{hump} = h_c$, which divides the solutions into an upper and a lower branch. Moreover, a significant change in shape of the lower branch is found at $h_{hump} = 2.37$, which suggests some significant changes also in the flow behavior. The upper branch is expected to be the stable one, while the lower branch consequently is an unstable one.
Due to this branching of the solutions a non-uniqueness is obtained. To each solution on the upper branch in vicinity of the bifurcation point there exists a second solution on the lower branch for the same hump height.
Evaluating the pressure perturbation (red lines) and the wall shear stress (blue lines)

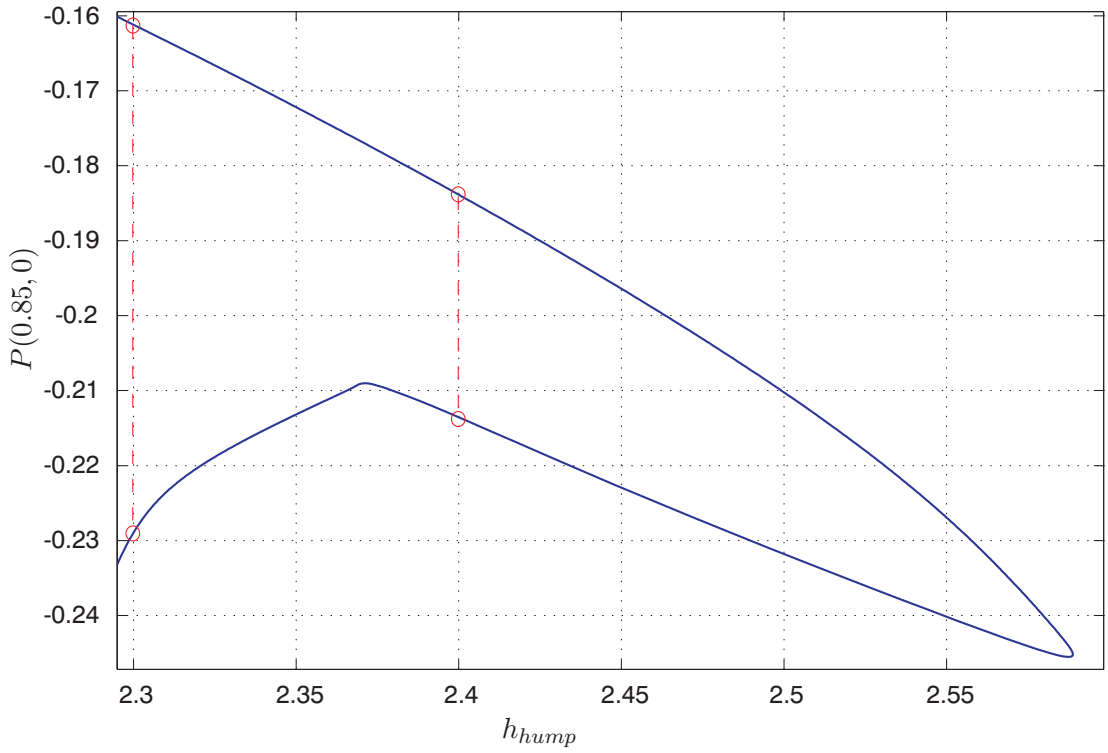

Figure 6.1.: Bifurcation curve of the pressure perturbation $P(X = 0.85, Z = 0)$ near the bifurcation point $h_c = 2.588$, $\Lambda = 1.25$, $K = 1$.

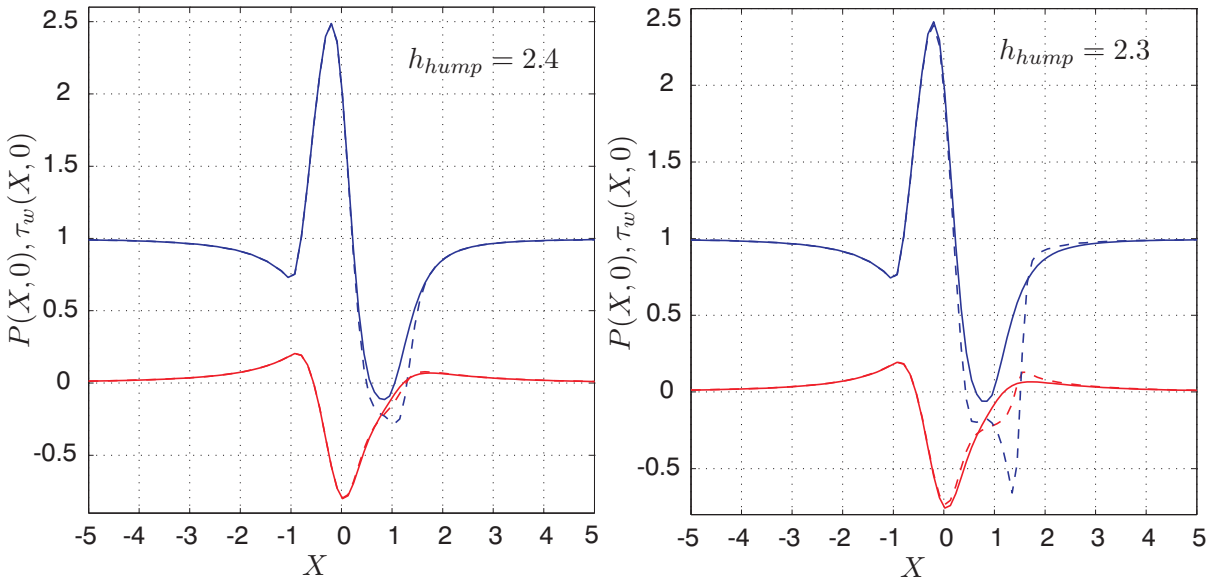

Figure 6.2.: Pressure perturbation (red) and wall shear stress (blue) associated with the upper branch (solid line) and the corresponding lower branch solution (dashed) for $h_{hump} = 2.4$ (left hand side) and $h_{hump} = 2.3$ (right hand side).

for a fixed hump height as plotted in figure 6.2, shows that the upper branch (solid line) and the lower branch (dashed line) solution differs in a small region at the lee side of the hump only, while far upstream and downstream, respectively, both solutions coincide again. Both solutions are seen to differ in a region, where also flow separation occurs. This observation suggests, that the bifurcation is somehow associated with the flow separation similar to the well studied problem of marginal separation, cf. S. Braun and A. Kluwick [6] and Kluwick et al. [32], where similar effects are apparent. Furthermore, a major change of the pressure perturbation and the wall shear stress in the reversed flow region of the lower branch solution for $h_{hump} < 2.37$ occurs, cf. figure 6.1. A new minimum in the wall shear stress evolves, which yields a highly unstable flow structure. This property is clearly visible also in figure 6.1 and responsible for the kink of the lower branch at $h_{hump} = 2.37$.

6.2. Local Analysis of the Bifurcation Point

To validate the numerical results summarized in figure 6.1 and figure 6.2 and to gain further insight into the flow structure close to the bifurcation point a local analysis of this turning point is performed, cf. [7]. The methods of bifurcation theory generally indicate a strong dimension reduction in the vicinity of a bifurcation point. The spatial structure is determined by critical modes and the evolution of the system and thus the stability is given by a bifurcation equation for the other passive modes, cf. [53].

Starting point of the subsequent analysis is the Fundamental Lower Deck problem as stated in the equations (2.72) and (2.78). Since we are studying the weakly three-dimensional problem and thus the crossflow velocity component W neither enters the continuity and x-momentum equation nor the interaction law the z-momentum equation (2.72c) will be omitted in the subsequent analysis. Thus the Lower Deck problem can be rewritten in the vector form

$$(0, 0, \dot{P}, 0)^T = \mathcal{N}(\boldsymbol{r}, h_{hump}), \tag{6.1}$$

where $\boldsymbol{r} = (U, V, P, A)^T$ and the height h_{hump} denotes the bifurcation parameter. The studied cosine-squared wall deformation is defined as

$$S(X, Z) = \begin{cases} h_{hump} \cdot cos^2(\frac{\pi}{2}\sqrt{X^2 + Z^2}) = h_{hump} \cdot \hat{S}, & \text{for } \sqrt{X^2 + Z^2} \leq 1, \\ 0, & \text{otherwise.} \end{cases}$$

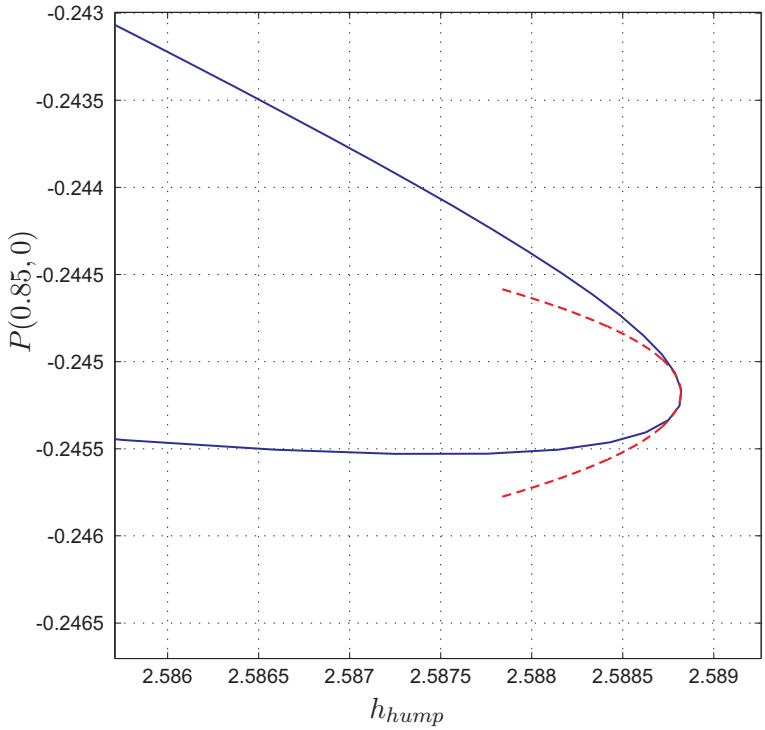

Figure 6.3.: Pressure perturbation with parabola approximation near the bifurcation point.

To perform a local analysis about the turning point a small perturbation parameter

$$\varepsilon_h = \sqrt{|h_c - h_{hump}|} = \sqrt{\Delta h}, \tag{6.2}$$

is introduced, which measures the distance from the critical point (turning point). Consequently the hump height is given by $h_{hump} = h_c - \varepsilon_h^2 sign(\Delta h)$. The parabolic shape of the bifurcation curve, cf. figure 6.3, suggest the following asymptotic expansions of the flow quantities

$$\boldsymbol{r} = \boldsymbol{r_c} + \varepsilon_h \boldsymbol{r_1} + \varepsilon_h^2 \boldsymbol{r_2} + \mathcal{O}(\varepsilon_h^3). \tag{6.3}$$

To ensure that the time dependency enters first in the second order approximation the appropriate slow time variable is found to be

$$T = \varepsilon_h^2 t. \tag{6.4}$$

Substitution of the expansions (6.3) and (6.4) into equation (6.1) yields in the leading order approximation the solution of the problem $\mathcal{N}(\boldsymbol{r}) = 0$ evaluated at the critical point $h_{hump} = h_c$

$\mathcal{O}(1)$:

$$\mathcal{N}(\boldsymbol{r_c}) = \mathbf{0} = \begin{pmatrix} \frac{\partial U_c}{\partial X} + \frac{\partial V_c}{\partial Y} \\ U_c\frac{\partial U_c}{\partial X} + V_c\frac{\partial U_c}{\partial Y} + \frac{\partial P_c}{\partial X} - \frac{\partial^2 U_c}{\partial Y^2} \\ \frac{1}{2}P_c^2 + sign(K)P_c - \Lambda A_c + h_c\hat{S} + \frac{1}{|K|}\int_{-\infty}^{X}\int_{-\infty}^{\zeta}\frac{\partial^2 P_c(\xi,Z,t)}{\partial Z^2}d\xi d\zeta \\ \lim_{Y\to\infty}[U_c - Y] - A_c \end{pmatrix} \tag{6.5}$$

and in higher orders

$\mathcal{O}(\varepsilon_h)$:

$$\mathcal{L}(\boldsymbol{r_1}) = \mathbf{0} = \begin{pmatrix} \frac{\partial U_1}{\partial X} + \frac{\partial V_1}{\partial Y} \\ U_1\frac{\partial U_c}{\partial X} + U_c\frac{\partial U_1}{\partial X} + V_1\frac{\partial U_c}{\partial Y} + +V_c\frac{\partial U_1}{\partial Y} + \frac{\partial P_1}{\partial X} - \frac{\partial^2 U_1}{\partial Y^2} \\ \frac{\partial}{\partial X}\left(P_cP_1 + sign(K)P_1 + \frac{1}{|K|}\int_{-\infty}^{X}\int_{-\infty}^{\zeta}\frac{\partial^2 P_1(\xi,Z,T)}{\partial Z^2}d\xi d\zeta - \Lambda A_1\right) \\ \lim_{Y\to\infty}[U_1] - A_1 \end{pmatrix}, \tag{6.6}$$

$\mathcal{O}(\varepsilon_h^2)$:

$$\begin{aligned}(0,0,\dot{P}_1,0)^T - \mathcal{L}(\boldsymbol{r_2}) + g(\boldsymbol{r_1}) = \mathbf{0} = \\ = \begin{pmatrix} 0 \\ 0 \\ \dot{P}_1 \\ 0 \end{pmatrix} - \mathcal{L}(\boldsymbol{r_2}) + \begin{pmatrix} 0 \\ U_1\frac{\partial U_1}{\partial X} + V_1\frac{\partial U_1}{\partial Y} \\ \frac{\partial}{\partial X}\left(P_1^2 + \Lambda\hat{S}sign(\Delta h)\right) \\ 0 \end{pmatrix},\end{aligned} \tag{6.7}$$

where $\boldsymbol{r_i} = (U_i, V_i, P_i, A_i)^T$ is the vector of the asymptotic expansions of the flow quantities.

Thus, we can conclude from the $\mathcal{O}(\varepsilon_h)$ equation

$$\boldsymbol{r}_1 = c(T)\boldsymbol{m}(x,y,z) = c(T)\begin{pmatrix} m_1(x,y,z) \\ m_2(x,y,z) \\ m_3(x,z) \\ m_4(x,z) \end{pmatrix}, \tag{6.8}$$

where $\boldsymbol{m}(x,y,z)$ is the critical right eigenfunction of $\mathcal{L}$ to the corresponding critical eigenvalue zero and $c(T)$ a time dependent shape function.

The $\mathcal{O}(\varepsilon_h^2)$ equation can be rewritten in the form

$$\mathcal{L}(\boldsymbol{r}_2) = \underbrace{(0,0,\dot{P}_1,0)^T + g(\boldsymbol{r_1})}_{\boldsymbol{g}}. \tag{6.9}$$

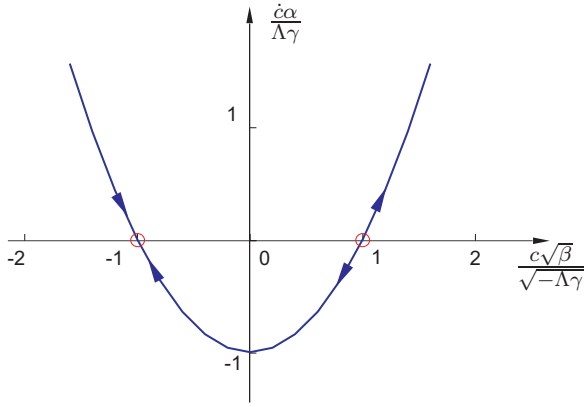

Figure 6.4.: Phase curve of the bifurcation equation with stable and unstable stationary points corresponding to the upper and lower branch solution in the subcritical case ($sign(\Delta h) > 0$).

Applying Fredholms alternative, which states that the equation $\mathcal{L}(\boldsymbol{r}) = \boldsymbol{g}$ has a solution if and only if the inner product $< \boldsymbol{n}, \boldsymbol{g} >= 0$ for every $\boldsymbol{n}$ in the nullspace of the adjoint operator $\mathcal{L}^\dagger$, yields the solvability condition

$$< \boldsymbol{n}, \mathcal{L}(\boldsymbol{r}) >=< \boldsymbol{r}, \underbrace{\mathcal{L}^\dagger(\boldsymbol{n})}_{0} >= 0, \tag{6.10}$$

where $\boldsymbol{n} = (n_1, n_2, n_3, n_4)^T$ is obviously the left eigenfunction of $\mathcal{L}$ to the corresponding critical eigenvalue and the inner product is defined as $< \boldsymbol{n}, \boldsymbol{g} >= \int_{-\infty}^{\infty}\int_{0}^{\infty}\int_{-\infty}^{\infty} \boldsymbol{n} \cdot \boldsymbol{g} dX dY dZ$.
Therefore the bifurcation equation

$$\begin{aligned} &\underbrace{< n_3, m_3 >}_{\alpha}\dot{c} + \underbrace{(< n_3, \frac{\partial}{\partial X}(m_3^2) > + < n_2, m_1\frac{\partial}{\partial X}m_1 + m_2\frac{\partial}{\partial Y}m_1) >)}_{\beta} c^2 + \\ &+ sign(\Delta h)\Lambda \underbrace{< n_3, \frac{\partial}{\partial X}(\hat{S}) >}_{\gamma} = 0. \end{aligned} \tag{6.11}$$

is obtained, which finally yields

$$\dot{c} + \frac{\beta}{\alpha}c^2 + sign(\Delta h)\frac{\Lambda\gamma}{\alpha} = 0. \tag{6.12}$$

The stationary points in the subcritical case $sign(\Delta h) > 0$, where $\dot{c} = 0$, are given by

$$c_s = \pm\sqrt{-\frac{\Lambda\gamma}{\beta}}, \tag{6.13}$$

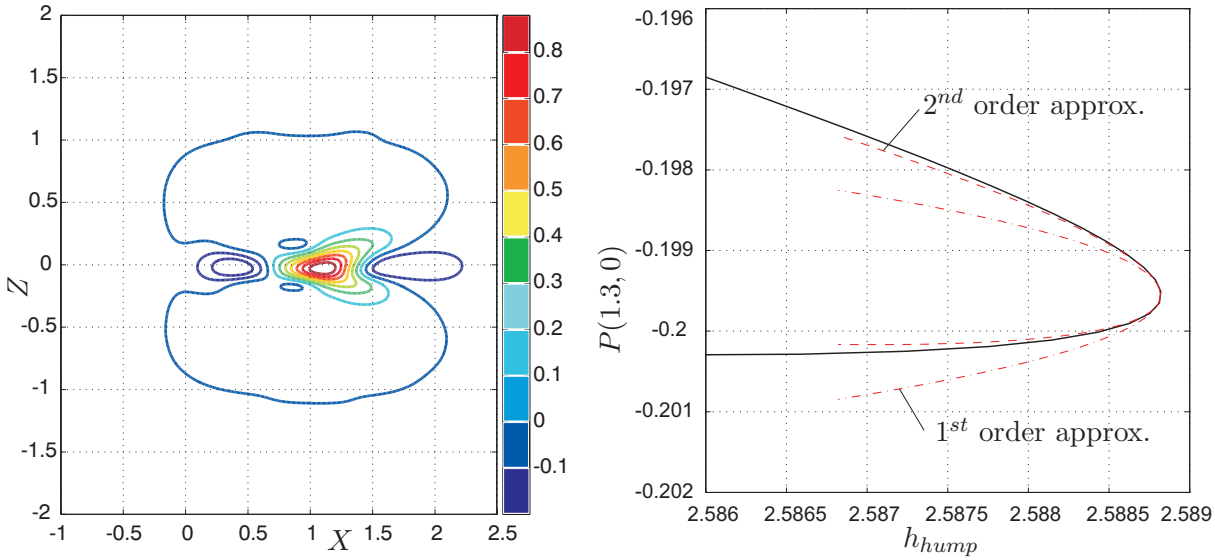

Figure 6.5.: Right eigenfunction $m_3(X, Z)$ (left hand side) and approximation of the pressure perturbation ($P \sim P_c + \sqrt{\Delta h} \cdot c_s m_3 + \Delta h \cdot P_2$) close to the turning point (h_c, P_c) (right hand side).

where the two solutions correspond to the upper branch and lower branch solution, respectively. The phase curve, as shown in figure 6.2, indicates that the positive value of c_s yields a stable stationary point corresponding to the upper branch solutions and the negative value of c_s gives an unstable stationary point corresponding to the lower branch solutions. This instance is also confirmed by the numerical results of the previous chapter.

Obviously there exists no real solution and thus no stationary points in the supercritical case $sign(\Delta h) < 0$. The imaginary solutions of (6.12) suggests oscillatory solutions for $h_{hump} > h_c$ and a blow-up of the separation bubble as in the theory of marginal separation, cf. [8]. Associated with this blow-up buffeting effects might be expected.

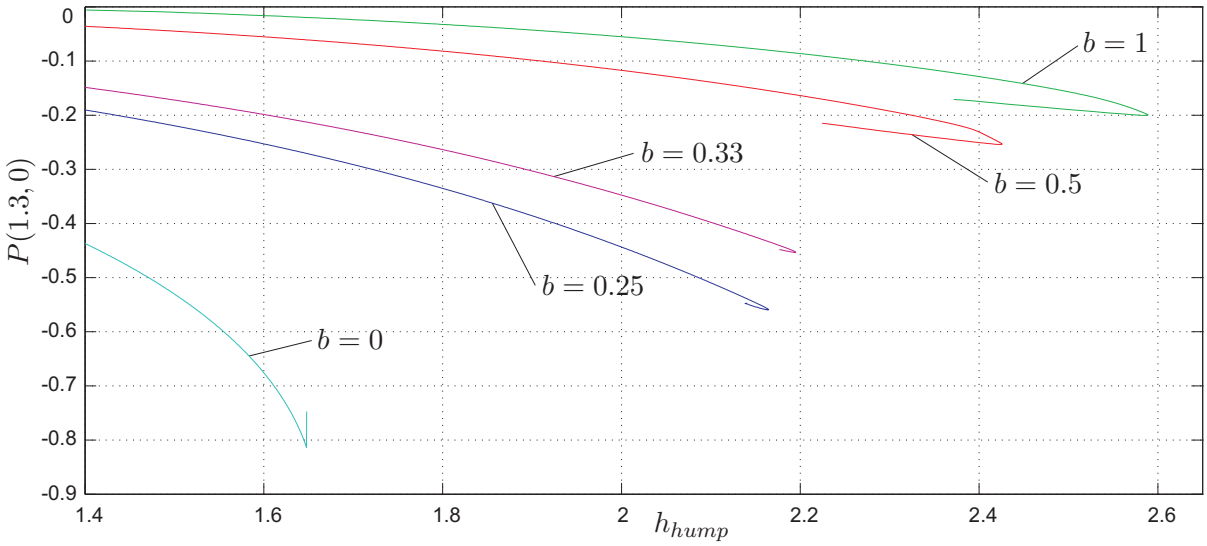

Figure 6.6.: Bifurcation curve of the pressure perturbation for various values of the hump width ($\Lambda = 1.25$, $K = 1$).

6.3. Dependence on the hump width

So far a cosine-squared wall deformation with fixed width was studied. The influence of the hump width on the bifurcation behavior, specially in the limiting case of a two-dimensional deformation, is of further interest and the topic of the subsequent studies. In the two-dimensional case there appears no such turning point, but there exists as well a critical hump height, such that no steady solutions exists for $h_{hump} > h_c$, cf. [36]. Very much alike the case of an ideal laval nozzle in classical theory this critical solution leads to a transition from the sub- to a supersonic regime. Further downstream in the divergent part of the nozzle the flow is shocked back by forming a pseudo shock due to the viscous-inviscid interaction. This pseudo shock is invariant with respect to the streamwise coordinate, which is reflected by the vertical branch at $h_{hump} = h_c$ of the bifurcation curve in figure 6.6 for $b = 0$.

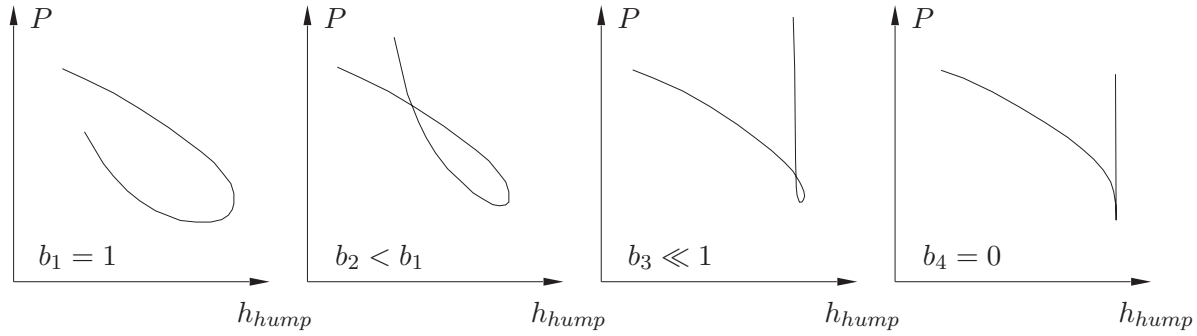

Figure 6.7.: Degeneration of the turning point bifurcation for increasing values of the hump width b_i.

This in turn suggest a degeneration of the bifurcation equation by increasing the hump width. Therefore the dependence on the hump width is studied by introducing the surface mounted obstacle

$$S(X,Z) = \begin{cases} h_{hump} \cdot cos^2(\frac{\pi}{2}\sqrt{X^2 + (b \cdot Z)^2}), & \text{for } \sqrt{X^2 + (b \cdot Z)^2} \leq 1, \\ 0, & \text{otherwise,} \end{cases}$$

where b is a stretching factor in Z-direction and a value of $b = 0$ corresponds to the two-dimensional case.
A first numerical investigation for various hump widths, as shown in figure 6.6, shows that the critical height h_c decreases for increasing values of the width, while the perturbation of the flow quantities increases. In the limiting case $b = 0$ the two-dimensional results found by G. Meyer [36] are recovered and a degeneration of the saddle-node bifurcation is observed.
More insight into the transition between the weakly three-dimensional and the two-

hump width b	1^{st} order approx. $P_1(1.3, 0)$	2^{nd} order approx. $P_2(1.3, 0)$
1	0.0195	0.29
0.5	0.0212	0.38
0.33	0.0229	0.49
0.25	0.025	0.63

Table 6.1.: 1^{st} and 2^{nd} order approx. terms for various values of the hump width b

dimensional case is gained by studying the first and second order approximations of the flow quantities in vicinity of the bifurcation point. As shown in table 6.1, the growth rate of the approximations of the pressure perturbation indicates a much faster growth of the second order approximation than of the first order one. That means, that for increasing values of the hump width the parabola of the approximation is getting slimmer and stepper. A behavior of the bifurcation curve, as sketched in figure 6.7, is suggested, which meets the results of the two-dimensional case in the limit $b \to 0$. The evolution of the bifurcation curve furthermore suggests a breakdown of the asymptotic structure (6.3) and thus a degeneration of the saddle-node bifurcation.

6.4. Future work

Further insight and a more general discussion of the degeneration of the saddle-node bifurcation is expected to be gained by studying the left eigenfunction $\boldsymbol{n}$ and the bifurcation equation (6.12). From the present point of view it seems sufficient to focus these studies on the investigation of the term $\gamma =< n_3, \frac{\partial}{\partial X}\hat{S} >$ since this is the only term, where the surface deformation $\hat{S}$ enters the equations. For $\gamma = 0$ the bifurcation equation degenerates and thus a qualitative analysis of the symmetry of the left eigenfunction and $\hat{S}$ for $b \to 0$ might yield the expected result.
Another open question of interest in this context concerns the flow behavior in the supercritical region $h_{hump} > h_c$. The results of S. Braun and A. Kluwick, cf. [8], suggest a growth of the separation bubble associated with a finite-time blow up similar to the blow up in the theory of marginal separation. A first numerical investigation of this unsteady effect performed with a time-explicit scheme, see appendix B, yields, as predicted by the theory, an unbounded growth of the separation bubble. So far it is expected that this problem can be overcome by introducing a new faster time scale, which is appropriate for the bubble dynamic. A growth of the bubble followed by bubble bursting and emerging of a new bubble leading to a periodic flow behavior is suggested. Associated with the periodic formation of separation bubbles and the interaction with the upper deck flow also pseudo shocks might appear yielding a so called buffeting effect.

7. Conclusions

In this thesis it has been shown, that the viscous inviscid interaction of weakly three-dimensional transonic flows in slender channels in the high Reynolds number range, as they appear for instance in supersonic micro nozzles and in turbomachines of micro-electro-mechanical-systems (MEMS), can be described properly by means of matched asymptotic expansions and the triple deck theory. Previous work done in this context by Kluwick [26], Gittler and Kluwick [29] and Kluwick and Meyer [30] has been extended to the weakly three-dimensional case to incorporate particularly the formation of upstream acting perturbations and bifurcating solutions. The derived "Lower Deck problem" has been studied with the focus on three main topics. First the flow over shallow surface mounted humps has been investigated by solving the linearized problem and afterwards for larger hump heights and the associated nonlinear effects numerically. Secondly, the occurrence and existence of upstream acting perturbations has been studied and finally the appearance of bifurcating solutions.

In order to gain a first insight into the complex spacial structure of the flow, the linearized problem has been studied under supersonic as well as under subsonic flow conditions. A simple source-like trend upstream the hump was found followed by some major adjustment of the crossflow velocity close to the surface near the front side of the hump, which yields a vortex motion. Then, over the back of the hump a sink-like form, in order that the fluid may encircle the obstacle has been observed and finally, downstream of the hump another vortex motion. It has been shown, that the two vortices rotate in the opposite sense. Thus four regions with a substantial different flow behavior and typically wall-jet like shaped crossflow velocity profiles were found.
The asymptotic behavior of the streamwise wall shear stress perturbation τ_w indicates a decay of $X^{-5/3}$, while the crossflow wall shear stress σ_w decays much faster with $X^{-8/3}$. Furthermore, the streamwise wall shear stress perturbation is confined to a region of about the lateral extent of the hump, while the crossflow wall shear stress spreads, which is also reflected in the wedge shaped region of the vortex motion downstream of

the hump. The decay of the pressure perturbation under subsonic flow conditions was found to be X^{-2}, which is significant for the subsonic behavior of three-dimensional perturbations. Moreover, the pressure perturbation far downstream loses any information about the geometry of the channel deformation and just keeps the information about the hump volume.
For larger hump heights it has been shown that the boundary layer is capable to separate at the lee side of the hump forming an open separation bubble with a mass flux into the bubble from both sides and a helical outflow in vicinity of the centerline $Z = 0$. Very good agreement of the angle of the separation streamline with the well known analytical result for the separation angle due to Oswatitsch [39] was found. The possibility of an emerging local subsonic or supersonic region in the upper deck flow, respectively, has been demonstrated by varying the transonic similarity parameter K, where in the limiting cases $K \to 0$ and $|K| \gg 1$ analytical solutions have been provided. These first general studies give an insight into the flow structure through slender channels as they appear in micro devices, e.g. supersonic micro nozzles for propulsion (thruster) in space applications and the channel wall deformations can be taken for instance as surface roughness. The results presented and calculations of the length scales have shown, that flow phenomena like the formation of separation bubbles, cf. chapter 4, the occurrence of compressive shock solutions, cf. chapter 5, and the existence of a limiting height of the wall deformation for steady solutions of the flow field, cf. chapter 6, should appear in such applications. But it shall be pointed out, that in the current work the oncoming boundary layer is a two-dimensional one, which might be a good approximation for nozzle flows, but which will be in general not the case for instance in micro turbomachines.

Another property of boundary layer flows considered here is the effect of upstream acting perturbations in front of a surface mounted hump. In contrast to the two-dimensional case, where such an upstream effect is observed only under supersonic flow conditions, it has been shown analytically, that there exists such an upstream effect in the weakly three-dimensional case under supersonic as well as under subsonic flow conditions. Moreover, the upstream behavior in the two-dimensional case has been recovered with the well known result of strictly no upstream effect under subsonic flow conditions. A more sophisticated study of the upstream behavior has been performed to gain the decay of the upstream perturbations, which was found to be algebraic-exponential under supersonic flow conditions and algebraic under subsonic flow conditions.

Furthermore, it has been shown, that it is not possible to trigger a weakly three-dimensional internal shock profile, for instance a shock profile with a curved shock front, by perturbing the flow with a surface mounted obstacle far downstream. The flow far upstream loses the information about the three-dimensionality of the hump and just 'sees' a two-dimensional wall deformation resulting from averaging the hump geometry with respect to the crossflow direction. This property has been shown analytically and has been confirmed by the numerical calculations for various hump geometries with a different three-dimensionality.
At this point it should be mentioned, that it is not possible to trigger such a weakly three-dimensional internal shock profile by perturbing the flow far downstream. This might be a hint that there exists no weakly three-dimensional eigensolutions, but obviously this is just a hint and no proof. Possibly, the triggering mechanism is rather different in the weakly three-dimensional case than in the two-dimensional one.

The most striking feature, which has been found is the appearance of bifurcating solutions and the emergence of the associated problem of stability. It has been shown, that there exists a critical hump height h_c, where a saddle-node bifurcation occurs and the solutions branch into a stable upper branch and an unstable lower branch. For larger values of the hump heights than this critical value no steady solution has been found, which has been confirmed by a local analysis of the bifurcation point. The solutions on the upper and the lower branch at a given hump height have been found to deviate just in vicinity of a region of reversed flow. From the present point of view the whole bifurcation behavior seems to be associated with the occurrence of a separation bubble, which is also suggested by the theory of marginal separation, cf. [7], since the bifurcation behavior there is very similar to the one discussed above.
Moreover, a degeneration of the bifurcation curve for increasing hump widths was found, which is conform with the two-dimensional result of G. Meyer [36], where no such saddle-node bifurcation occurs. A study of the first and second order approximation of the pressure perturbation in vicinity of the bifurcation point has also shown this degenerative behavior suggested by a breakdown of the asymptotic expansions for large hump widths.

Throughout the present work it has been found, that even small surface deformations embedded in the viscous lower deck of the boundary layer, such as wall roughnesses due to the manufacturing process, can considerably effect the flow structure globally for instance by triggering weak normal shocks or leading to boundary layer separation and unsteady flow structures. To avoid such effects is of vital importance in the engineering practice of micro-turbomachines, since they are designed and optimized for specified oncoming flow conditions and any perturbations lower their efficiency. On the other hand these effects might be of interest for instance for leaf seal, where a high pressure drop is aimed for.

Thus the results of this theoretical work gives some hints for an improved design of micro-devices and a guideline for the manufacturing process, specially concerning the surface roughness.

Appendices

A. List of Symbols

Latin Symbols

A	negative perturbation of the displacement thickness (displacement function)
b	stretching parameter of hump width
c	speed of sound
$c(T)$	shape function in the bifurcation equation
c_p	specific heat at constant pressure
c_v	specific heat at constant volume
f	spectral denominator function
$G(P;K,\Gamma)$	leading order term of the negative perturbation of the upper deck mass flux density
H	thickness of the upper deck, half channel height
h	specific enthalpy
h_{hump}	height of a surface mounted hump
h_c	critical hump height
$\boldsymbol{I}$	Identity matrix
$J(P;K,\Gamma)$	leading order term of the perturbation of mass flux density
$\mathcal{J}(r)$	spectral shape function of the crossflow velocity profile
K	transonic similarity parameter
k	spectral variable corresponding to X
k_λ	thermal conductivity
L	characteristic length of the channel
l	spectral variable corresponding to Z
n	number of reflections of the characteristics
p, P	pressure perturbation
$\boldsymbol{q}$	heat flux vector
$\boldsymbol{r}$	flow quantity vector

s	thermodynamic entropy
$\boldsymbol{s_h}, \boldsymbol{S}$	position vector describing the surface mounted hump
t, T	time
$\boldsymbol{u}$	velocity vector
u, U	streamwise velocity component
v, V	vertical velocity component
w, W	crossflow velocity component
$\boldsymbol{x}$	positioning vector
x, X	horizontal coordinate, streamwise direction
Δx	horizontal length of the interaction region
y, Y	vertical coordinate
z, Z	lateral coordinate, crossflow direction
Δz	width of the interaction region

Greek Symbols

α	stretching parameter
δ_l	thickness of the lower deck subregion
δ_m	thickness of the main deck subregion
ε	small perturbation parameter for the interaction region
ε_h	small perturbation parameter for the bifurcation
Γ	Fundamental derivative of gas dynamics
Δh	distance from the critical height h_c
η	mapped Y-coordinate
Λ	coupling parameter in the interaction law
λ	second coupling parameter in the interaction law
μ	dynamic viscosity
ρ, R	density
σ	crossflow shear stress
θ, Θ	temperature
ϑ_{SEP}	separation angle
$\boldsymbol{\tau}$	viscous stress tensor
τ	streamwise shear stress
Ξ	shape function of the shear stress
Ω	spectral transfer function of the pressure perturbation
$\boldsymbol{\omega}$	vorticity

Dimensionless Numbers

Ec	Eckert number
M_0	Mach number
Pr	Prandtl number
Re	Reynolds number

Superscripts

$\tilde{a}$	dimensional form of quantity a
$\bar{a}$	triple deck scaling of quantity a
a^*	quantity of fundamental lower deck problem before Prandtl's transposition theorem is applied
$\hat{a}$	perturbation of quantity a

Subscripts

0	reference state
1	first order approximation
2	second order approximation
c	quantity evaluated at the critical (bifurcation) point
l	lower deck
m	main deck
u	upper deck
s	stationary solution
w	quantity evaluated at the wall

Operators

∇	nabla operator
∇^2	laplace operator
∇a	gradient of a
$\nabla \cdot \boldsymbol{a}$	divergence of $\boldsymbol{a}$
$rot(\boldsymbol{a})$	rotation of a
$\mathcal{F}(a)^2 = a^{**}$	two-dimensional Fourier transform
$\mathcal{L}$	linear operator
$\mathcal{N}$	nonlinear operator
$\Re(a)$	real part of a
$\Im(a)$	imaginary part of a
$\boldsymbol{a}^T$	transpose of $\boldsymbol{a}$
$\mathcal{L}^\dagger$	adjoint operator of $\mathcal{L}$
$\frac{Da}{Dt} = \frac{\partial a}{\partial t} + \boldsymbol{u} \cdot \nabla a$	substantial derivative

B. Pseudo Spectral Method

To solve the full nonlinear fundamental lower deck problem (2.72) and (2.79) a pseudo spectral method, cf. [10], [15], [19], [3], is used. This method requires much less memory resources than standard numerical techniques (i.e. finite-difference schemes) in particular for three-dimensional problems, for which the finite-difference methods have not proven successful. However, a major advantage of spectral methods is to capture regions of reversed flow (i.e. boundary layer separation) without any additional approximations (e.g. FLARE-approximation for finite-difference methods). The physical problem can be solved very effectively and allows the usage of standard numerical algorithms (e.g. Fast Fourier Transform-algorithm, cf. [12]).

B.1. Preparation of the governing equations

To obtain an efficiently working numerical algorithm the governing equations are properly modified before a numerical method is applied.

First, the streamwise component of the velocity is split into its perturbed and unperturbed parts

$$U = Y + \hat{U},$$

where $\hat{U}$ denotes the perturbation of velocity profile of the oncoming boundary layer. After differentiating the x-momentum equation (2.72b) with respect to Y, the lower deck problem reads

$$\frac{\partial \hat{U}}{\partial X} + \frac{\partial V}{\partial Y} = 0, \tag{B.1a}$$

$$Y\frac{\partial^2 \hat{U}}{XY} - \frac{\partial^3 \hat{U}}{Y^3} = -V\frac{\partial^2 \hat{U}}{Y^2} - \hat{U}\frac{\partial^2 \hat{U}}{XY}, \tag{B.1b}$$

$$Y\frac{\partial W}{\partial X} - \frac{\partial^2 W}{\partial Y^2} + \frac{\partial P}{\partial Z} = -\hat{U}\frac{\partial W}{\partial X} - V\frac{\partial W}{\partial Y} \tag{B.1c}$$

and the interaction law is found to be

$$\frac{\partial P}{\partial t} - sign(K)\frac{\partial P}{\partial X} - \Lambda\frac{\partial}{\partial X}\left(A - S - \frac{1}{\Lambda\,|K|}\int_{-\infty}^{X}\int_{-\infty}^{\zeta}\frac{\partial^2 P(\xi,Z,t)}{\partial Z^2}d\xi d\zeta\right) = \frac{1}{2}P^2, \quad \text{(B.2)}$$

where one recovers the linearized problem by neglecting the right-hand-side of (B.1) and (B.2). Furthermore, the perturbation streamwise shear

$$\hat{\tau} = \frac{\partial \hat{U}}{\partial Y}$$

as well as a transformation in Y-direction

$$Y = f(\eta) = \frac{\eta}{1-\eta},$$

which is appropriate, given the decay of W indicated by (2.75) for $Y \to \infty$, is introduced. Hence, the governing equations in spectral space, considering the boundary condition (2.83), become

$$ik\int_0^\eta \tau^{**} f'(\eta)d\eta + \frac{1}{f'(\eta)}\frac{\partial V^{**}}{\partial \eta} = 0, \quad \text{(B.3a)}$$

$$ikf(\eta)\tau^{**} - \frac{\partial^2\tau^{**}}{\partial\eta^2}\frac{1}{[f'(\eta)]^2} + \frac{\partial\tau^{**}}{\partial\eta}\frac{f''(\eta)}{[f'(\eta)]^3} = \mathcal{F}^2\left\{-\frac{V}{f'(\eta)}\frac{\partial\tau}{\partial\eta} - \tau_X\int_0^\eta \tau f'(\eta)d\eta\right\}, \quad \text{(B.3b)}$$

$$ikf(\eta)W^{**} - \frac{\partial^2 W^{**}}{\partial\eta^2}\frac{1}{[f'(\eta)]^2} + \frac{\partial W^{**}}{\partial\eta}\frac{f''(\eta)}{[f'(\eta)]^3} + ilP^{**} = \mathcal{F}^2\left\{-W_X\int_0^\eta \tau f'(\eta)d\eta - \frac{VW_\eta}{f'(\eta)}\right\}, \quad \text{(B.3c)}$$

$$\frac{\partial P^{**}}{\partial t} - sign(K)ikP^{**} - \Lambda ik\left(\int_0^\infty \hat{\tau}(\eta')^{**}d\eta' - S^{**} - \frac{1}{\Lambda\,|K|}\frac{l^2}{k^2}P^{**}\right) = \frac{1}{2}\mathcal{F}^2\left\{P^2\right\}, \quad \text{(B.4)}$$

where k and l denote the spectral variables corresponding to the physical variables X and Z, respectively. The boundary conditions for this system are given by

$$V^{**} = W^{**} = 0 \qquad \text{at } Y = 0, \quad \text{(B.5a)}$$

$$\lim_{X\to-\infty}(\hat{\tau}^{**}, V^{**}, W^{**}, P^{**}) = 0, \quad \text{(B.5b)}$$

$$\lim_{\eta\to\infty} W^{**} = 0. \quad \text{(B.5c)}$$

One further boundary condition is required and arises from the x-momentum equation evaluated at $\eta = 0$, which yields

$$\frac{1}{f'(0)}\frac{\partial\tau^{**}(k,l,0,t)}{\partial\eta} = ikP^{**}(k,l,t). \quad \text{(B.6)}$$

B.2. Discretization of the Equations

Since the flow variables are mapped into spectral space only in streamwise and cross flow direction, respectively, the Y direction is discretized using conventional second order finite differences. Moreover, the time derivative is discretized using a simple first order differential quotient.

Discretization in η direction

The η-direction is discretized using a second order finite difference

$$\begin{aligned}\frac{\partial\hat{\tau}^{**}(k,l,\eta,t)}{\partial\eta} &= \frac{\hat{\tau}^{**}(k,l,\eta+\Delta\eta,t)-\hat{\tau}^{**}(k,l,\eta-\Delta\eta,t)}{2\Delta\eta},\\ \frac{\partial^2\hat{\tau}^{**}(k,l,\eta,t)}{\partial\eta^2} &= \frac{\hat{\tau}^{**}(k,l,\eta+\Delta\eta,t)-2\hat{\tau}^{**}(k,l,\eta,t)+\hat{\tau}^{**}(k,l,\eta-\Delta\eta,t)}{\Delta\eta^2},\end{aligned} \tag{B.7}$$

where $\Delta\eta = \eta_\infty/N_{max}$. Only the boundary condition (B.6) is approximated by second order backward differences to avoid the introduction of image points, to yield

$$\hat{\tau}^{**}(k,l,0,t) = -\frac{2}{3}\Delta\eta ikf'(0)P^{**}(k,l,t) - \frac{1}{3}\hat{\tau}^{**}(k,l,2\Delta\eta,t) + \frac{4}{3}\hat{\tau}^{**}(k,l,\Delta\eta,t). \tag{B.8}$$

The integral in equation (B.4) is approximated using the trapezoidal rule

$$\begin{aligned}\int_0^\infty f'(\eta)\tau^{**}d\eta = \frac{f'(0)\tau^{**}(0)}{2}\Delta\eta + f'(\Delta\eta)\tau^{**}(\Delta\eta)\Delta\eta + f'(2\Delta\eta)\tau^{**}(2\Delta\eta)\Delta\eta + \cdots\\ + f'(\eta_\infty-\Delta\eta)\tau^{**}(\eta_\infty-\Delta\eta)\Delta\eta + \frac{f'(\eta_\infty)\tau^{**}(\eta_\infty)}{2}\Delta\eta.\end{aligned} \tag{B.9}$$

Discretization of the time derivative

The time derivative is discretized using a first order differential quotient

$$\frac{\partial P^{**}(k,l,\eta,t)}{\partial t} = \frac{P^{**}(k,l,\eta,t+\Delta t)-P^{**}(k,l,\eta,t)}{\Delta t}. \tag{B.10}$$

Formulating an explicit scheme for the unsteady interaction law yields

$$\begin{aligned}&P^{**}(k,l,t+\Delta t) = P^{**}(k,l,t) + \Delta t[sign(K)ikP^{**}(l,k,t)+\\ &+\Lambda ik\left(\int_0^\infty \hat{\tau}(k,l,\eta',t)^{**}d\eta' - S^{**} - \frac{1}{\Lambda\,|K|}\frac{l^2}{k^2}P^{**}(k,l,t)\right) + \frac{1}{2}\mathcal{F}^2\left\{P^2(X,Z,t)\right\}].\end{aligned} \tag{B.11}$$

B.3. Numerical Scheme

Discretization of the equations (B.3) to (B.6) finally yields the nonlinear problem

$$\boldsymbol{G} \cdot \vec{x}(k, l, \eta) = \vec{g}, \tag{B.12}$$

where $\boldsymbol{G}$ is the system matrix of the problem, $\vec{x}$ the solution vector in spectral space and $\vec{g}$ contains the nonlinear terms of (B.3) and (B.4). To avoid the calculation of convolution terms in spectral space due to the nonlinear terms in $\vec{g}$ the problem is solved iteratively. The nonlinear terms are evaluated in physical space and mapped back into spectral space giving a new right hand side in (B.12). Thus, in a first step the linearized problem is solved, which yields a first approximation of the flow field. In a second step equation (B.12) is solved again, but now considering the nonlinear terms evaluated with the flow quantities of the previous step. This procedure, see figure B.1, is repeated until a given residuum is reached.

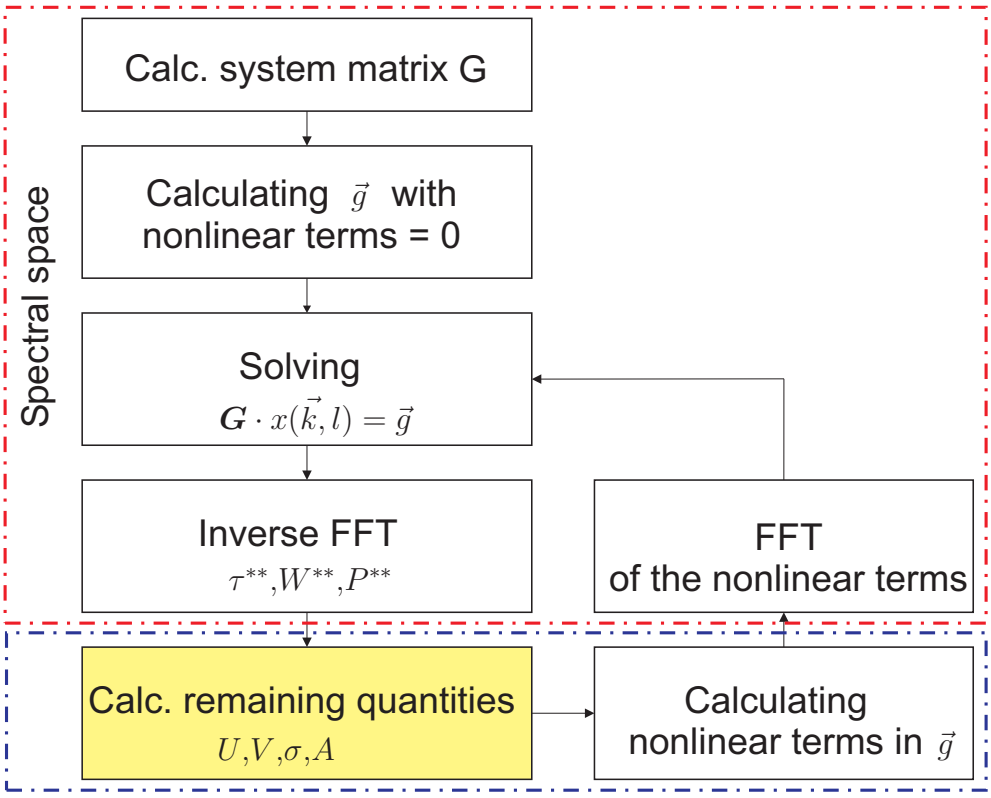

Figure B.1.: Calculation scheme of the pseudo spectral method

If the hump height is fixed the calculation procedure is straight forward by solving the problem as sketched in figure B.1. The surface deformation enters the systems matrix $\boldsymbol{G}$ and remains constant. In case of studying bifurcating solutions for increasing values of the hump height, as performed in chapter 6, instead of prescribing the hump height and solving the resulting flow field one flow quantity is prescribed in a single point of the calculation domain, e.g. the wall shear stress $\tau_w(X_p, Z_p)$. The height of the hump becomes part of the solution and an additional equation, e.g. the prescribed wall shear stress in the flow field

$$\tau_w(X_p, Z_p) = \frac{1}{k_{max} \cdot l_{max}} \sum_{k=0}^{k_{max}-1} \sum_{l=0}^{l_{max}-1} exp\left(2\pi i \left[\frac{X_p \cdot k}{k_{max}} + \frac{Z_p \cdot l}{l_{max}}\right]\right)$$

has to be considered, where X_P and Z_P are the coordinates of the prescribed quantity, k_{max} and l_{max} the number of spectral modes.

B.4. Grids and Collocation Points

To use standard numerical algorithms, e.g. Fast Fourier Transform Algorithms, [12], for the Fourier Transform as well as for the inverse Fourier Transform uniformly distributed collocation points in the physical domain are necessary. Thus the size of the calculation domain is restricted by the maximum numbers of collocation points due to memory. But since the problem can be solved for each spectral mode independently the size of the system matrix is $\mathcal{O}(N_{max})$ and the number of collocation points and spectral modes can be rather large.
For very slowly decaying solutions the calculation domain has to be increased and hence an appropriate mapping has to be introduced. The idea is to map the unbounded physical domain onto a bounded domain with uniformly distributed collocation points.

The required mapping function should satisfy the following conditions:

- mapping from an infinite domain $[-\infty, \infty]$ onto a finite domain
- clustering of the collocation points near the origin on the unbounded domain
- minimal number of spectral modes of the introduced new metric for a minimal truncation error

An appropriate mapping function satisfying all of these requirement is the cotangent function, cf. [5], [9]

$$X = h(\chi) = -d \cdot cotan(\chi),$$

which maps the physical domain $X \in [-\infty, \infty)$ onto the calculation domain $\chi \in [0, \pi)$. Due to this mapping a new metric is introduced with the metric function

$$\frac{d}{dX} f(X) = \frac{1}{h'} \frac{d}{d\chi} f(\chi) \quad \text{with} \quad \frac{1}{h'} = \frac{1}{d} sin^2(\chi) = \frac{1}{2d} \left[1 - \frac{e^{2\pi i \chi} + e^{-2\pi i \chi}}{2} \right].$$

This results in a modal coupling and therefore the problem has to be solved for all modes simultaneously. Thus the size of the system matrix is of $\mathcal{O}(k_{max} \cdot l_{max} \cdot N_{max})$ and the number of spectral modes and collocations points has to be much smaller than in the unmapped case. But due to the clustering near the origin and the associated higher resolution of the solutions in this region even calculations with just about 100 modes in each direction yields reasonable results.

	Scheme with infinite domain	Scheme with finite domain
k_{max}	128	1024
l_{max}	128	1024
N_{max}	50	50
X_{max}/Z_{max}	-	$\pm 100 / \pm 100$
η_∞	0.98	0.98
d	4/2	-

Table B.1.: Parameters of the numerical scheme

List of Figures

1.1. MEMS turbine stage with 4mm diameter, A. H. Epstein, MIT Cambridge, [17] (left hand side) and supersonic micro nozzle, S.W. Janson, H. Helvajian and K. Breuer, The Aerospace Corporation, [24] (right hand side). . 1

2.1. Slender Laval nozzle with interaction region. 4
2.2. Tripledeck structure of the viscous inviscid interaction region. 7
2.3. Tripledeck structure and length scales of the interaction region. 12

3.1. Flow structure under subsonic flow conditions ($\Lambda = 1.25, K = 1$). 29
3.2. Crossflow velocity profiles W in region I-IV,($\Lambda = 1.25, K = 1, h_{hump} = 0.1$). 29
3.3. Wall shear stress τ_w and pressure perturbation P along the centerline of the hump (Z=0) for $\Lambda = 1.25$, $K = 1$ and and $h_{hump} = 0.1$. 30
3.4. Flow structure under supersonic flow conditions ($\Lambda = 1.25, K = -1$). . . 32
3.5. Crossflow velocity profiles W in region I-IV,($\Lambda = 1.25, K = -1, h_{hump} = 0.1$). 33
3.6. Wall shear stress τ_w and pressure perturbation P along the centerline of the hump (Z=0) for $\Lambda = 1.25$, $K = -1$ and $h_{hump} = 0.1$. 33

4.1. Wall shear stress τ_w and pressure perturbation P along the centerline of the hump (Z=0) for $\Lambda = 1.25$, $K = 1$ and $h_{hump} = 2.25$. 38
4.2. Wall streamlines in the vicinity of the hump (left hand side) and streamlines in a cross section $Z = 0$ with a separation bubble at the lee side of the hump (right hand side), ($h_{hump} = 2.25, \Lambda = 1.25, K = 1$). 39
4.3. Streamwise velocity profiles $U(X, Y, 0)$ in the separation bubble at the centerline $Z = 0$. 39

4.4. Wall streamlines with an appropriate scaled crossflow velocity component in the vicinity of the hump and the point of weak convergence at $X = 0.57, Z = 0$ (left hand side) and the flow structure close to the point of weak convergence with the angle of the separation streamline ϑ_{SEP} (right hand side). 40
4.5. Streamlines in a cross section through the centerline Z=0 in the vicinity of the separation point (dashed lines) with the separation streamline (solid line) and separation angle ϑ_{SEP}. 42
4.6. Pressure perturbation P for various values of K under subsonic flow conditions (left hand side) and under supersonic flow conditions (right hand side), $(h_{hump} = 1.0, \Lambda = 1.25|K|^{-3/2})$. 43

5.1. Zeros (circles) of the denominator function $f(s, l)$ under supersonic flow conditions (red lines) and subsonic flow conditions (blue lines). 49
5.2. Poles, pole traces and zeros of the transfer function Ω under supersonic (left hand side) and subsonic (right hand side) flow conditions. 51
5.3. Algebraic-exponential decay of the upstream pressure perturbation under supersonic flow conditions. 54
5.4. Algebraic decay of the upstream pressure perturbation under subsonic flow conditions. 54
5.5. Asymptotic structure of the upstream perturbation of the pressure under supersonic flow conditions (solid line) and numerical results for $K = -1$, $\Lambda = 1.25$ ($\bigcirc ...X = -11.5$, $\square ...X = -16$ and $\diamond ...X = -20$). 58
5.6. Asymptotic structure of the upstream perturbation of the pressure under subsonic flow conditions (solid line) and numerical results for $K = 1$, $\Lambda = 1.25$ ($\square ...X = -16$, $\diamond ...X = -20$ and $\bigtriangledown ...X = -35$). 58
5.7. Constant hump geometry with respect to Z ($\alpha = 0$) (left hand side) and deformed hump geometry ($\alpha = 0.5$) (right hand side). 62
5.8. Pressure perturbation along the centerline $Z = 0$ for various deforming parameters α, $h_{hump} = 1.25, \Lambda = 1.25, K = -1$. 62
5.9. Periodic ridge with respect to Z (left hand side) and corresponding pressure perturbation P (right hand side) for $\Lambda = 1.25$, $K = 1$ and $h_{hump} = 2.25$. 64
5.10. Pressure perturbation for various hump height at $X = 0.85$, $Z = 0$ under subsonic flow conditions for $\Lambda = 1.25$ and $K = 1$. 66

6.1. Bifurcation curve of the pressure perturbation $P(X = 0.85, Z = 0)$ near the bifurcation point $h_c = 2.588$, $\Lambda = 1.25$, $K = 1$. 68
6.2. Pressure perturbation (red) and wall shear stress (blue) associated with the upper branch (solid line) and the corresponding lower branch solution (dashed) for $h_{hump} = 2.4$ (left hand side) and $h_{hump} = 2.3$ (right hand side). 68
6.3. Pressure perturbation with parabola approximation near the bifurcation point. 70
6.4. Phase curve of the bifurcation equation with stable and unstable stationary points corresponding to the upper and lower branch solution in the subcritical case ($sign(\Delta h) > 0$). 72
6.5. Right eigenfunction $m_3(X, Z)$ (left hand side) and approximation of the pressure perturbation ($P \sim P_c + \sqrt{\Delta h} \cdot c_s m_3 + \Delta h \cdot P_2$) close to the turning point (h_c, P_c) (right hand side). 73
6.6. Bifurcation curve of the pressure perturbation for various values of the hump width ($\Lambda = 1.25$, $K = 1$). 74
6.7. Degeneration of the turning point bifurcation for increasing values of the hump width b_i. 75

B.1. Calculation scheme of the pseudo spectral method 89

List of Tables

6.1. 1^{st} and 2^{nd} order approx. terms for various values of the hump width b . 75

B.1. Parameters of the numerical scheme 91

Bibliography

[1] M. Abramowitz and I.A. Stegun. *Handbook of mathematical functions.* U.S. Dept. of Commerce, National Institute of Standards and Technology, 1972.

[2] R.L. Bayt and K.S. Breuer. Viscous effects in supersonic MEMS-fabricated micronozzles. In *Proc. 3rd ASMEMicrofluids Symposium*, 1998.

[3] S. Biringen and K.H. Kao. On the application of pseudospectral FFT techniques to non-periodic problems. *Int. J. Numer. Meth. Fluids*, 9:1235–1267, 1989.

[4] R.J. Bodonyi and A. Kluwick. Freely interacting transonic boundary layers. *Phys. Fluids*, 20:1432–1437, 1977.

[5] J.P. Boyd. Spectral Methods Using Rational Basis Functions on an Infinite Interval. *J. Comput. Phys.*, 69:112–142, 1987.

[6] S. Braun and A. Kluwick. The effect of three-dimensional obstacles on marginally separated laminar boundary-layer flows. *J. Fluid Mech.*, 460:57–82, 2002.

[7] S. Braun and A. Kluwick. Analysis of a bifurcation problem in marginally separated laminar wall jets and boundary layers. *Acta Mechanica*, 161:195–211, 2003.

[8] S. Braun and A. Kluwick. Blow-up and control of marginally separated boundary layer flows. In *New Developments and Applications in Rapid Fluid Flows (Eds. J.S.B. Gajjar and F.T. Smith)*, volume 363 of *Phil. Trans. R. Soc. Lond. A*, pages 1057–1067, 2005.

[9] A.B. Cain, J.H. Ferziger, and W.C. Reynolds. Discrete Orthogonal Functions Expansion for Non-uniform Grids Using the Fast Fourier Transform. *J. Comput. Phys.*, 56:272–286, 1984.

[10] C. Canuto, M.Y. Hussaini, A. Quarteroni, and Th.A. Zang. *Spectral-Methods in Fluid Dynamics.* Springer Verlag, 1987.

[11] D.R. Chapman, D.M. Kuehn, and H.K. Larson. Investigation of separated flows in supersonic and subsonic streams with emphasis on the effect of transition. *Nat. Adv. Comm. Aeronaut. Rep.*, 1356, 1958.

[12] J.W. Cooley and J. Tukey. An algorithm for the machine calculation of complex Fourier series. *Math. Comput.*, 19:297–301, 1965.

[13] M. Cramer and A. Kluwick. On the propagation of waves exhibiting both positive and negative nonlinearity. *J. Fluid Mech.*, 142:9–37, 1984.

[14] M.S. Cramer and A.B. Crickenberger. The dissipative structure of shock waves in dense gases. *J. Fluid Mech.*, 223:325–355, 1991.

[15] P.W. Duck and O.R. Burggraf. Spectral solutions for three-dimensional triple-deck flow over surface topography. *J. Fluid Mech.*, 162:1–22, 1985.

[16] J.W. Elliot, A.P. Rothmayer, and F.T. Smith. The structure of three-dimensional free-interactions in external, steady, compressible flows. *Eur. J. Mech.,B/Fluids*, 10:227–251, 1991.

[17] A.H. Epstein. Milimeter-scale, MEMS gas turbine engines. In *Proceedings of ASME Turbo Expo 2003,Power for Land, Sea and Air*, volume GT-2003-38866 of *ASME*, pages 1–28, 2003.

[18] M.J. Lighthill et al. *Laminar Boundary Layers*, chapter Introduction. Boundary layer theory. Oxford University Press, 1963.

[19] D. Gottlieb and S.A. Orszag. *Numerical Analysis of Spectral Methods: Theory and Application*. Society for Industrial and Applied Mathematics, 1993.

[20] A. Gyr and K. Hoyer. *Sediment Transport*. Springer Verlag, 2006.

[21] Peng-Fei Hao et al. Size effect on gas flow in micro nozzles. *J. Micromech. Microeng.*, 15:2069–2073, 2005.

[22] C. Huang, J.W. Gregory, and J.P. Sullivan. Flow Visualization and Pressure Measurement in Micronozzles. *Journal of Visualization*, 10:281–288, 2007.

[23] I.H.J. Jahn et al. Experimental characterisation of the stiffness and leakage of a prototype leaf seal for turbine applications. In *Proceedings of ASME Turbo Expo 2008,Power for Land, Sea and Air*, volume GT2008-51206 of *ASME*, page 10, 2008.

[24] S.W. Janson, H. Helvajian, and K. Breuer. MEMS, microengineering and Aerospace Systems. *AIAA*, 99-3802, 1999.

[25] A. Kluwick. Transonic nozzle flow of dense gases. *J. Fluid Mech.*, 247:661–699, 1993.

[26] A. Kluwick. *Recent advances in boundary layer theory*, chapter Interacting laminar and turbulent boundary layers. Number 350 in CISM Courses and Lectures. Springer Wien NewYork, 1998.

[27] A. Kluwick. *Recent advances in boundary layer theory*. Springer Verlag, 1998.

[28] A. Kluwick, S. Braun, and Ph. Gittler. Transonic, laminar high Reynolds number flow in slender channels. In *Proceedings of the IUTAM symposium held in Göttingen, Germany*, IUTAM Symposium Transonicum IV, 2002.

[29] A. Kluwick and Ph. Gittler. Transonic laminar interacting boundary layers in narrow channels. *ZAMM*, 81:473–474, 2001.

[30] A. Kluwick and G. Meyer. Shock regularization in dense gases by viscous-inviscid interactions. *J. Fluid Mech.*, 644:473–507, 2010.

[31] A. Kluwick and G. Meyer. Shock regularization in dense gases by viscous-inviscid interactions. *J. Fluid Mech.*, 644:473–507, 2010.

[32] A. Kluwick, M. Reiterer, and G. Hackmüller. Marginal separation caused by three-dimensional surface mounted obstacles. In *Proc. 2nd Int. Conf. on Asymptotics in Mechanics,St. Petersburg State Marine Technical University*, pages 113–120, 1997.

[33] M.J. Lighthill. On boundary layers and upstream influence ii. supersonic flows without separation. *Proc. Roy. Soc.*, A217:478–507, 1953.

[34] W.F. Louisos and D.L. Hitt. Viscous Effects on Performance of Two-Dimensional Supersonic Linear Micronozzles. *J. of Spacecraft and Rockets*, 45:706, 2008.

[35] A.F. Messiter. Boundary layer flow near the trailing edge of a flat plate. *SIAM J.Appl. Math.*, 18:241–257, 1970.

[36] G. Meyer. *Transonic Viscous Inviscid Interactions in Narrow Channels*. PhD thesis, TU Wien, 2010.

[37] H. Nakane et al. The Development of High-Performance Leaf Seals. In *Tranactions of the ASME*, volume 126 of *ASME*, pages 342–350, 2004.

[38] V.Ya. Neiland. Towards a theory of separation of the laminar boundary layer in a supersonic stream. *Ivz. Akad. Nauk. SSSR, Mekh. Zhidk. Gaza*, 4:53–57, 1976.

[39] K. Oswatitsch. *Contributions to the Development of Gasdynamics*. Vieweg Verlag, 1980.

[40] E.S. Piekos and K.S. Breuer. Numerical modeling of micromechanical devices using direct simulation monte carlo method. *J. Fluid Eng., Trans. ASME*, 118:464–469, 1996.

[41] L. Prandtl. Zur Berechnung der Grenzschichten. *Z. angew. Math. Mech.*, 18:77–82, 1938.

[42] D.E. Rothe. Electron-beam studies of viscous flow in supersonic nozzles. *AIAA*, 9:804–811, 1972.

[43] H. Schlichting and K. Gersten. *Grenzschicht-Theorie*. Springer Verlag, 1997.

[44] W. Schneider. Upstream propagation of unsteady disturbances in supersonic boundary layers. *J. Fluid Mech.*, 63(3):205–234, 1974.

[45] R. Sedney. A Survey of the Effects of Small Protuberances on Boundary-Layer Flows. *AIAA J.*, 11:782–792, 1973.

[46] A.H. Shapiro. *The Dynamics and Thermodynamics of Compressible Fluid Flow*. The Ronald Press Company, 1953.

[47] F.T. Smith. On entry-flow effects in bifurcating, blocked or constricted tubes. *J. Fluid Mech.*, 78:709, 1976.

[48] F.T. Smith. Pipeflows distorted by nonsymmetric indentation or branching. *Mathematika*, 23:62, 1976.

[49] F.T. Smith, R.I. Sykes, and P.W.M. Brighton. A two-dimensional boundary layer encountering a three-dimensional hump. *J. Fluid Mech.*, 83:163–176, 1977.

[50] K. Stewartson. Multistrucured boundary layers on flat plates and related bodies. *Adv. Appl. Mech.*, 14:145–239, 1974.

[51] K. Stewartson and P.G. Williams. Self-induced separation. *Proc. Roy. Soc.*, A312:181–206, 1969.

[52] K. Stewartson and P.G. Williams. On self-induced separation ii. *Mathematika*, 20:98–108, 1973.

[53] H. Troger and A. Steindl. *Nonlinear Stability and Bifurcation Theory*. Springer Verlag, 1991.

[54] M. VanDyke. *Perturbation Methods in Fluid Mechanics*. Parabolic Press, 1975.

[55] D. Weihs and J. Katz. Cellular patterns in post stall flow over unswept wings. *AIAA J.*, 21:1757–1759, 1983.

[56] A.E. Winkelmann. The effects of aspect ratio on the stall of a finite wing. *AIAA paper*, 89-0570, 1989.

[57] J. Xu and C. Zhao. Two-dimensional numerical simulations of shock waves in micro convergent-divergent nozzles. *Int. J. of Heat and Mass Transfer*, 50:2434–2438, 2007.

Curriculum vitae

Dipl.-Ing. Matthias Kornfeld
Parkstraße 4/21, A-2340 Mödling
Date of Birth: November 24^{th}, 1982
Place of Birth: Vienna
Nationality: Austria

Educational Background

Jan. 2008 - currently	**University of Technology Vienna** Ph.D studies: Institute of Fluid Mechanics and Heat Transfer, Advisor: Prof. A. Kluwick
Oct. 2003 - Nov. 2007	**University of Technology Vienna** Mechanical engineering (Diploma program), Diploma thesis: *Laval nozzle used as suction device*, Advisor: Prof. H. Steinrück
Oct. 2002 - May 2003	**Military Service** Truck driver at PzB33
Sept. 1997 - Nov. 2002	**Upper secondary school of technology, HTBL Wien 10** 5-year course: Environmental engineering
Sept. 1993 - June. 1997	**Grammar school Perchtoldsdorf**
Sept. 1989 - June. 1993	**Elementary school Perchtoldsdorf**

Employments and Internships

Jan. 2009 - Dec. 2010	Research assistant (FWF) at the Institute of Fluid Mechanics and Heat Transfer, Student member of the doctoral college WK Differential Equations.
February - June 2007	Tutor at the Institute of Mechanics and Mechatronics TU Vienna, Division Measurements and Actuators.
July 2001	Student trainee at Turbotherm, Luft- und Wärmetechnik.
July 1998	Student trainee at Jenbacher Werke AG, Division construction and research.
July - August 1997	Student trainee at Turbotherm, Luft- und Wärmetechnik.

List of Publications

M. Kornfeld and A. Kluwick. Weakly 3D Transonic Flows in Narrow Channels. talk at GAMM Annual Meeting 2010, Karlsruhe, Germany; 02-09-2009 - 02-13-2009. in Proceedings in Applied Mathematics and Mechanics PAMM 2010, Wiley InterScience, Volume 10, Issue 1 (2010). 469 - 470.

M. Kornfeld and A. Kluwick. Weakly 3D effects upstream a surface mounted obstacle in transonic flows. in CISM Courses and Lectures - Asymptotic Methods in Fluid Mechanics: Survey and Recent Advances, H. Steinrück (ed.); issued by: CISM. Springer-Verlag, Wien/New York, 2010.

M. Kornfeld and A. Kluwick. Local Interaction Theory for Laminar Transonic Flows in Slender Channels. talk at GAMM Annual Meeting 2009, Gdansk, Poland; 02-09-2009 - 02-13-2009. in Proceedings in Applied Mathematics and Mechanics PAMM 2009, Wiley InterScience, Volume 9, Issue 1 (2009), ISSN: 1617-7061. 467 - 468.

H. Steinrück, M. Kornfeld and S. Braun. Flare Gas Extraction by a Laval Nozzle. talk at GAMM 2008, Bremen. 03-31-2008 - 04-04-2008. in GAMM Annual Meeting, Bremen 2008, PAMM, Wiley InterScience, 8 (2008), ISSN: 1617-7061. 2 pages.